

# Electronic Properties of Graphene in a Strong Magnetic Field

M. O. Goerbig

<sup>1</sup>*Laboratoire de Physique des Solides, Univ. Paris-Sud, CNRS UMR 8502, F-91405 Orsay, France*

(Dated: November 26, 2024)

We review the basic aspects of electrons in graphene (two-dimensional graphite) exposed to a strong perpendicular magnetic field. One of its most salient features is the relativistic quantum Hall effect the observation of which has been the experimental breakthrough in identifying pseudo-relativistic massless charge carriers as the low-energy excitations in graphene. The effect may be understood in terms of Landau quantisation for massless Dirac fermions, which is also the theoretical basis for the understanding of more involved phenomena due to electronic interactions. We present the role of electron-electron interactions both in the weak-coupling limit, where the electron-hole excitations are determined by collective modes, and in the strong-coupling regime of partially filled relativistic Landau levels. In the latter limit, exotic ferromagnetic phases and incompressible quantum liquids are expected to be at the origin of recently observed (fractional) quantum Hall states. Furthermore, we discuss briefly the electron-phonon coupling in a strong magnetic field. Although the present review has a dominating theoretical character, a close connection with available experimental observation is intended.

PACS numbers: 81.05.ue, 73.43.Lp, 73.22.Pr

## Contents

<b>I. Introduction to Graphene</b>	1	<b>IV. Magneto-Phonon Resonance in Graphene</b>	31
A. The Carbon Atom and its Hybridizations	2	A. Electron-Phonon Coupling	31
B. Crystal Structure of Graphene	3	1. Coupling Hamiltonian	32
C. Electronic Band Structure of Graphene	4	2. Hamiltonian in terms of magneto-exciton operators	32
1. Tight-binding model for electrons on the honeycomb lattice	4	B. Phonon Renormalization and Raman Spectroscopy	33
2. Continuum limit	7	1. Non-resonant coupling and Kohn anomaly	33
D. Deformed Graphene	10	2. Resonant coupling	34
1. Dirac point motion	11	<b>V. Electronic Correlations in Partially Filled Landau Levels</b>	35
2. Tilted Dirac cones	12	A. Electrons in a Single Relativistic Landau Level	35
<b>II. Dirac Equation in a Magnetic Field and the Relativistic Quantum Hall Effect</b>	13	1. SU(4)-symmetric model	36
A. Massless 2D Fermions in a Strong Magnetic Field	13	2. Symmetry-breaking long-range terms	37
1. Quantum-mechanical treatment	14	3. Qualitative expectations for correlated electron phases	37
2. Relativistic Landau levels	14	4. External spin-valley symmetry breaking terms	39
B. Limits of the Dirac Equation in the Description of Graphene Landau Levels	17	5. Hierarchy of relevant energy scales	40
C. Landau Level Spectrum in the Presence of an Inplane Electric Field	19	B. SU(4) Quantum Hall Ferromagnetism in Graphene	41
D. Landau Levels in Deformed Graphene	19	1. Ferromagnetic ground state and Goldstone modes	41
1. The generalized Weyl Hamiltonian in a magnetic field	19	2. Skyrmions and entanglement	42
2. Tilted Dirac cones in a crossed magnetic and electric field	20	3. Comparison with magnetic catalysis	45
<b>III. Electronic Interactions in Graphene – Integer Quantum Hall Regime</b>	20	4. The quantum Hall effect at $\nu = \pm 1$ and $\nu = 0$	46
A. Decomposition of the Coulomb interaction in the Two-Spinor Basis	22	C. Fractional Quantum Hall Effect in Graphene	48
1. SU(2) valley symmetry	23	1. Generalized Halperin wave functions	48
2. SU(4) spin-valley symmetric Hamiltonian	24	2. The use of generalized Halperin wave functions in graphene	49
B. Particle-Hole Excitation Spectrum	24	3. Experiments on the graphene FQHE	51
1. Graphene particle-hole excitation spectrum at $B = 0$	25	<b>VI. Conclusions and Outlook</b>	51
2. Polarizability for $B \neq 0$	26	<b>Acknowledgments</b>	52
3. Electron-electron interactions in the random-phase approximation: upper-hybrid mode and linear magnetoplasmons	28	<b>A. Matrix Elements of the Density Operators</b>	52
4. Dielectric function and static screening	29	<b>References</b>	53
		<b>I. INTRODUCTION TO GRAPHENE</b>	

The experimental and theoretical study of graphene, two-dimensional (2D) graphite, has become a major issue of modern condensed matter research. A milestone

was the experimental evidence of an unusual quantum Hall effect reported in September 2005 by two different groups, the Manchester group led by Andre Geim and a Columbia-Princeton collaboration led by Philip Kim and Horst Stormer (Novoselov *et al.*, 2005a; Zhang *et al.*, 2005).

The reasons for this enormous scientific interest are manifold, but one may highlight some major motivations. First, one may underline its possible technological potential. One of the first publications on graphene in 2004 by the Geim group reported indeed an electric field effect in graphene, i.e. the possibility to control the carrier density in the graphene sheet by simple application of a gate voltage (Novoselov *et al.*, 2004). This effect is a fundamental element for the design of electronic devices. In a contemporary publication Berger *et al.* reported on the fabrication and the electrical contacting of monolayer graphene samples on epitaxially grown SiC crystals (Berger *et al.*, 2004). Today's silicon-based electronics reaches its limits in miniaturization, which is on the order of 50 nm for an electric channel, whereas it has been shown that a narrow graphene strip with a width of only a few nanometers may be used as a transistor (Ponomarenko *et al.*, 2008), i.e. as the basic electronics component.

Apart from these promising technological applications, two major motivations for fundamental research may be emphasized. Graphene is the first truly 2D crystal ever observed in nature and possess remarkable mechanical properties. Furthermore, electrons in graphene show relativistic behavior, and the system is therefore an ideal candidate for the test of quantum-field theoretical models that have been developed in high-energy physics. Most prominently, electrons in graphene may be viewed as massless charged fermions living in 2D space, particles one usually does not encounter in our three-dimensional world. Indeed, all massless elementary particles happen to be electrically neutral, such as photons or neutrinos.<sup>1</sup> Graphene is therefore an exciting bridge between condensed-matter and high-energy physics, and the research on its electronic properties unites scientists with various thematic backgrounds.

Several excellent reviews witness the enormous research achievements in graphene. In a first step those by Geim and Novoselov (Geim and Novoselov, 2007) and by de Heer (de Heer *et al.*, 2007) aimed at a rather global experimental review of exfoliated and epitaxial graphene, respectively. Furthermore, the review by Castro Neto (Castro Neto *et al.*, 2009) was concerned with general theoretical issues of electrons in graphene. Apart from the review by Abergel *et al.* (Abergel *et al.*, 2010), more recent reviews concentrate on the subfields of graphene

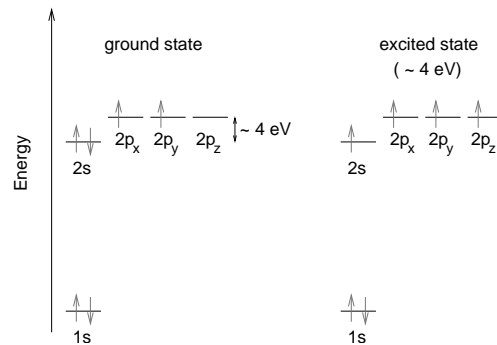


Figure 1 Electronic configurations for carbon in the ground state (left) and in the excited state (right).

research, which have themselves grown to a considerable size and that require reviews on their own. As an example one may cite the review by Peres (Peres, 2010), which is concerned with transport properties of graphene, or that by Kotov and co-workers on interaction effects (Kotov *et al.*, 2010). The present theoretical review deals with electronic properties of graphene in a strong magnetic field, and its scope is delimited to monolayer graphene. The vast amount of knowledge on bilayer graphene certainly merits a review on its own.

## A. The Carbon Atom and its Hybridizations

In order to understand the crystallographic structure of graphene and carbon-based materials in general, it is useful to review the basic chemical bonding properties of carbon atoms. The carbon atom possesses 6 electrons, which, in the atomic ground state, are in the configuration  $1s^2 2s^2 2p^2$ , i.e. 2 electrons fill the inner shell 1s, which is close to the nucleus and which is irrelevant for chemical reactions, whereas 4 electrons occupy the outer shell of 2s and 2p orbitals. Because the 2p orbitals ( $2p_x$ ,  $2p_y$ , and  $2p_z$ ) are roughly 4 eV higher in energy than the 2s orbital, it is energetically favorable to put 2 electrons in the 2s orbital and only 2 of them in the 2p orbitals (Fig 1). It turns out, however, that in the presence of other atoms, such as e.g. H, O, or other C atoms, it is favorable to excite one electron from the 2s to the third 2p orbital, in order to form covalent bonds with the other atoms.

In the excited state, we therefore have four equivalent quantum-mechanical states,  $|2s\rangle$ ,  $|2p_x\rangle$ ,  $|2p_y\rangle$ , and  $|2p_z\rangle$ . A quantum-mechanical superposition of the state  $|2s\rangle$  with  $n$   $|2p_j\rangle$  states is called  $sp^n$  hybridization. The  $sp^1$  hybridization plays, e.g., an important role in the context of organic chemistry (such as the formation of acetylene) and the  $sp^3$  hybridization gives rise to the formation of diamonds, a particular 3D form of carbon. Here, however, we are interested in the planar  $sp^2$  hybridization, which is the basic ingredient for the graphitic allotropes.

As shown in Fig. 2, the three  $sp^2$ -hybridized orbitals are oriented in the  $xy$ -plane and have mutual  $120^\circ$  angles.

<sup>1</sup> The neutrino example is only partially correct. The observed oscillation between different neutrino flavors ( $\nu_\mu \leftrightarrow \nu_\tau$ ) requires indeed a tiny non-zero mass (Fukuda, Y. *et al.* (Super-Kamiokande Collaboration), 1998).

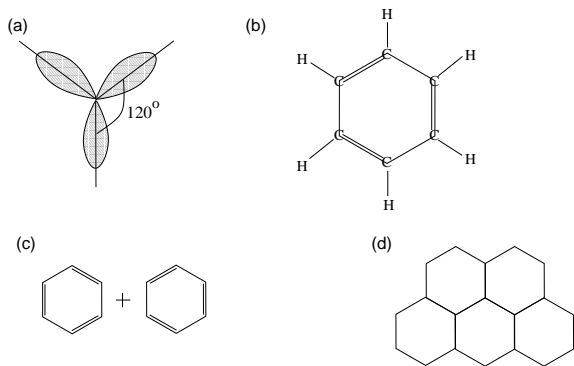


Figure 2 (a) Schematic view of the  $sp^2$  hybridization. The orbitals form angles of  $120^\circ$ . (b) Benzene molecule ( $C_6H_6$ ). The 6 carbon atoms are situated at the corners of a hexagon and form covalent bonds with the H atoms. (c) The quantum-mechanical ground state of the benzene ring is a superposition of the two configurations which differ by the position of the  $\pi$  bonds. (d) Graphene may be viewed as a tiling of benzene hexagons, where the H atoms are replaced by C atoms of neighboring hexagons and where the  $\pi$  electrons are delocalized over the whole structure.

The remaining unhybridized  $2p_z$  orbital is perpendicular to the plane.

A prominent chemical example for such hybridization is the benzene molecule the chemical structure of which has been analyzed by August Kekulé in 1865 (Kekulé, 1865, 1866). The molecule consists of a hexagon with carbon atoms at the corners linked by  $\sigma$  bonds [Fig. 2 (b)]. Each carbon atom has, furthermore, a covalent bond with one of the hydrogen atoms which stick out from the hexagon in a star-like manner. In addition to the six  $\sigma$  bonds, the remaining  $2p_z$  orbitals form three  $\pi$  bonds, and the resulting double bonds alternate with single  $\sigma$  bonds around the hexagon. Because a double bond is stronger than a single  $\sigma$  bond, one may expect that the hexagon is not perfect. A double bond (C=C) yields indeed a carbon-carbon distance of 0.135 nm, whereas it is 0.147 nm for a single  $\sigma$  bond (C-C). However, the measured carbon-carbon distance in benzene is 0.142 nm for all bonds, which is roughly the average length of a single and a double bond. This equivalence of all bonds in benzene was explained by Linus Pauling in 1931 within a quantum-mechanical treatment of the benzene ring (Pauling, 1960). The ground state is indeed a quantum-mechanical superposition of the two possible configurations for the double bonds, as shown schematically in Fig. 2 (c).

These chemical considerations indicate the way towards carbon-based condensed matter physics – any graphitic compound has indeed a sheet of graphene as its basic constituent. Such a graphene sheet may be viewed simply as a tiling of benzene hexagons, where the hydrogen are replaced by carbon atoms to form a neighboring carbon hexagon [Fig. 2 (d)]. However, graphene has remained the basic constituent of graphitic systems during a long time only on the theoretical level. From an experimental point of view, graphene is the youngest allotrope

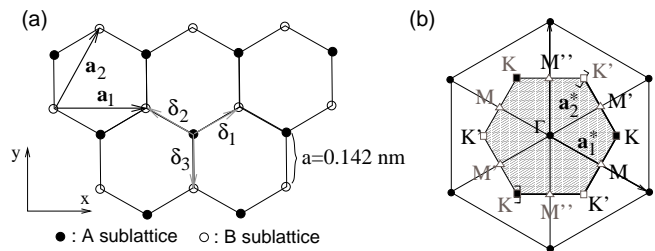


Figure 3 (a) Honeycomb lattice. The vectors  $\delta_1$ ,  $\delta_2$ , and  $\delta_3$  connect  $nn$  carbon atoms, separated by a distance  $a = 0.142$  nm. The vectors  $\mathbf{a}_1$  and  $\mathbf{a}_2$  are basis vectors of the triangular Bravais lattice. (b) Reciprocal lattice of the triangular lattice. Its primitive lattice vectors are  $\mathbf{a}_1^*$  and  $\mathbf{a}_2^*$ . The shaded region represents the first Brillouin zone (BZ), with its center  $\Gamma$  and the two inequivalent corners  $K$  (black squares) and  $K'$  (white squares). The thick part of the border of the first BZ represents those points which are counted in its definition such that no points are doubly counted. The first BZ, defined in a strict manner, is, thus, the shaded region plus the thick part of the border. For completeness, we have also shown the three inequivalent crystallographic points  $M$ ,  $M'$ , and  $M''$  (white triangles).

and accessible to electronic-transport measurements only since 2004.

For a detailed discussion of the different fabrication techniques, the most popular of which are the exfoliation technique (Novoselov *et al.*, 2005b) and thermal graphitization of epitaxially-grown SiC crystals (Berger *et al.*, 2004), we refer the reader to existing experimental reviews (Geim and Novoselov, 2007; de Heer *et al.*, 2007). Notice that, more recently, large-scale graphene has been fabricated by chemical vapor deposition (Reina *et al.*, 2009) that seems a promising technique not only for fundamental research but also for technological applications.

## B. Crystal Structure of Graphene

As already mentioned in the last section, the carbon atoms in graphene condense in a honeycomb lattice due to their  $sp^2$  hybridization. The honeycomb lattice is not a Bravais lattice because two neighboring sites are inequivalent from a crystallographic point of view.<sup>2</sup> Fig. 3 (a) illustrates indeed that a site on the A sublattice has nearest neighbors ( $nn$ ) in the directions north-east, north-west, and south, whereas a site on the B sublattice has  $nns$  in the directions north, south-west, and south-east. Both A and B sublattices, however, are triangular Bravais lattices, and one may view the honeycomb lattice as a *triangular Bravais lattice with a two-atom basis* (A and B). The distance between  $nn$  carbon atoms is  $a = 0.142$  nm, which is the average of the single (C-C) and double (C=C) covalent  $\sigma$  bonds, as in the case of

<sup>2</sup> This needs to be clearly distinguished from a chemical point of view according to which they may be equivalent as in the case of graphene where both types of sites consist of carbon atoms.

benzene.

The three vectors which connect a site on the A sublattice with a  $mn$  on the B sublattice are given by

$$\boldsymbol{\delta}_1 = \frac{a}{2} (\sqrt{3}\mathbf{e}_x + \mathbf{e}_y), \quad \boldsymbol{\delta}_2 = \frac{a}{2} (-\sqrt{3}\mathbf{e}_x + \mathbf{e}_y), \quad \boldsymbol{\delta}_3 = -a\mathbf{e}_y, \quad (1)$$

and the triangular Bravais lattice is spanned by the basis vectors

$$\mathbf{a}_1 = \sqrt{3}a\mathbf{e}_x \quad \text{and} \quad \mathbf{a}_2 = \frac{\sqrt{3}a}{2} (\mathbf{e}_x + \sqrt{3}\mathbf{e}_y). \quad (2)$$

The modulus of the basis vectors yields the lattice spacing,  $\tilde{a} = \sqrt{3}a = 0.24$  nm, and the area of the unit cell is  $A_{uc} = \sqrt{3}\tilde{a}^2/2 = 0.051$  nm<sup>2</sup>. The density of carbon atoms is, therefore,  $n_C = 2/A_{uc} = 39$  nm<sup>-2</sup> =  $3.9 \times 10^{15}$  cm<sup>-2</sup>. Because there is one  $\pi$  electron per carbon atom that is not involved in a covalent  $\sigma$  bond, there are as many valence electrons as carbon atoms, and their density is, thus,  $n_\pi = n_C = 3.9 \times 10^{15}$  cm<sup>-2</sup>. As discussed in detail below, this density is not equal to the carrier density in graphene, which one measures in electric transport measurements.

The reciprocal lattice, which is defined with respect to the triangular Bravais lattice, is depicted in Fig. 3 (b). It spanned by the vectors

$$\mathbf{a}_1^* = \frac{2\pi}{\sqrt{3}a} \left( \mathbf{e}_x - \frac{\mathbf{e}_y}{\sqrt{3}} \right) \quad \text{and} \quad \mathbf{a}_2^* = \frac{4\pi}{3a} \mathbf{e}_y. \quad (3)$$

Physically, all sites of the reciprocal lattice represent equivalent wave vectors. The first Brillouin zone [BZ, shaded region and thick part of the border of the hexagon in Fig. 3 (b)] is defined as the set of inequivalent points in reciprocal space, i.e. of points which may not be connected to one another by a reciprocal lattice vector. The long wavelength excitations are situated in the vicinity of the  $\Gamma$  point, in the center of the first BZ. Furthermore, one distinguishes the six corners of the first BZ, which consist of the inequivalent points  $K$  and  $K'$  represented by the vectors

$$\pm \mathbf{K} = \pm \frac{4\pi}{3\sqrt{3}a} \mathbf{e}_x. \quad (4)$$

The four remaining corners [shown in gray in Fig. 3 (b)] may indeed be connected to one of these points via a translation by a reciprocal lattice vector. These crystallographic points play an essential role in the electronic properties of graphene because their low-energy excitations are centered around the two points  $K$  and  $K'$ , as is discussed in detail in the following section. We emphasize, because of some confusion in the literature on this point, that the inequivalence of the two BZ corners,  $K$  and  $K'$ , has nothing to do with the presence of two sublattices,  $A$  and  $B$ , in the honeycomb lattice. The form of the BZ is an intrinsic property of the *Bravais* lattice, independent of the possible presence of more than one atom in the unit cell. For completeness, we have also shown, in Fig. 3 (b), the three crystallographically inequivalent  $M$  points in the middle of the BZ edges.

### C. Electronic Band Structure of Graphene

As we have discussed in the previous section, three electrons per carbon atom in graphene are involved in the formation of strong covalent  $\sigma$  bonds, and one electron per atom yields the  $\pi$  bonds. The  $\pi$  electrons happen to be those responsible for the electronic properties at low energies, whereas the  $\sigma$  electrons form energy bands far away from the Fermi energy (Saito *et al.*, 1998). This section of the introduction is, thus, devoted to a brief discussion of the energy bands of  $\pi$  electrons within the tight-binding approximation, which was originally calculated for the honeycomb lattice by P. R. Wallace in 1947 (Wallace, 1947).

#### 1. Tight-binding model for electrons on the honeycomb lattice

In the case of two atoms per unit cell, we may write down a trial wave function

$$\psi_{\mathbf{k}}(\mathbf{r}) = a_{\mathbf{k}}\psi_{\mathbf{k}}^{(A)}(\mathbf{r}) + b_{\mathbf{k}}\psi_{\mathbf{k}}^{(B)}(\mathbf{r}), \quad (5)$$

where  $a_{\mathbf{k}}$  and  $b_{\mathbf{k}}$  are complex functions of the quasi-momentum  $\mathbf{k}$ . Both  $\psi_{\mathbf{k}}^{(A)}(\mathbf{r})$  and  $\psi_{\mathbf{k}}^{(B)}(\mathbf{r})$  are Bloch functions with

$$\psi_{\mathbf{k}}^{(j)}(\mathbf{r}) = \sum_{\mathbf{R}_l} e^{i\mathbf{k}\cdot\mathbf{R}_l} \phi^{(j)}(\mathbf{r} + \boldsymbol{\delta}_j - \mathbf{R}_l), \quad (6)$$

where  $j = A/B$  labels the atoms on the two sublattices  $A$  and  $B$ , and  $\boldsymbol{\delta}_j$  is the vector which connects the sites of the underlying Bravais lattice with the site of the  $j$  atom within the unit cell. The  $\phi^{(j)}(\mathbf{r} + \boldsymbol{\delta}_j - \mathbf{R}_l)$  are atomic orbital wave functions for electrons that are in the vicinity of the  $j$  atom situated at the position  $\mathbf{R}_l - \boldsymbol{\delta}_j$  at the (Bravais) lattice site  $\mathbf{R}_l$ . Typically one chooses the sites of one of the sublattices, e.g. the  $A$  sublattice, to coincide with the sites of the Bravais lattice. Notice furthermore that there is some arbitrariness in the choice of the phase in Eq. (6) – instead of choosing  $\exp(i\mathbf{k}\cdot\mathbf{R}_l)$ , one may also have chosen  $\exp[i\mathbf{k}\cdot(\mathbf{R}_l - \boldsymbol{\delta}_j)]$ , for the atomic wave functions. The choice, however, does not affect the physical properties of the system because it simply leads to a redefinition of the weights  $a_{\mathbf{k}}$  and  $b_{\mathbf{k}}$  which acquire a different relative phase (Bena and Montambaux, 2009).

With the help of these wave functions, we may now search the solutions of the Schrödinger equation  $H\psi_{\mathbf{k}} = \epsilon_{\mathbf{k}}\psi_{\mathbf{k}}$ . Multiplication of the Schrödinger equation by  $\psi_{\mathbf{k}}^*$  from the left yields the equation  $\psi_{\mathbf{k}}^*H\psi_{\mathbf{k}} = \epsilon_{\mathbf{k}}\psi_{\mathbf{k}}^*\psi_{\mathbf{k}}$ , which may be rewritten in matrix form with the help of Eq. (5)

$$(a_{\mathbf{k}}^*, b_{\mathbf{k}}^*) \mathcal{H}_{\mathbf{k}} \begin{pmatrix} a_{\mathbf{k}} \\ b_{\mathbf{k}} \end{pmatrix} = \epsilon_{\mathbf{k}} (a_{\mathbf{k}}^*, b_{\mathbf{k}}^*) \mathcal{S}_{\mathbf{k}} \begin{pmatrix} a_{\mathbf{k}} \\ b_{\mathbf{k}} \end{pmatrix}. \quad (7)$$

Here, the Hamiltonian matrix is defined as

$$\mathcal{H}_{\mathbf{k}} \equiv \begin{pmatrix} \psi_{\mathbf{k}}^{(A)*} H \psi_{\mathbf{k}}^{(A)} & \psi_{\mathbf{k}}^{(A)*} H \psi_{\mathbf{k}}^{(B)} \\ \psi_{\mathbf{k}}^{(B)*} H \psi_{\mathbf{k}}^{(A)} & \psi_{\mathbf{k}}^{(B)*} H \psi_{\mathbf{k}}^{(B)} \end{pmatrix} = \mathcal{H}_{\mathbf{k}}^\dagger, \quad (8)$$

and the overlap matrix

$$\mathcal{S}_{\mathbf{k}} \equiv \begin{pmatrix} \psi_{\mathbf{k}}^{(A)*} \psi_{\mathbf{k}}^{(A)} & \psi_{\mathbf{k}}^{(A)*} \psi_{\mathbf{k}}^{(B)} \\ \psi_{\mathbf{k}}^{(B)*} \psi_{\mathbf{k}}^{(A)} & \psi_{\mathbf{k}}^{(B)*} \psi_{\mathbf{k}}^{(B)} \end{pmatrix} = \mathcal{S}_{\mathbf{k}}^\dagger \quad (9)$$

accounts for the non-orthogonality of the trial wave functions. The eigenvalues  $\epsilon_{\mathbf{k}}$  of the Schrödinger equation yield the electronic bands, and they may be obtained from the secular equation

$$\det [\mathcal{H}_{\mathbf{k}} - \epsilon_{\mathbf{k}}^\lambda \mathcal{S}_{\mathbf{k}}] = 0, \quad (10)$$

which needs to be satisfied for a non-zero solution of the wave functions, i.e. for  $a_{\mathbf{k}} \neq 0$  and  $b_{\mathbf{k}} \neq 0$ . The label  $\lambda$  denotes the energy bands, and it is clear that there are as many energy bands as solutions of the secular equation (10), i.e. two bands for the case of two atoms per unit cell.

*a. Formal solution.* Before turning to the specific case of graphene and its energy bands, we solve formally the secular equation for an arbitrary lattice with several atoms per unit cell. The Hamiltonian matrix (8) may be written, with the help of Eq. (6), as

$$\mathcal{H}_{\mathbf{k}}^{ij} = N \left( \epsilon_{\mathbf{k}}^{(j)} s_{\mathbf{k}}^{ij} + t_{\mathbf{k}}^{ij} \right) \quad (11)$$

where  $(\delta_{ij} \equiv \delta_j - \delta_i)$ ,

$$s_{\mathbf{k}}^{ij} \equiv \sum_{\mathbf{R}_l} e^{i\mathbf{k} \cdot \mathbf{R}_l} \int d^2r \phi^{(i)*}(\mathbf{r}) \phi^{(j)}(\mathbf{r} + \delta_{ij} - \mathbf{R}_l) = \frac{\mathcal{S}_{\mathbf{k}}^{ij}}{N} \quad (12)$$

and we have defined the *hopping matrix*

$$t_{\mathbf{k}}^{ij} \equiv \sum_{\mathbf{R}_l} e^{i\mathbf{k} \cdot \mathbf{R}_l} \int d^2r \phi^{(i)*}(\mathbf{r}) \Delta V \phi^{(j)}(\mathbf{r} + \delta_{ij} - \mathbf{R}_l). \quad (13)$$

Here,  $N$  is the number of unit cells, and we have separated the Hamiltonian  $H$  into an atomic orbital part  $H^a = -(\hbar^2/2m)\Delta + V(\mathbf{r} - \mathbf{R}_l + \delta_j)$ , which satisfies the eigenvalue equation  $H^a \phi^{(j)}(\mathbf{r} + \delta_j - \mathbf{R}_l) = \epsilon^{(j)} \phi^{(j)}(\mathbf{r} + \delta_j - \mathbf{R}_l)$  and a ‘‘perturbative part’’  $\Delta V$  which takes into account the potential term that arises from all other atoms different from that in the atomic orbital Hamiltonian. The last line in Eq. (11) has been obtained from the fact that the atomic wave functions  $\phi^{(i)}(\mathbf{r})$  are eigenstates of the atomic Hamiltonian  $H^a$  with the atomic energy  $\epsilon^{(i)}$  for an orbital of type  $i$ . This atomic energy plays the role of an onsite energy. The secular equation now reads  $\det[t_{\mathbf{k}}^{ij} - (\epsilon_{\mathbf{k}}^\lambda - \epsilon^{(j)})s_{\mathbf{k}}^{ij}] = 0$ . Notice that, if the atoms on the different sublattices are all of the same electronic configuration, one has  $\epsilon^{(i)} = \epsilon_0$  for all  $i$ , and one may omit this on-site energy, which yields only a constant and physically irrelevant shift of the energy bands.

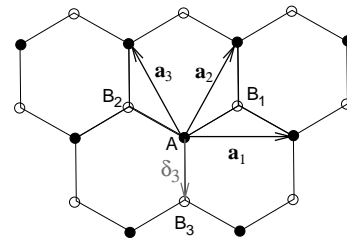


Figure 4 Tight-binding model for the honeycomb lattice.

*b. Solution for graphene with nearest-neighbor and next-nearest-neighbor hopping.* After these formal considerations, we now study the particular case of the tight-binding model on the honeycomb lattice, which yields, to great accuracy, the  $\pi$  energy bands of graphene. Because all atomic orbitals are  $p_z$  orbitals of carbon atoms, we may omit the onsite energy  $\epsilon_0$ , as discussed in the last paragraph. We choose the Bravais lattice vectors to be those of the A sublattice, i.e.  $\delta_A = 0$ , and the equivalent site on the B sublattice is obtained by the displacement  $\delta_B = \delta_{AB} = \delta_3$  (see Fig. 4). The  $nn$  hopping amplitude is given by the expression

$$t \equiv \int d^2r \phi^{A*}(\mathbf{r}) \Delta V \phi^B(\mathbf{r} + \delta_3), \quad (14)$$

and we also take into account next-nearest neighbor ( $nnn$ ) hopping which connects neighboring sites on the *same* sublattice

$$t_{nnn} \equiv \int d^2r \phi^{A*}(\mathbf{r}) \Delta V \phi^A(\mathbf{r} + \mathbf{a}_1) \quad (15)$$

Notice that one may have chosen any other vector  $\delta_j$  or  $\mathbf{a}_2$ , respectively, in the calculation of the hopping amplitudes. Because of the normalization of the atomic wave functions, we have  $\int d^2r \phi^{(j)*}(\mathbf{r}) \phi^{(j)}(\mathbf{r}) = 1$ , and we consider furthermore the overlap correction between orbitals on  $nn$  sites,

$$s \equiv \int d^2r \phi^{A*}(\mathbf{r}) \phi^B(\mathbf{r} + \delta_3). \quad (16)$$

We neglect overlap corrections between all other orbitals which are not  $nn$ , as well as hopping amplitudes for larger distances than  $nnn$ .

If we now consider an arbitrary site  $A$  on the A sublattice (Fig. 4), we may see that the off-diagonal terms of the hopping matrix (13) consist of three terms corresponding to the  $nn$   $B_1$ ,  $B_2$ , and  $B_3$ , all of which have the same hopping amplitude  $t$ . However, only the site  $B_3$  is described by the same lattice vector (shifted by  $\delta_3$ ) as the site  $A$  and thus yields a zero phase to the hopping matrix. The sites  $B_1$  and  $B_2$  correspond to lattice vectors shifted by  $\mathbf{a}_2$  and  $\mathbf{a}_3 \equiv \mathbf{a}_2 - \mathbf{a}_1$ , respectively. Therefore, they contribute a phase factor  $\exp(i\mathbf{k} \cdot \mathbf{a}_2)$  and  $\exp(i\mathbf{k} \cdot \mathbf{a}_3)$ , respectively. The off-diagonal elements of the hopping

matrix may then be written as<sup>3</sup>  $t_{\mathbf{k}}^{AB} = t\gamma_{\mathbf{k}}^* = (t_{\mathbf{k}}^{BA})^*$ , as well as those of the overlap matrix  $s_{\mathbf{k}}^{AB} = s\gamma_{\mathbf{k}}^* = (s_{\mathbf{k}}^{BA})^*$ , ( $s_{\mathbf{k}}^{AA} = s_{\mathbf{k}}^{BB} = 1$ , due to the above-mentioned normalization of the atomic wave functions), where we have defined the sum of the  $nn$  phase factors

$$\gamma_{\mathbf{k}} \equiv 1 + e^{i\mathbf{k}\cdot\mathbf{a}_2} + e^{i\mathbf{k}\cdot\mathbf{a}_3}. \quad (17)$$

The  $nnn$  hopping amplitudes yield the diagonal elements of the hopping matrix,

$$t_{\mathbf{k}}^{AA} = t_{\mathbf{k}}^{BB} = 2t_{nnn} \sum_{i=1}^3 \cos(\mathbf{k} \cdot \mathbf{a}_i) = t_{nnn} (|\gamma_{\mathbf{k}}|^2 - 3), \quad (18)$$

and one obtains, thus, the secular equation

$$\det \begin{bmatrix} t_{\mathbf{k}}^{AA} - \epsilon_{\mathbf{k}} & (t - s\epsilon_{\mathbf{k}})\gamma_{\mathbf{k}}^* \\ (t - s\epsilon_{\mathbf{k}})\gamma_{\mathbf{k}} & t_{\mathbf{k}}^{AA} - \epsilon_{\mathbf{k}} \end{bmatrix} = 0 \quad (19)$$

with the two solutions ( $\lambda = \pm$ )

$$\epsilon_{\mathbf{k}}^{\lambda} = \frac{t_{\mathbf{k}}^{AA} + \lambda t |\gamma_{\mathbf{k}}|}{1 + \lambda s |\gamma_{\mathbf{k}}|}. \quad (20)$$

This expression may be expanded under the reasonable assumptions  $s \ll 1$  and  $t_{nnn} \ll t$ , which we further justify at the end of the paragraph,

$$\begin{aligned} \epsilon_{\mathbf{k}}^{\lambda} &\simeq t_{\mathbf{k}}^{AA} + \lambda t |\gamma_{\mathbf{k}}| - st |\gamma_{\mathbf{k}}|^2 = t'_{nnn} |\gamma_{\mathbf{k}}|^2 + \lambda t |\gamma_{\mathbf{k}}| \\ &= t'_{nnn} \left[ 3 + 2 \sum_{i=1}^3 \cos(\mathbf{k} \cdot \mathbf{a}_i) \right] \\ &\quad + \lambda t \sqrt{3 + 2 \sum_{i=1}^3 \cos(\mathbf{k} \cdot \mathbf{a}_i)}, \end{aligned} \quad (21)$$

where we have defined the effective  $nnn$  hopping amplitude  $t'_{nnn} \equiv t_{nnn} - st$ , and we have omitted the unimportant constant  $-3t_{nnn}$  in the second step. Therefore, the overlap corrections simply yield a renormalization of the  $nnn$  hopping amplitudes. The hopping amplitudes may be determined by fitting the energy dispersion (21) obtained within the tight-binding approximation to those calculated numerically in more sophisticated band-structure calculations (Partoens and Peeters, 2006) or to spectroscopic measurements (Mucha-Kruczyński *et al.*, 2008). These yield a value of  $t \simeq -3$  eV for the  $nn$  hopping amplitude and  $t'_{nnn} \simeq 0.1t$ , which justifies the above-mentioned expansion for  $t'_{nnn}/t \ll 1$ . Notice that this fitting procedure does not allow for a distinction between the “true”  $nnn$  hopping amplitude  $t_{nnn}$  and the contribution from the overlap correction  $-st$ . We, therefore, omit this distinction in the following discussion and drop the prime at the effective  $nnn$  hopping amplitude, but one should keep in mind that it is an effective parameter with a contribution from  $nn$  overlap corrections.

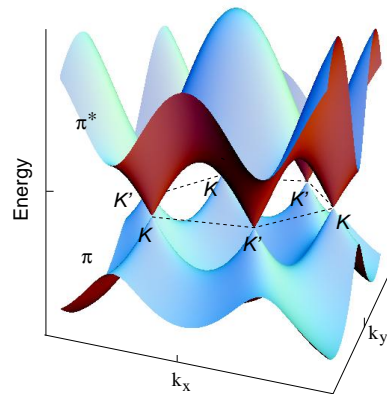


Figure 5 Energy dispersion as a function of the wave-vector components  $k_x$  and  $k_y$ , obtained within the tight-binding approximation, for  $t_{nnn}/t = 0.1$ . One distinguishes the valence ( $\pi$ ) band from the conduction ( $\pi^*$ ) band. The Fermi level is situated at the points where the  $\pi$  band touches the  $\pi^*$  band. The energy is measured in units of  $t$  and the wave vector in units of  $1/a$ .

*c. Energy dispersion of  $\pi$  electrons in graphene.* The energy dispersion (21) is plotted in Fig. 5 for  $t_{nnn}/t = 0.1$ . It consists of two bands, labeled by the index  $\lambda = \pm$ , each of which contains the same number of states. Because each carbon atom contributes one  $\pi$  electron and each electron may occupy either a spin-up or a spin-down state, the lower band with  $\lambda = -$  (the  $\pi$  or valence band) is completely filled and that with  $\lambda = +$  (the  $\pi^*$  or conduction band) completely empty. The Fermi level is, therefore, situated at the points, called *Dirac points*, where the  $\pi$  band touches the  $\pi^*$  band. Notice that only if  $t_{nnn} = 0$  the energy dispersion (21) is electron-hole symmetric, i.e.  $\epsilon_{\mathbf{k}}^{\lambda} = -\epsilon_{\mathbf{k}}^{-\lambda}$ . This means that  $nnn$  hopping and  $nn$  overlap corrections break the electron-hole symmetry. The Dirac points are situated at the points  $\mathbf{k}^D$  where the energy dispersion (21) is zero,

$$\epsilon_{\mathbf{k}^D}^{\lambda} = 0. \quad (22)$$

Eq. (22) is satisfied when  $\gamma_{\mathbf{k}^D} = 0$ , i.e. when

$$\begin{aligned} \text{Re}\gamma_{\mathbf{k}^D} &= 1 + \cos \left[ \frac{\sqrt{3}a}{2} (k_x^D + \sqrt{3}k_y^D) \right] \\ &\quad + \cos \left[ \frac{\sqrt{3}a}{2} (-k_x^D + \sqrt{3}k_y^D) \right] = 0 \end{aligned} \quad (23)$$

and, equally,

$$\begin{aligned} \text{Im}\gamma_{\mathbf{k}^D} &= \sin \left[ \frac{\sqrt{3}a}{2} (k_x^D + \sqrt{3}k_y^D) \right] \\ &\quad + \sin \left[ \frac{\sqrt{3}a}{2} (-k_x^D + \sqrt{3}k_y^D) \right] = 0. \end{aligned} \quad (24)$$

<sup>3</sup> The hopping matrix element  $t_{\mathbf{k}}^{AB}$  corresponds to a hopping from the  $B$  to the  $A$  sublattice.

The last equation may be satisfied by the choice  $k_y^D = 0$ , and Eq. (23), thus, when

$$1 + 2 \cos \left( \frac{\sqrt{3}a}{2} k_x^D \right) = 0 \quad \Rightarrow \quad k_x^D = \pm \frac{4\pi}{3\sqrt{3}a}. \quad (25)$$

Comparison with Eq. (4) shows that there are, thus, two inequivalent Dirac points  $D$  and  $D'$ , which are situated at the points  $K$  and  $K'$ , respectively,

$$\mathbf{k}^D = \pm \mathbf{K} = \pm \frac{4\pi}{3\sqrt{3}a} \mathbf{e}_x. \quad (26)$$

Although situated at the same position in the first BZ, it is useful to make a clear conceptual distinction between the Dirac points  $D$  and  $D'$ , which are defined as the contact points between the two bands  $\pi$  and  $\pi^*$ , and the crystallographic points  $K$  and  $K'$ , which are defined as the corners of the first BZ. There are, indeed, situations where the Dirac points move away from the points  $K$  and  $K'$ , as we will discuss in Sec. I.D.

Notice that the band Hamiltonian (8) respects time-reversal symmetry,  $\mathcal{H}_{\mathbf{k}} = \mathcal{H}_{-\mathbf{k}}^*$ , which implies  $\epsilon_{-\mathbf{k}} = \epsilon_{\mathbf{k}}$  for the dispersion relation. Therefore, if  $\mathbf{k}^D$  is a solution of  $\epsilon_{\mathbf{k}} = 0$ , so is  $-\mathbf{k}^D$ , and Dirac points thus necessarily occur in pairs. In graphene, there is one pair of Dirac points, and the zero-energy states are, therefore, doubly degenerate. One speaks of a twofold *valley degeneracy*, which survives when we consider low-energy electronic excitations that are restricted to the vicinity of the Dirac points, as is discussed in Sec. I.C.2.

*d. Effective tight-binding Hamiltonian.* Before considering the low-energy excitations and the continuum limit, it is useful to define an effective tight-binding Hamiltonian,

$$\mathcal{H}_{\mathbf{k}} \equiv t_{nnn} |\gamma_{\mathbf{k}}|^2 \mathbb{1} + t \begin{pmatrix} 0 & \gamma_{\mathbf{k}}^* \\ \gamma_{\mathbf{k}} & 0 \end{pmatrix}. \quad (27)$$

Here,  $\mathbb{1}$  represents the  $2 \times 2$  one-matrix

$$\mathbb{1} = \begin{pmatrix} 1 & 0 \\ 0 & 1 \end{pmatrix}. \quad (28)$$

This Hamiltonian effectively omits the problem of non-orthogonality of the wave functions by a simple renormalization of the  $nnn$  hopping amplitude, as alluded to above. It is therefore simpler to treat than the original one (8) the eigenvalue equation of which involves the overlap matrix  $\mathcal{S}_{\mathbf{k}}$ , while it yields the same dispersion relation (21). The eigenstates of the effective Hamiltonian (27) are the spinors

$$\Psi_{\mathbf{k}}^{\lambda} = \begin{pmatrix} a_{\mathbf{k}}^{\lambda} \\ b_{\mathbf{k}}^{\lambda} \end{pmatrix}, \quad (29)$$

the components of which are the probability amplitudes of the Bloch wave function (5) on the two different sublattices A and B. They may be determined by considering

the eigenvalue equation  $\mathcal{H}_{\mathbf{k}}(t_{nnn} = 0)\Psi_{\mathbf{k}}^{\lambda} = \lambda t |\gamma_{\mathbf{k}}| \Psi_{\mathbf{k}}^{\lambda}$ , which does not take into account the  $nnn$  hopping correction. Indeed, these eigenstates are also those of the Hamiltonian with  $t_{nnn} \neq 0$  because the  $nnn$  term is proportional to the one-matrix  $\mathbb{1}$ . The solution of the eigenvalue equation (29) yields

$$a_{\mathbf{k}}^{\lambda} = \lambda \frac{\gamma_{\mathbf{k}}^*}{|\gamma_{\mathbf{k}}|} b_{\mathbf{k}}^{\lambda} = \lambda e^{-i\varphi_{\mathbf{k}}} b_{\mathbf{k}}^{\lambda} \quad (30)$$

and, thus, the eigenstates

$$\Psi_{\mathbf{k}}^{\lambda} = \frac{1}{\sqrt{2}} \begin{pmatrix} 1 \\ \lambda e^{i\varphi_{\mathbf{k}}} \end{pmatrix}, \quad (31)$$

where  $\varphi_{\mathbf{k}} = \arctan(\text{Im}\gamma_{\mathbf{k}}/\text{Re}\gamma_{\mathbf{k}})$ .

As one may have expected, the spinor represents an equal probability to find an electron in the state  $\Psi_{\mathbf{k}}^{\lambda}$  on the A as on the B sublattice because both sublattices are built from carbon atoms with the same onsite energy  $\epsilon^{(i)}$ .

## 2. Continuum limit

In order to describe the low-energy excitations, i.e. electronic excitations with an energy that is much smaller than the band width  $\sim |t|$ , one may restrict the excitations to quantum states in the vicinity of the Dirac points and expand the energy dispersion around  $\pm \mathbf{K}$ . The wave vector is, thus, decomposed as  $\mathbf{k} = \pm \mathbf{K} + \mathbf{q}$ , where  $|\mathbf{q}| \ll |\mathbf{K}| \sim 1/a$ . The small parameter, which governs the expansion of the energy dispersion, is therefore  $|\mathbf{q}|a \ll 1$ .

It is evident from the form of the energy dispersion (21) and the effective Hamiltonian that the basic entity to be expanded is the sum of the phase factors  $\gamma_{\mathbf{k}}$ . As we have already mentioned, there is some arbitrariness in the definition of  $\gamma_{\mathbf{k}}$ , as a consequence of the arbitrary choice of the relative phase between the two sublattice components – indeed, a change  $\gamma_{\mathbf{k}} \rightarrow \gamma_{\mathbf{k}} \exp(i f_{\mathbf{k}})$  in Eq. (17) for a real and non-singular function  $f_{\mathbf{k}}$  does not affect the dispersion relation (21), which only depends on the modulus of the phase-factor sum. For the series expansion, it turns out to be more convenient not to use the expression (17), but one with  $f_{\mathbf{k}} = \mathbf{k} \cdot \boldsymbol{\delta}_3$ , which renders the expression more symmetric (Bena and Montambaux, 2009),

$$e^{i\mathbf{k} \cdot \boldsymbol{\delta}_3} \gamma_{\mathbf{k}} = e^{i\mathbf{k} \cdot \boldsymbol{\delta}_1} + e^{i\mathbf{k} \cdot \boldsymbol{\delta}_2} + e^{i\mathbf{k} \cdot \boldsymbol{\delta}_3} \quad (32)$$

In the series expansion, we need to distinguish further-

more the sum at the  $K$  point from that at the  $K'$  point,

$$\begin{aligned}\gamma_{\mathbf{q}}^{\pm} &\equiv e^{i\mathbf{k}\cdot\boldsymbol{\delta}_3}\gamma_{\mathbf{k}=\pm\mathbf{K}+\mathbf{q}} = \sum_{j=1}^3 e^{\pm i\mathbf{K}\cdot\boldsymbol{\delta}_j} e^{i\mathbf{q}\cdot\boldsymbol{\delta}_j} \\ &\simeq e^{\pm i2\pi/3} \left[ 1 + i\mathbf{q}\cdot\boldsymbol{\delta}_1 - \frac{1}{2}(\mathbf{q}\cdot\boldsymbol{\delta}_1)^2 \right] \\ &\quad + e^{\mp i2\pi/3} \left[ 1 + i\mathbf{q}\cdot\boldsymbol{\delta}_2 - \frac{1}{2}(\mathbf{q}\cdot\boldsymbol{\delta}_2)^2 \right] \\ &\quad + \left[ 1 + i\mathbf{q}\cdot\boldsymbol{\delta}_3 - \frac{1}{2}(\mathbf{q}\cdot\boldsymbol{\delta}_3)^2 \right] \\ &= \gamma_{\mathbf{q}}^{\pm(0)} + \gamma_{\mathbf{q}}^{\pm(1)} + \gamma_{\mathbf{q}}^{\pm(2)}\end{aligned}\quad (33)$$

By definition of the Dirac points and their position at the BZ corners  $K$  and  $K'$ , we have  $\gamma_{\mathbf{q}}^{\pm(0)} = \gamma_{\pm\mathbf{K}} = 0$ . We limit the expansion to second order in  $|\mathbf{q}|a$ .

a. *First order in  $|\mathbf{q}|a$ .* The first-order term is given by

$$\begin{aligned}\gamma_{\mathbf{q}}^{\pm(1)} &= i\frac{a}{2} \left[ (\sqrt{3}q_x + q_y)e^{\pm i2\pi/3} - (\sqrt{3}q_x - q_y)e^{\mp i2\pi/3} \right] \\ &\quad - iq_y a = \mp \frac{3a}{2}(q_x \pm iq_y),\end{aligned}\quad (34)$$

which is obtained with the help of  $\sin(\pm 2\pi/3) = \pm\sqrt{3}/2$  and  $\cos(\pm 2\pi/3) = -1/2$ . This yields the effective low-energy Hamiltonian

$$\mathcal{H}_{\mathbf{q}}^{\text{eff},\xi} = \xi \hbar v_F (q_x \sigma^x + \xi q_y \sigma^y), \quad (35)$$

where we have defined the Fermi velocity<sup>4</sup>

$$v_F \equiv -\frac{3ta}{2\hbar} = \frac{3|t|a}{2\hbar} \quad (36)$$

and used the Pauli matrices

$$\sigma^x = \begin{pmatrix} 0 & 1 \\ 1 & 0 \end{pmatrix} \quad \text{and} \quad \sigma^y = \begin{pmatrix} 0 & -i \\ i & 0 \end{pmatrix}. \quad (37)$$

Furthermore, we have introduced the *valley pseudospin*  $\xi = \pm$ , where  $\xi = +$  denotes the  $K$  point at  $+\mathbf{K}$  and  $\xi = -$  the  $K'$  point at  $-\mathbf{K}$  modulo a reciprocal lattice vector. The low-energy Hamiltonian (35) does not take into account *nnn*-hopping corrections, which are proportional to  $|\gamma_{\mathbf{k}}|^2$  and, thus, occur only in the second-order expansion of the energy dispersion [at order  $\mathcal{O}(|\mathbf{q}|a)^2$ ]. The energy dispersion (21) therefore reads

$$\epsilon_{\mathbf{q},\xi=\pm}^{\lambda} = \lambda \hbar v_F |\mathbf{q}|, \quad (38)$$

independent of the valley pseudospin  $\xi$ . We have already alluded to this twofold valley degeneracy in Sec. I.C.1, in

the framework of the discussion of the zero-energy states at the BZ corners. From Eq. (38) it is apparent that the continuum limit  $|\mathbf{q}|a \ll 1$  coincides with the limit  $|\epsilon| \ll |t|$ , as described above, because  $|\epsilon_{\mathbf{q}}| = 3ta|\mathbf{q}|/2 \ll |t|$  then.

It is convenient to swap the spinor components at the  $K'$  point (for  $\xi = -$ ),

$$\Psi_{\mathbf{k},\xi=+} = \begin{pmatrix} \psi_{\mathbf{k},+}^A \\ \psi_{\mathbf{k},+}^B \end{pmatrix}, \quad \Psi_{\mathbf{k},\xi=-} = \begin{pmatrix} \psi_{\mathbf{k},-}^B \\ \psi_{\mathbf{k},-}^A \end{pmatrix}, \quad (39)$$

i.e. to invert the role of the two sublattices. In this case, the effective low-energy Hamiltonian may be represented as

$$\mathcal{H}_{\mathbf{q}}^{\text{eff},\xi} = \xi \hbar v_F (q_x \sigma^x + q_y \sigma^y) = \hbar v_F \tau^z \otimes \mathbf{q} \cdot \boldsymbol{\sigma}, \quad (40)$$

i.e. as two copies of the *2D Dirac Hamiltonian*  $H_D = v_F \mathbf{p} \cdot \boldsymbol{\sigma}$  (with the momentum  $\mathbf{p} = \hbar \mathbf{q}$ ), where we have introduced the four-spinor representation

$$\Psi_{\mathbf{q}} = \begin{pmatrix} \psi_{\mathbf{q},+}^A \\ \psi_{\mathbf{q},+}^B \\ \psi_{\mathbf{q},-}^B \\ \psi_{\mathbf{q},-}^A \end{pmatrix} \quad (41)$$

in the last line via the  $4 \times 4$  matrices

$$\tau^z \otimes \boldsymbol{\sigma} = \begin{pmatrix} \boldsymbol{\sigma} & 0 \\ 0 & -\boldsymbol{\sigma} \end{pmatrix}, \quad (42)$$

and  $\boldsymbol{\sigma} \equiv (\sigma^x, \sigma^y)$ . In this four-spinor representation, the first two components represent the lattice components at the  $K$  point and the last two components those at the  $K'$  point. We emphasise that one must clearly distinguish both types of pseudospin: (a) the *sublattice pseudospin* is represented by the Pauli matrices  $\sigma^j$ , where ‘‘spin up’’ corresponds to the component on one sublattice and ‘‘spin down’’ to that on the other one. A rotation within the  $\text{SU}(2)$  sublattice-pseudospin space yields the band indices  $\lambda = \pm$ , and the band index is, thus, intimately related to the sublattice pseudospin. (b) The *valley pseudospin*, which is described by a second set of Pauli matrices  $\tau^j$ , the  $z$ -component of which appears in the Hamiltonian (40), is due to the twofold valley degeneracy and is only indirectly related to the presence of two sublattices.

The eigenstates of the Hamiltonian (40) are the four-spinors

$$\Psi_{\mathbf{q},\lambda}^{\xi=+} = \frac{1}{\sqrt{2}} \begin{pmatrix} 1 \\ \lambda e^{i\varphi_{\mathbf{q}}} \\ 0 \\ 0 \end{pmatrix}, \quad \Psi_{\mathbf{q},\lambda}^{\xi=-} = \frac{1}{\sqrt{2}} \begin{pmatrix} 0 \\ 0 \\ 1 \\ -\lambda e^{i\varphi_{\mathbf{q}}} \end{pmatrix}, \quad (43)$$

where we have, now,

$$\varphi_{\mathbf{q}} = \arctan \left( \frac{q_y}{q_x} \right). \quad (44)$$

<sup>4</sup> The minus sign in the definition is added to render the Fermi velocity positive because the hopping parameter  $t \simeq -3$  eV happens to be negative, as mentioned in the last section.



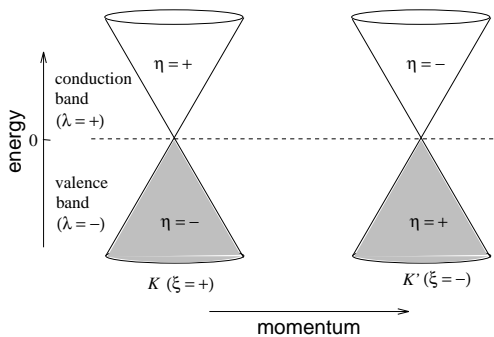


Figure 6 Relation between band index  $\lambda$ , valley pseudospin  $\xi$ , and chirality  $\eta$  in graphene.

*b. Chirality.* In high-energy physics, one defines the helicity of a particle as the projection of its spin onto the direction of propagation (Weinberg, 1995),

$$\eta_{\mathbf{q}} = \frac{\mathbf{q} \cdot \boldsymbol{\sigma}}{|\mathbf{q}|}, \quad (45)$$

which is a Hermitian and unitary operator with the eigenvalues  $\eta = \pm$ ,  $\eta_{\mathbf{q}}|\eta = \pm\rangle = \pm|\eta = \pm\rangle$ . Notice that  $\boldsymbol{\sigma}$  describes, in this case, the true physical spin of the particle. In the absence of a mass term, the helicity operator commutes with the Dirac Hamiltonian, and the helicity is, therefore, a good quantum number, e.g. in the description of neutrinos, which have approximately zero mass. One finds indeed, in nature, that all neutrinos are “left-handed” ( $\eta = -$ ), i.e. their spin is antiparallel to their momentum, whereas all anti-neutrinos are “right-handed” ( $\eta = +$ ).

For massive Dirac particles, the helicity operator (45) no longer commutes with the Hamiltonian. One may, however, decompose a quantum state  $|\Psi\rangle$  describing a massive Dirac particle into its *chiral* components, with the help of the projectors

$$|\Psi_L\rangle = \frac{1 - \eta_{\mathbf{q}}}{2} |\Psi\rangle \quad \text{and} \quad |\Psi_R\rangle = \frac{1 + \eta_{\mathbf{q}}}{2} |\Psi\rangle. \quad (46)$$

In the case of massless Dirac particles, with a well-defined helicity  $|\Psi\rangle = |\eta = \pm\rangle$ , one simply finds

$$|\Psi_L^+\rangle = \frac{1 - \eta_{\mathbf{q}}}{2} |+\rangle = 0, \quad |\Psi_R^+\rangle = \frac{1 + \eta_{\mathbf{q}}}{2} |+\rangle = |+\rangle \quad (47)$$

and

$$|\Psi_L^-\rangle = \frac{1 - \eta_{\mathbf{q}}}{2} |-\rangle = |-\rangle, \quad |\Psi_R^-\rangle = \frac{1 + \eta_{\mathbf{q}}}{2} |-\rangle = 0, \quad (48)$$

such that one may then identify helicity and chirality. Because we are concerned with massless particles in the context of graphene, we make this identification in the remainder of this review and use the term *chirality*.

For the case of graphene, one may use the same definition (45), but the Pauli matrices define now the sublattice pseudospin instead of the true spin. The operator

$\eta_{\mathbf{q}}$  clearly commutes with the massless 2D Dirac Hamiltonian (40), and one may even express the latter as

$$\mathcal{H}_{\mathbf{q}}^{\text{eff},\xi} = \xi \hbar v_F |\mathbf{q}| \eta_{\mathbf{q}}, \quad (49)$$

which takes into account the two-fold valley degeneracy, in terms of the valley pseudospin  $\xi = \pm$ . The band index  $\lambda$ , which describes the valence and the conduction band, is therefore entirely determined by the chirality and the valley pseudospin, and one finds

$$\lambda = \xi \eta, \quad (50)$$

which is depicted in Fig. 6.

We notice finally that the chirality is a preserved quantum number in elastic scattering processes induced by impurity potentials  $V_{\text{imp}} = V(\mathbf{r}) \mathbb{1}$  that vary smoothly on the lattice scale. In this case, inter-valley scattering is suppressed, and the chirality thus conserved, as a consequence of Eq. (50). This effect gives rise to the absence of backscattering in graphene (Shon and Ando, 1998) and is at the origin of Klein tunneling according to which a massless Dirac particle is fully transmitted, under normal incidence, through a high electrostatic barrier without being reflected (Katsnelson *et al.*, 2006). This rather counter-intuitive result was first considered as a paradox and led to the formulation of a *charged vacuum* in the potential barrier (Klein, 1929), which may be identified in the framework of band theory with a Fermi level in the valence band.

*c. Higher orders in  $|\mathbf{q}|a$ .* Although most of the fundamental properties of graphene are captured within the effective model obtained at first order in the expansion of the energy dispersion, it is useful to take into account second-order terms. These corrections include *nnn* hopping corrections and off-diagonal second-order contributions from the expansion of  $\gamma_{\mathbf{k}}$ . The latter yield the so-called *trigonal warping*, which consists of an anisotropy in the energy dispersion around the Dirac points.

The diagonal second-order term, which stems from the *nnn* hopping, is readily obtained from Eq. (34),

$$\mathcal{H}_{nnn}^{\xi} = t_{nnn} |\gamma_{\mathbf{q}}^{\xi}|^2 \mathbb{1} \simeq t_{nnn} |\gamma_{\mathbf{q}}^{\xi(1)}|^2 \mathbb{1} = \frac{9a^2}{4} t_{nnn} |\mathbf{q}|^2 \mathbb{1}, \quad (51)$$

independent of the valley index  $\xi$ .

The off-diagonal second-order terms are  $t\gamma_{\mathbf{q}}^{\xi(2)} = -\hbar v_F a (q_x - i\xi q_y)^2 / 4$ . Notice that there is a natural energy hierarchy between the diagonal and off-diagonal second-order terms when compared to the leading linear term; whereas the off-diagonal terms are on the order  $\mathcal{O}(|\mathbf{q}|a)$  as compared to the energy scale  $\hbar v_F |\mathbf{q}|$ , the diagonal term is on the order  $\mathcal{O}((t_{nnn}/t)|\mathbf{q}|a)$  and thus roughly an order of magnitude smaller. We therefore take into account also the off-diagonal third order term  $t\gamma_{\mathbf{q}}^{\xi(3)} = -\xi \hbar v_F a^2 (q_x + i\xi q_y) |\mathbf{q}|^2 / 8$ , which also needs to be considered when calculating the high-energy corrections

of the energy levels in a magnetic field (see Sec. II.B). Up to third order, the off-diagonal terms therefore read

$$t\gamma_{\mathbf{q}}^{\xi} = \xi\hbar v_F \left[ (q_x + i\xi q_y) - \xi \frac{a}{4} (q_x - i\xi q_y)^2 - \frac{a^2}{8} |\mathbf{q}|^2 (q_x + i\xi q_y) \right], \quad (52)$$

where one may omit the valley-dependent sign before the  $y$ -components of the wave vector by sweeping the sublattice components in the spinors when changing the valley.

In order to appreciate the influence of the second-order off-diagonal terms on the energy bands, we need to calculate the modulus of  $\gamma_{\mathbf{q}}^{\xi}$ ,

$$|\gamma_{\mathbf{q}}^{\xi}| \simeq \frac{3a}{2} |\mathbf{q}| \left[ 1 - \xi \frac{|\mathbf{q}|a}{4} \cos(3\varphi_{\mathbf{q}}) \right], \quad (53)$$

where we have used the parametrization  $q_x = |\mathbf{q}| \cos \varphi_{\mathbf{q}}$  and  $q_y = |\mathbf{q}| \sin \varphi_{\mathbf{q}}$ , and where we have restricted the expansion to second order. Finally, the energy dispersion (21) expanded to second order in  $|\mathbf{q}|a$  reads

$$\epsilon_{\mathbf{q},\xi}^{\lambda} = \frac{9a^2}{4} t_{nnn} |\mathbf{q}|^2 + \lambda \hbar v_F |\mathbf{q}| \left[ 1 - \xi \frac{|\mathbf{q}|a}{4} \cos(3\varphi_{\mathbf{q}}) \right]. \quad (54)$$

As mentioned in Sec. I.C.1, it is apparent from Eq. (54) that the  $nnn$  correction breaks the electron-hole symmetry  $\epsilon_{\mathbf{q},\xi}^{-\lambda} = -\epsilon_{\mathbf{q},\xi}^{\lambda}$ . This is, however, a rather small correction, of order  $|\mathbf{q}|at_{nnn}/t$ , to the first-order effective Hamiltonian (40). The second-order expansion of the phase factor sum  $\gamma_{\mathbf{q}}$  yields a more relevant correction – the third term in Eq. (54), that is of order  $|\mathbf{q}|a \gg |\mathbf{q}|at_{nnn}/t$  – to the linear theory. It depends explicitly on the valley pseudospin  $\xi$  and renders the energy dispersion anisotropic in  $\mathbf{q}$  around the  $K$  and  $K'$  point. The tripling of the period, due to the term  $\cos(3\varphi_{\mathbf{q}})$ , is a consequence of the symmetry of the underlying lattice and is precisely the origin of trigonal warping.

The trigonal warping of the dispersion relation is visualized in Fig. 7, where we have plotted the contours of constant (positive) energy in Fourier space. The closed energy contours around the  $K$  and  $K'$  points at low energy are separated by the high-energy contours around the  $\Gamma$  point by the dashed lines in Fig. 7 (a) at energy  $|t + t_{nnn}|$  the crossing points of which correspond to the  $M$  points. As mentioned above, the dispersion relation has saddle points at these points at the border of the first BZ, which yield van Hove singularities in the density of states. In Fig. 7 (b), we compare constant-energy contours of the full dispersion relation to those obtained from Eq. (54) calculated within a second-order expansion. The contours are indistinguishable for an energy of  $\epsilon = |t|/3 \simeq 1$  eV, and the continuum limit yields rather accurate results up to energies as large as 2 eV. Notice that, in today's exfoliated graphene samples on  $\text{SiO}_2$  substrates, one may probe, by field-effect doping of the graphene sheet, energies which are on the order of 100 meV. Above these energies the capacitor breaks

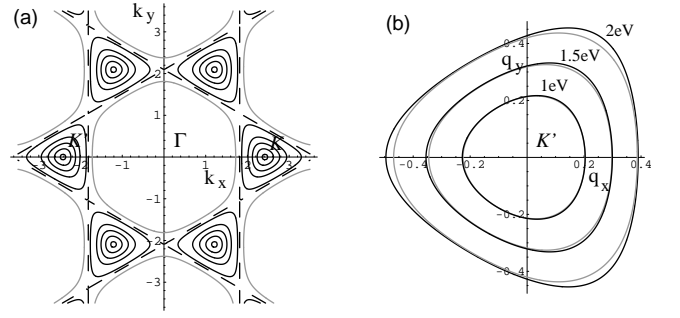


Figure 7 Contours of constant (positive) energy in reciprocal space. (a) Contours obtained from the full dispersion relation (21). The dashed line corresponds to the energy  $t + t_{nnn}$ , which separates closed orbits around the  $K$  and  $K'$  points (black lines, with energy  $\epsilon < t + t_{nnn}$ ) from those around the  $\Gamma$  point (gray line, with energy  $\epsilon > t + t_{nnn}$ ). (b) Comparison of the contours at energy  $\epsilon = 1$  eV, 1.5 eV, and 2 eV around the  $K'$  point. The black lines correspond to the energies calculated from the full dispersion relation (21) and the gray ones to those calculated to second order within the continuum limit (54).

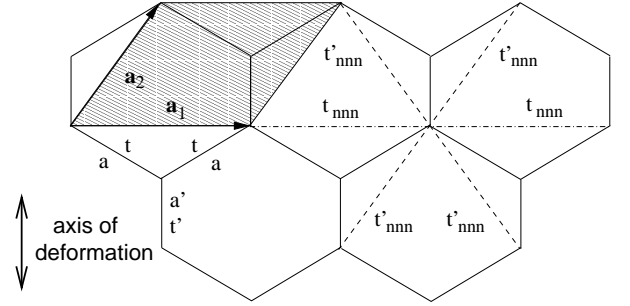


Figure 8 Quinoid-type deformation of the honeycomb lattice – the bonds parallel to the deformation axis (double arrow) are modified. The shaded region indicates the unit cell of the oblique lattice, spanned by the lattice vectors  $\mathbf{a}_1$  and  $\mathbf{a}_2$ . Dashed and dashed-dotted lines indicate next-nearest neighbors, with characteristic hopping integrals  $t_{nnn}$  and  $t'_{nnn}$ , respectively, which are different due to the lattice deformation.

down, and Fig. 7 (a) indicates that the continuum limit (54) yields extremely accurate results at these energies.

We finally mention that, when higher-order terms in  $|\mathbf{q}|a$  are taken into account, the chirality operator (45) no longer commutes with the Hamiltonian. Chirality is therefore only a good quantum number in the vicinity of the Dirac points.

#### D. Deformed Graphene

In the previous section, we have considered a perfect honeycomb lattice which is invariant under a  $2\pi/3$  rotation. As a consequence, all hopping parameters along the  $nn$  bonds  $\delta_j$  were equal. An interesting situation arises when the graphene sheet is deformed, such that rotation symmetry is broken. In order to illustrate the consequences, we may apply a uniax-

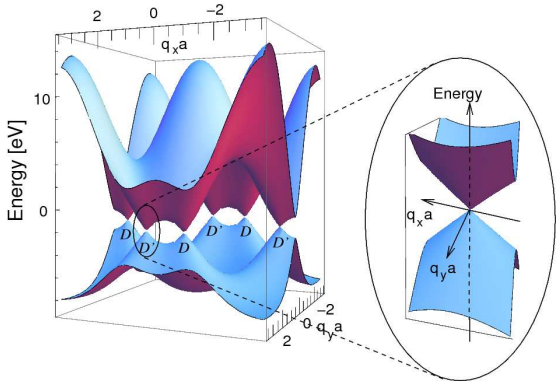


Figure 9 Band dispersion of the quinoid-type deformed the honeycomb lattice, for a lattice distortion of  $\delta a/a = -0.4$ , with  $t = 3$  eV,  $t_{nnn}/t = 0.1$ ,  $\partial t/\partial a = -5$  eV/Å, and  $\partial t_{nnn}/\partial a = -0.7$  eV/Å. The inset shows a zoom on one of the Dirac points,  $D'$ .

ial strain in the  $y$ -direction,<sup>5</sup>  $a \rightarrow a' = a + \delta a$ , in which case one obtains a quinoid-type deformation (Fig. 8). The hopping  $t'$  along  $\delta_3$  is then different from that  $t$  along  $\delta_1$  and  $\delta_2$  (Dietl *et al.*, 2008; Farjam and Rafii-Tabar, 2009; Goerbig *et al.*, 2008; Hasegawa *et al.*, 2006; Wunsch *et al.*, 2008; Zhu *et al.*, 2007),

$$t \rightarrow t' = t + \frac{\partial t}{\partial a} \delta a. \quad (55)$$

Furthermore, also four of six  $nnn$  hopping integrals are affected by the strain (see Fig. 8),

$$t_{nnn} \rightarrow t'_{nnn} = t_{nnn} + \frac{\partial t_{nnn}}{\partial a} \delta a. \quad (56)$$

If one considers a moderate deformation  $\epsilon \equiv \delta a/a \ll 1$ , the effect on the hopping amplitudes may be estimated with the help of Harrison's law (Harrison, 1981), according to which  $t = C\hbar^2/ma^2$ , where  $C$  is a numerical prefactor of order 1. One therefore finds a value

$$\frac{\partial t}{\partial a} = -\frac{2t}{a} \sim -4.3 \text{ eV/Å} \quad \text{and} \quad t' = t(1 - 2\epsilon) \quad (57)$$

which coincides well with the value  $\partial t/\partial a \simeq 5$  eV/Å, which may be found in the literature (Dillon *et al.*, 1977; Saito *et al.*, 1998). The estimation of the modified  $nnn$  hopping integral  $t'_{nnn}$  is slightly more involved. One may use a law  $t_{nnn}(b, a) \approx t(a) \exp[-(b-a)/d(a)]$  familiar in the context of the extended Hückel model (Salem, 1966), where  $b$  is the  $nnn$  distance, and  $d \approx a/3.5 \approx 0.4$  Å is a characteristic distance related to the overlap of atomic orbitals. In undeformed graphene one has  $b = a\sqrt{3}$ ,

whereas in quinoid-type graphene  $b' = b(1 + \epsilon/2)$ , which gives

$$t'_{nnn} = t_{nnn}(1 - 2\epsilon + b\epsilon/2d). \quad (58)$$

The electronic properties of quinoid-type graphene may then be described in terms of an effective Hamiltonian of the type (27),

$$\mathcal{H}_{\mathbf{k}} = t_{nnn} h_{\mathbf{k}} \mathbb{1} + t \begin{pmatrix} 0 & \tilde{\gamma}_{\mathbf{k}}^* \\ \tilde{\gamma}_{\mathbf{k}} & 0 \end{pmatrix}, \quad (59)$$

with (Goerbig *et al.*, 2008)

$$h_{\mathbf{k}} = 2 \cos \sqrt{3} k_x a + 2 \frac{t'_{nnn}}{t_{nnn}} \left\{ \cos \left[ \frac{\sqrt{3} k_x a}{2} + k_y a \left( \frac{3}{2} + \epsilon \right) \right] + \cos \left[ -\frac{\sqrt{3} k_x a}{2} + k_y a \left( \frac{3}{2} + \epsilon \right) \right] \right\}, \quad (60)$$

and the off-diagonal elements

$$\tilde{\gamma}_{\mathbf{k}} = 2e^{ik_y a(3/2+\epsilon)} \cos \left( \frac{\sqrt{3}}{2} k_x a \right) + (1 - 2\epsilon). \quad (61)$$

The resulting energy dispersion

$$\epsilon_{\mathbf{k}}^{\lambda} = t_{nnn} h_{\mathbf{k}} + \lambda t |\tilde{\gamma}_{\mathbf{k}}| \quad (62)$$

is plotted in Fig. 9 for an unphysically large deformation,  $\epsilon = 0.4$ , for illustration reasons. Notice that the reversible deformations are limited by a value of  $\epsilon \sim 0.1 \dots 0.2$  beyond which the graphene sheet cracks (Lee *et al.*, 2008). One notices, in Fig. 9, two effects of the deformation: i) the Dirac points no longer coincide with the corners of the first BZ, the form of which is naturally also modified by the deformation; and ii) the cones in the vicinity of the Dirac points are tilted, i.e. the  $nnn$  hopping term (60) breaks the electron-hole symmetry already at *linear* order in  $|\mathbf{q}|a$ . These two points are discussed in more detail in the following two subsections.

### 1. Dirac point motion

In order to evaluate quantitatively the position of the Dirac points, which are defined as the contact points between the valence ( $\lambda = -$ ) and the conduction ( $\lambda = +$ ) bands, one needs to solve the equation  $\tilde{\gamma}_{\mathbf{k}^D} = 0$ , in analogy with the case of undeformed graphene discussed in Sec. I.C.1. One then finds

$$k_y^D = 0 \quad \text{and} \quad k_x^D a = \xi \frac{2}{\sqrt{3}} \arccos \left( -\frac{t'}{2t} \right), \quad (63)$$

where the valley index  $\xi = \pm$  denotes again the two inequivalent Dirac points  $D$  and  $D'$ , respectively. As already mentioned, the Dirac points  $D$  and  $D'$  coincide, for undistorted graphene, with the crystallographic points  $K$  and  $K'$ , respectively, at the corners of the first BZ. The

<sup>5</sup> In our simplified model, we only consider one bond length changed by the strain. The more general case has been considered by Peirera *et al.* (Pereira *et al.*, 2009). However, the main effects are fully visible in the simplified model.

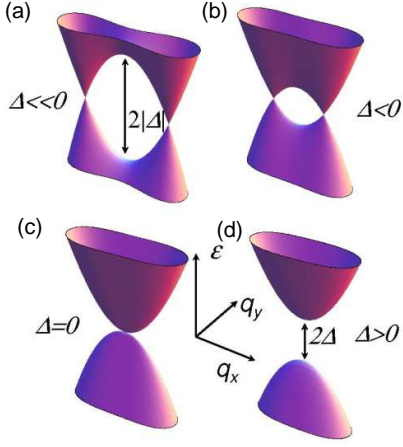


Figure 10 Topological semi-metal insulator transition in the model (64) driven by the gap parameter  $\Delta$ . (a) Two well-separated Dirac cones for  $\Delta \ll 0$ , as for graphene. (b) When lowering the modulus of the (negative) gap parameter, the Dirac points move towards a single point. (c) The two Dirac points merge into a single point at the transition ( $\Delta = 0$ ). The band dispersion remains linear in the  $q_y$ -direction while it becomes parabolic in the  $q_x$ -direction. (d) Beyond the transition ( $\Delta > 0$ ), the (parabolic) bands are separated by a band gap  $\Delta$  (insulating phase). From Montambaux *et al.*, 2009a.

distortion makes both pairs of points move in the same direction due to the negative value of  $\partial t/\partial a$ . However, unless the parameters are fine-tuned, this motion is different, and the two pairs of points no longer coincide.

One further notices that Eq. (63) has (two) solutions only for  $t' \leq 2t$ . Indeed, the two Dirac points merge at the characteristic point  $M''$  at the border of the first BZ (see Fig. 3). The point  $t' = 2t$  is special insofar as it characterizes a topological phase transition between a semi-metallic phase (for  $t' < 2t$ ) with a pair of Dirac cones and a band insulator (for  $t' > 2t$ ) (Dietl *et al.*, 2008; Esaki *et al.*, 2009; Montambaux *et al.*, 2009a,b; Pereira *et al.*, 2009; Wunsch *et al.*, 2008). In the vicinity of the transition, one may expand the Hamiltonian (59) around the merging point  $M''$  (Montambaux *et al.*, 2009a,b), and one finds<sup>6</sup>

$$\mathcal{H}_{\mathbf{q}}^M = \begin{pmatrix} 0 & \Delta + \frac{\hbar^2 q_x^2}{2m^*} - i\hbar c q_y \\ \Delta + \frac{\hbar^2 q_x^2}{2m^*} + i\hbar c q_y & 0 \end{pmatrix}, \quad (64)$$

in terms of the mass  $m^* = 2\hbar^2/3ta^2$  and the velocity  $c = 3ta/\hbar$  (Montambaux *et al.*, 2009b). The gap parameter  $\Delta = t' - 2t$  changes its sign at the transition – it is negative in the semi-metallic and positive in the insulating phase, where it describes a true gap (Fig. 10).

The Hamiltonian (64) has quite a particular form in the vicinity of the merging points: it is linear in the

<sup>6</sup> We do not consider the diagonal part of the Hamiltonian, here, i.e. we choose  $t_{nmn} = 0$ , because it does not affect the position of the Dirac points.

$q_y$ -direction, as one would expect for Dirac points, but it is quadratic in the  $q_x$ -direction (Dietl *et al.*, 2008). This is a general feature of merging points, which may only occur at the  $\Gamma$  point or else at half a reciprocal lattice vector  $\mathbf{G}/2$ , i.e. in the center of a BZ border line (such as the  $M$  points) (Montambaux *et al.*, 2009a). Indeed, one may show that in the case of a time-reversal symmetric Hamiltonian, the Fermi velocity in the  $x$ -direction then vanishes such that one must take into account the quadratic order in  $q_x$  in the energy band. Notice that such hybrid semi-Dirac points, with a linear-parabolic dispersion relation, are inaccessible in graphene because unphysically large strains would be required (Lee *et al.*, 2008; Pereira *et al.*, 2009). However, such points may exist in other physical systems such as cold atoms in optical lattices (Hou *et al.*, 2009; Lee *et al.*, 2009; Wunsch *et al.*, 2008; Zhao and Paramakanti, 2006; Zhu *et al.*, 2007), the quasi-2D organic material  $\alpha$ -(BEDT-TTF)<sub>2</sub>I<sub>3</sub> (Katayama *et al.*, 2006; Kobayashi *et al.*, 2007) or VO<sub>2</sub>/TiO<sub>2</sub> heterostructures (Banerjee *et al.*, 2009).

## 2. Tilted Dirac cones

Another aspect of quinoid-type deformed graphene and a consequence of the fact that the Dirac points no longer coincide with the BZ corners  $K$  and  $K'$  of high crystallographic symmetry is the tilt of the Dirac cones. This may be appreciated when expanding the Hamiltonian (59) to linear order around the Dirac points  $\xi\mathbf{k}_D$ , instead of an expansion around the point  $M''$  as in the last subsection. In contrast to the undeformed case (51), the diagonal components  $h_{\mathbf{k}}$  now yield a linear contribution (Goerbig *et al.*, 2008),  $t_{nmn}h_{\xi\mathbf{k}^D+\mathbf{q}}\mathbb{1} \simeq \xi\hbar\mathbf{w}_0 \cdot \mathbf{q}\mathbb{1}$ , in terms of the *tilt velocity*

$$w_{0x} = \frac{2\sqrt{3}}{\hbar}(t_{nmn}a \sin 2\theta + t'_{nmn}a \sin \theta) \quad \text{and} \quad w_{0y} = 0, \quad (65)$$

where we have defined  $\theta \equiv \arccos(-t'/2t)$ . The linear model is therefore described by the Hamiltonian,<sup>7</sup>

$$\mathcal{H}_{\mathbf{q}}^{\xi} = \xi\hbar(\mathbf{w}_0 \cdot \mathbf{q}\mathbb{1} + w_x q_x \sigma^x + w_y q_y \sigma^y), \quad (66)$$

with the renormalized anisotropic velocities

$$w_x = \frac{\sqrt{3}ta}{\hbar} \sin \theta \quad \text{and} \quad w_y = \frac{3t'a}{2\hbar} \left(1 + \frac{2}{3}\epsilon\right).$$

<sup>7</sup> This model may be viewed as the minimal form of the generalized Weyl Hamiltonian (with  $\sigma^0 \equiv \mathbb{1}$ )

$$H_W = \sum_{\mu=0,\dots,3} \hbar\mathbf{v}_{\mu} \cdot \mathbf{q}\sigma^{\mu},$$

which is the most general  $2 \times 2$  matrix Hamiltonian that yields a linear dispersion relation.

Diagonalizing the Hamiltonian (66) yields the dispersion relation

$$\epsilon_{\lambda}^{\xi}(\mathbf{q}) = \hbar \mathbf{w}_0 \cdot \mathbf{q} + \lambda \hbar \sqrt{w_x^2 q_x^2 + w_y^2 q_y^2}, \quad (67)$$

and one notices that the first term ( $\hbar \mathbf{w}_0 \cdot \mathbf{q}$ ) breaks indeed the symmetry  $\epsilon_{\lambda}^{\xi}(\mathbf{q}) = \epsilon_{\lambda}^{\xi}(-\mathbf{q})$  in each valley, i.e. it tilts the Dirac cones in the direction opposite to  $\mathbf{w}_0$ , as well as the electron-hole symmetry  $\epsilon_{\lambda}(\mathbf{q}) = -\epsilon_{-\lambda}(\mathbf{q})$  at the same wave vector.<sup>8</sup> Indeed, the linearity in  $\mathbf{q}$  of the generalized Weyl Hamiltonian (66) satisfies only the symmetry  $\mathcal{H}_{\mathbf{q}}^{\xi} = -\mathcal{H}_{-\mathbf{q}}^{\xi}$  inside each valley.

Furthermore, one notices that the chiral symmetry is preserved even in the presence of the tilt term if one redefines the chirality operator (45) as  $\eta_{\mathbf{q}} = (w_x q_x \sigma^x + w_y q_y \sigma^y) / \sqrt{w_x^2 q_x^2 + w_y^2 q_y^2}$ , which naturally commutes with the Hamiltonian (66). The eigenstates of the chirality operator are still given by

$$\psi_{\eta} = \frac{1}{\sqrt{2}} \begin{pmatrix} 1 \\ \eta e^{-i\varphi_{\mathbf{q}}} \end{pmatrix}, \quad (68)$$

with  $\tan \varphi_{\mathbf{k}} \equiv w_y q_y / w_x q_x$ , and one notices that these states are also the natural eigenstates of the Hamiltonian (66).

One finally notices that not all values of the tilt parameter  $\mathbf{w}_0$  are indeed physical. In order to be able to associate  $\lambda = +$  to a positive and  $\lambda = -$  to a negative energy state, one must fulfill the condition

$$\tilde{w}_0 < 1, \quad (69)$$

in terms of the *tilt parameter*

$$\tilde{w}_0 \equiv \sqrt{\left(\frac{w_{0x}}{w_x}\right)^2 + \left(\frac{w_{0y}}{w_y}\right)^2}. \quad (70)$$

In the particular case of the deformation in the  $y$ -axis, which is discussed here and in which case  $w_{0y} = 0$  [see Eq. (65)], the general form of the tilt parameter reduces to  $\tilde{w}_0 = w_{0x}/w_x$ . Unless this condition is fulfilled, the iso-energetic lines are no longer ellipses but hyperbolas. In quinoid-type deformed graphene, the tilt parameter may be evaluated as (Goerbig *et al.*, 2008)

$$\tilde{w}_0 = 2 \left( \frac{t_{nnn} \sin 2\theta}{t \sin \theta} + \frac{t'_{nnn}}{t} \right) \simeq \frac{2}{t^2} (t t'_{nnn} - t' t_{nnn}) \simeq 0.6\epsilon, \quad (71)$$

where we have used Eqs. (57) and (58). Even at moderate deformations ( $\epsilon < 0.1$ ), the tilt of the Dirac cones is on the order of 5%, and one may therefore hope to

observe the effect, e.g. in angle-resolved photoemission spectroscopy (ARPES) measurements (Damascelli, 2004) that have been successfully applied to epitaxial graphene (Bostwick *et al.*, 2007) and graphitic samples (Zhou *et al.*, 2006). Notice that the Dirac cones are naturally tilted in  $\alpha$ -(BEDT-TTF)<sub>2</sub>I<sub>3</sub> (Katayama *et al.*, 2006; Kobayashi *et al.*, 2007), where the Dirac points occur at positions of low crystallographic symmetry within the first BZ.

## II. DIRAC EQUATION IN A MAGNETIC FIELD AND THE RELATIVISTIC QUANTUM HALL EFFECT

As already mentioned in the introduction, a key experiment in graphene research was the discovery of a particular quantum Hall effect (Novoselov *et al.*, 2005a; Zhang *et al.*, 2005), which unveiled the relativistic nature of low-energy electrons in graphene. For a deeper understanding of this effect and as a basis for the following parts, we discuss here relativistic massless 2D fermions in a strong quantizing magnetic field (Sec. II.A). The limits of the Dirac equation in the treatment of the high-field properties of graphene are discussed in Sec. II.B, and we terminate this section with a discussion of the relativistic Landau level spectrum in the presence of an in-plane electric field (Sec. II.C) and that of deformed graphene (Sec. II.D).

### A. Massless 2D Fermions in a Strong Magnetic Field

In order to describe free electrons in a magnetic field, one needs to replace the canonical momentum  $\mathbf{p}$  by the gauge-invariant kinetic momentum (Jackson, 1999)

$$\mathbf{p} \rightarrow \mathbf{\Pi} = \mathbf{p} + e\mathbf{A}(\mathbf{r}), \quad (72)$$

where  $\mathbf{A}(\mathbf{r})$  is the vector potential that generates the magnetic field  $\mathbf{B} = \nabla \times \mathbf{A}(\mathbf{r})$ . The kinetic momentum is proportional to the electron velocity  $\mathbf{v}$ , which must naturally be gauge-invariant because it is a physical quantity.

In the case of electrons on a lattice, the substitution (72), which is then called *Peierls substitution*, remains correct as long as the lattice spacing  $\tilde{a}$  is much smaller than the *magnetic length*

$$l_B = \sqrt{\frac{\hbar}{eB}}, \quad (73)$$

which is the fundamental length scale in the presence of a magnetic field. Because  $\tilde{a} = 0.24$  nm and  $l_B \simeq 26$  nm/ $\sqrt{B[\text{T}]}$ , this condition is fulfilled in graphene for the magnetic fields, which may be achieved in today's high-field laboratories ( $\sim 45$  T in the continuous regime and  $\sim 80$  T in the pulsed regime).

With the help of the (Peierls) substitution (72), one may thus immediately write down the Hamiltonian for

<sup>8</sup> In the absence of the tilt term  $\hbar \mathbf{w}_0 \cdot \mathbf{q} \mathbb{1}$ , this is a consequence of the symmetry  $\sigma^z \mathcal{H} \sigma^z = -\mathcal{H}$ , which is satisfied both by the effective Hamiltonian (27) for  $t_{nnn} = 0$  and the linearised version (40) in each valley for undeformed graphene.

charged particles in a magnetic field if one knows the Hamiltonian in the absence of the field,

$$\mathcal{H}(\mathbf{p}) \rightarrow H(\mathbf{\Pi}) = \mathcal{H}(\mathbf{p} + e\mathbf{A}) = H^B(\mathbf{p}, \mathbf{r}). \quad (74)$$

Notice that because of the spatial dependence of the vector potential, the resulting Hamiltonian is no longer translation invariant, and the (canonical) momentum  $\mathbf{p} = \hbar\mathbf{q}$  is no longer a conserved quantity. For the Dirac Hamiltonian (40), which we have derived in the preceding section to lowest order in  $|\mathbf{q}|a$ , the Peierls substitution yields

$$\mathcal{H}_B^\xi = \xi \hbar v_F (q_x \sigma^x + q_y \sigma^y) \rightarrow \mathcal{H}_B^{\text{eff}, \xi} = \xi v_F (\Pi_x \sigma^x + \Pi_y \sigma^y). \quad (75)$$

We further notice that, because electrons do not only possess a charge but also a spin, each energy level resulting from the diagonalization of the Hamiltonian (75) is split into two spin branches separated by the Zeeman effect  $\Delta_Z = g\mu_B B$ , where  $g$  is the  $g$ -factor of the host material [ $g \sim 2$  for graphene (Zhang *et al.*, 2006)] and  $\mu_B = e\hbar/2m_0$  is the Bohr magneton, in terms of the bare electron mass  $m_0$ . In the remainder of this section, we concentrate on the orbital degrees of freedom which yield the characteristic level structure of electrons in a magnetic field and therefore neglect the spin degree of freedom, i.e. we consider *spinless* fermions. Effects related to the internal degrees of freedom are discussed in a separate section (Sec. V) in the framework of the quantum-Hall ferromagnet.

### 1. Quantum-mechanical treatment

One may easily treat the Hamiltonian (75) quantum-mechanically with the help of the standard *canonical quantization* (Cohen-Tannoudji *et al.*, 1973), according to which the components of the position  $\mathbf{r} = (x, y)$  and the associated canonical momentum  $\mathbf{p} = (p_x, p_y)$  satisfy the commutation relations  $[x, p_x] = [y, p_y] = i\hbar$  and  $[x, y] = [p_x, p_y] = [x, p_y] = [y, p_x] = 0$ . As a consequence of these relations, the components of the kinetic momentum no longer commute, and, with the help of the commutator relation (Cohen-Tannoudji *et al.*, 1973)

$$[\mathcal{O}_1, f(\mathcal{O}_2)] = \frac{df}{d\mathcal{O}_2} [\mathcal{O}_1, \mathcal{O}_2] \quad (76)$$

between two arbitrary operators, the commutator of which is an operator that commutes itself with both  $\mathcal{O}_1$  and  $\mathcal{O}_2$ , one finds

$$[\Pi_x, \Pi_y] = -ie\hbar \left( \frac{\partial A_y}{\partial x} - \frac{\partial A_x}{\partial y} \right) = -i \frac{\hbar^2}{l_B^2}, \quad (77)$$

in terms of the magnetic length (73).

For the quantum-mechanical solution of the Hamiltonian (75), it is convenient to use the pair of conjugate operators  $\Pi_x$  and  $\Pi_y$  to introduce *ladder operators* in the same manner as in the quantum-mechanical treatment

of the one-dimensional harmonic oscillator. These ladder operators play the role of a *complex* gauge-invariant momentum (or velocity), and they read

$$\hat{a} = \frac{l_B}{\sqrt{2}\hbar} (\Pi_x - i\Pi_y) \quad \text{and} \quad \hat{a}^\dagger = \frac{l_B}{\sqrt{2}\hbar} (\Pi_x + i\Pi_y), \quad (78)$$

where we have chosen the appropriate normalization such as to obtain the usual commutation relation

$$[\hat{a}, \hat{a}^\dagger] = 1. \quad (79)$$

It turns out to be helpful for practical calculations to invert the expression for the ladder operators (78),

$$\Pi_x = \frac{\hbar}{\sqrt{2}l_B} (\hat{a}^\dagger + \hat{a}) \quad \text{and} \quad \Pi_y = \frac{\hbar}{i\sqrt{2}l_B} (\hat{a}^\dagger - \hat{a}). \quad (80)$$

### 2. Relativistic Landau levels

In terms of the ladder operators (78), the Hamiltonian (75) becomes

$$H_B^\xi = \xi \sqrt{2} \frac{\hbar v_F}{l_B} \begin{pmatrix} 0 & \hat{a} \\ \hat{a}^\dagger & 0 \end{pmatrix}. \quad (81)$$

One remarks the occurrence of a characteristic frequency  $\omega' = \sqrt{2}v_F/l_B$ , which plays the role of the cyclotron frequency in the relativistic case. Notice, however, that this frequency may not be written in the form  $eB/m_b$  because the band mass is strictly zero in graphene, such that the frequency would diverge.<sup>9</sup>

The eigenvalues and the eigenstates of the Hamiltonian (81) are readily obtained by solving the eigenvalue equation  $H_B^\xi \psi_n = \epsilon_n \psi_n$ , in terms of the 2-spinors,

$$\psi_n = \begin{pmatrix} u_n \\ v_n \end{pmatrix}. \quad (82)$$

We thus need to solve the system of equations

$$\xi \hbar \omega' \hat{a} v_n = \epsilon_n u_n \quad \text{and} \quad \xi \hbar \omega' \hat{a}^\dagger u_n = \epsilon_n v_n, \quad (83)$$

which yields the equation

$$\hat{a}^\dagger \hat{a} v_n = \left( \frac{\epsilon_n}{\hbar \omega'} \right)^2 v_n \quad (84)$$

for the second spinor component. One may therefore identify, up to a numerical factor, the second spinor component  $v_n$  with the eigenstate  $|n\rangle$  of the usual number operator  $\hat{a}^\dagger \hat{a}$ , with  $\hat{a}^\dagger \hat{a} |n\rangle = n |n\rangle$  in terms of the integer  $n \geq 0$ . Furthermore, one observes that the square of the energy is proportional to this quantum number,

<sup>9</sup> Sometimes, a density-dependent *cyclotron mass*  $m_C$  is formally introduced via the equality  $\omega' \equiv eB/m_C$ .

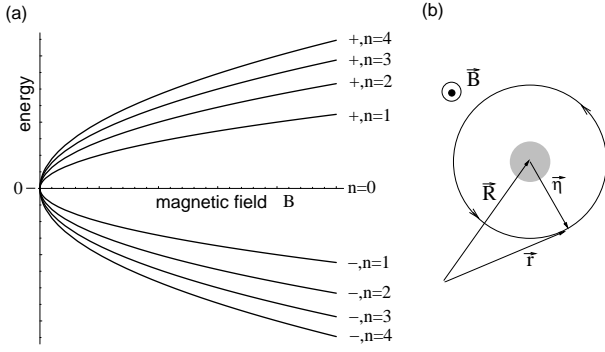


Figure 11 (a) Relativistic Landau levels as a function of the magnetic field. (b) Semi-classical picture of cyclotron motion described by the cyclotron coordinate  $\boldsymbol{\eta}$ , where the charged particle turns around the guiding center  $\mathbf{R}$ . The gray region depicts the uncertainty on the guiding center, as indicated by Eq. (98).

$\epsilon_n^2 = (\hbar\omega')^2 n$ . This equation has two solutions, a positive and a negative one, and one needs to introduce another quantum number  $\lambda = \pm$ , which labels the states of positive and negative energy, respectively. This quantum number plays the same role as the band index ( $\lambda = +$  for the conduction and  $\lambda = -$  for the valence band) in the zero- $B$ -field case discussed in the preceding section. One thus obtains the spectrum (McClure, 1956)

$$\epsilon_{\lambda,n} = \lambda \frac{\hbar v_F}{l_B} \sqrt{2n} \quad (85)$$

of *relativistic Landau levels* (LLs) that disperse as  $\lambda\sqrt{Bn}$  as a function of the magnetic field [see Fig. 11(a)]. Notice that, as in the  $B = 0$  case, the level spectrum is two-fold valley-degenerate.

Once we know the second spinor component, the first component is obtained from Eq. (83), which reads  $u_n \propto \hat{a} v_n \sim \hat{a}|n\rangle \sim |n-1\rangle$  because of the usual equations

$$\hat{a}^\dagger |n\rangle = \sqrt{n+1} |n+1\rangle \quad \text{and} \quad \hat{a}|n\rangle = \sqrt{n} |n-1\rangle \quad (86)$$

for the ladder operators, where the last equation is valid for  $n > 0$ . One then needs to distinguish the zero-energy LL ( $n = 0$ ) from all other levels. Indeed, for  $n = 0$ , the first component is zero because

$$\hat{a}|n=0\rangle = 0 \quad (87)$$

In this case one obtains the spinor

$$\psi_{n=0} = \begin{pmatrix} 0 \\ |n=0\rangle \end{pmatrix}. \quad (88)$$

In all other cases ( $n \neq 0$ ), one has positive and negative energy solutions, which differ among each other by a relative sign in one of the components. A convenient representation of the associated spinors is given by

$$\psi_{\lambda,n \neq 0}^\xi = \frac{1}{\sqrt{2}} \begin{pmatrix} |n-1\rangle \\ \xi \lambda |n\rangle \end{pmatrix}. \quad (89)$$

The particular form of the  $n = 0$  spinor (88) associated with zero-energy states merits a more detailed comment. One notices that only the second spinor component is non-zero. Remember that this component corresponds to the B sublattice in the  $K$ -valley ( $\xi = +$ ) and to the A sublattice in the  $K'$ -valley ( $\xi = -$ ) – the valley pseudospin therefore coincides with the sublattice pseudospin, and the two sublattices are decoupled at zero energy. Notice that this is also the case in the absence of a magnetic field, where the relation (50) between the chirality, the band index and the valley pseudospin is only valid at non-zero values of the wave vector, i.e. not exactly at zero energy. Indeed, the chirality can no longer be defined as the projection of the sublattice pseudospin on the direction of propagation  $\mathbf{q}/|\mathbf{q}|$ , which is singular at  $\mathbf{q} = 0$ . At zero energy, it is therefore useful to identify the chirality with the valley pseudospin. Notice, however, that this particularity concerns, in the absence of a magnetic field, only a non-extensive number of states (only two) because of the vanishing density of states at zero energy, whereas the zero-energy LL  $n = 0$  is macroscopically degenerate, as discussed in the following paragraphs.

*a. LL degeneracy.* A particular feature of LLs, both relativistic and non-relativistic ones, consists of their large degeneracy, which equals the number of flux quanta  $N_B = \mathcal{A} \times B / (h/e)$  threading the 2D surface  $\mathcal{A}$  occupied by the electron gas. From the classical point of view, this degeneracy is related to the existence of a constant of motion, namely the position of the *guiding center*, i.e. the center of the classical cyclotron motion. Indeed, due to translation invariance in a uniform magnetic field, the energy of an electron does not depend on the position of this guiding center. Translated to quantum mechanics, this means that the operator corresponding to this guiding center  $\mathbf{R} = (X, Y)$  commutes with the Hamiltonian  $\mathcal{H}(\mathbf{p} + e\mathbf{A})$ .

In order to understand how the LL degeneracy is related to the guiding-center operator, we formally decompose the position operator

$$\mathbf{r} = \mathbf{R} + \boldsymbol{\eta} \quad (90)$$

into its guiding center  $\mathbf{R}$  and the cyclotron variable  $\boldsymbol{\eta} = (\eta_x, \eta_y)$ , as depicted in Fig. 11(b). Whereas the guiding center is a constant of motion, as mentioned above, the cyclotron variable describes the dynamics of the electron in a magnetic field and is, classically, the time-dependent component of the position. Indeed, the cyclotron variable is perpendicular to the electron's velocity and thus related to the kinetic momentum  $\boldsymbol{\Pi}$  by

$$\eta_x = \frac{\Pi_y}{eB} \quad \text{and} \quad \eta_y = -\frac{\Pi_x}{eB}, \quad (91)$$

which, as a consequence of the commutation relations (77), satisfy

$$[\eta_x, \eta_y] = \frac{[\Pi_x, \Pi_y]}{(eB)^2} = -il_B^2, \quad (92)$$

whereas they commute naturally with the guiding-center components  $X$  and  $Y$ . Equation (92) thus induces the commutation relation

$$[X, Y] = -[\eta_x, \eta_y] = il_B^2, \quad (93)$$

in order to satisfy  $[x, y] = 0$ .

These commutation relations indicate that the components of the guiding-center operator form a pair of conjugate variables, and one may introduce, in the same manner as for the kinetic momentum operator  $\mathbf{\Pi}$ , the ladder operators

$$\hat{b} = \frac{1}{\sqrt{2}l_B}(X + iY) \quad \text{and} \quad \hat{b}^\dagger = \frac{1}{\sqrt{2}l_B}(X - iY), \quad (94)$$

which again satisfy the usual commutation relations  $[\hat{b}, \hat{b}^\dagger] = 1$  and which naturally commute with the Hamiltonian. One may then introduce a number operator  $\hat{b}^\dagger \hat{b}$  associated with these ladder operators, the eigenstates of which satisfy the eigenvalue equation

$$\hat{b}^\dagger \hat{b} |m\rangle = m |m\rangle. \quad (95)$$

One thus obtains a second quantum number, an integer  $m \geq 0$ , which is necessary to describe the full quantum states in addition to the LL quantum number  $n$ , and the completed quantum states (88) and (89) then read

$$\psi_{n=0,m}^\xi = \psi_{n=0}^\xi \otimes |m\rangle = \begin{pmatrix} 0 \\ |n=0, m\rangle \end{pmatrix} \quad (96)$$

and

$$\psi_{\lambda n,m}^\xi = \psi_{\lambda n}^\xi \otimes |m\rangle = \frac{1}{\sqrt{2}} \begin{pmatrix} |n-1, m\rangle \\ \xi \lambda |n, m\rangle \end{pmatrix}, \quad (97)$$

respectively.

One may furthermore use the commutation relation (93) for counting the number of states, i.e. the degeneracy, in each LL. Indeed, this relation indicates that one may not measure both components of the guiding center simultaneously, which is therefore smeared out over a surface

$$\Delta X \Delta Y = 2\pi l_B^2, \quad (98)$$

as it is depicted in Fig. 11(b). The result (98) for the surface occupied by a quantum state may be calculated rather simply if one chooses a particular gauge, such as the Landau or the symmetric gauge for the vector potential, but its general derivation is rather involved (Imry, 1997). This minimal surface plays the same role as the surface (action)  $h$  in phase space and therefore allows us to count the number of possible quantum states of a given (macroscopic) surface  $\mathcal{A}$ ,

$$N_B = \frac{\mathcal{A}}{\Delta X \Delta Y} = \frac{\mathcal{A}}{2\pi l_B^2} = n_B \times \mathcal{A}, \quad (99)$$

where we have introduced the flux density

$$n_B = \frac{1}{2\pi l_B^2} = \frac{B}{h/e}, \quad (100)$$

which is nothing other than the magnetic field measured in units of the flux quantum  $h/e$ , as already mentioned above. The ratio between the electronic density  $n_{el}$  and this flux density then defines the *filling factor*

$$\nu = \frac{n_{el}}{n_B} = \frac{hn_{el}}{eB}, \quad (101)$$

which characterizes the filling of the different LLs.

*b. The relativistic quantum Hall effect.* The integer quantum Hall effect (IQHE) in 2D electron systems (v. Klitzing *et al.*, 1980) is a manifestation of the LL quantization and the macroscopic degeneracy (100) of each level, as well as of semi-classical electron localization due to the sample impurities.<sup>10</sup> In a nutshell, this energy quantization yields a quantization of the Hall resistance

$$R_H = \frac{h}{e^2 N}, \quad (102)$$

where  $N = [\nu]$  is the integer part of the filling factor (101), while the longitudinal resistance vanishes.<sup>11</sup> The resistance quantization reflects the presence of an incompressible quantum liquid with gapped single-particle and density excitations. In the case of the IQHE, at integer filling factors, the gap is simply given by the energy difference between adjacent LLs which must be overcome by an electron that one adds to the system. Notice that if one takes into account the electron spin and a vanishing Zeeman effect, the condition for the occurrence of the IQHE is satisfied when both spin branches of the last LL  $n$  are completely filled, and one thus obtains the Hall-resistance quantization at the filling factors

$$\nu^{IQHE} = 2n, \quad (103)$$

i.e. for even integers. Odd integers may principally be observed at higher magnetic fields when the Zeeman effect becomes prominent, and the energy gap is then no longer given by the inter-LL spacing but by the Zeeman gap. This picture is naturally simplistic and needs to be modified if one takes into account electronic interactions

<sup>10</sup> Strictly speaking, the IQHE requires only the breaking of translation invariance, which in a diffusive sample is due to impurities. In a ballistic sample, translation invariance is broken via the sample edges (Büttiker, 1992).

<sup>11</sup> A simultaneous measurement of the Hall and the longitudinal resistance requires a particular geometry with at least four electric contacts [for a recent review on the quantum Hall effect, see Ref. (Goerbig, 2009)].



– their consequences, such as the fractional quantum Hall effect or ferromagnetic states are discussed, in the context of graphene, in Sec. V.

The phenomenology of the relativistic quantum Hall effect (RQHE) in graphene is quite similar to that of the IQHE. Notice, however, that one is confronted not only with the two-fold spin degeneracy of electrons in graphene (in the absence of a strong Zeeman effect), but also with the two-fold valley degeneracy due to the presence of the  $K$  and  $K'$  points in the first BZ, which govern the low-energy electronic properties. The filling factor therefore changes by steps of 4 between adjacent plateaus in the Hall resistance. Furthermore, the filling factor (101) is defined in terms of the carrier density which vanishes at the Dirac point. This particle-hole symmetric situation naturally corresponds to a half-filled zero-energy LL  $n = 0$ , whereas all levels with  $\lambda = -$  are completely filled and all  $\lambda = +$  levels are unoccupied. In the absence of a Zeeman effect and electronic interactions, there is thus no quantum Hall effect at  $\nu = 0$ , and the condition of a completely filled (or empty)  $n = 0$  LL is found for  $\nu = 2$  ( $\nu = -2$ ). As a consequence, the signature of the RQHE is a Hall-resistance quantization at the filling factors (Gusynin and Sharapov, 2005, 2006; Peres *et al.*, 2006)

$$\nu^{RQHE} = 2(2n + 1), \quad (104)$$

which needs to be contrasted to the series (103) of the IQHE in non-relativistic 2D electron systems. The series (104) has indeed been observed in 2005 within the quantum Hall measurements (Novoselov *et al.*, 2005a; Zhang *et al.*, 2005), which thus revealed the relativistic character of electrons in exfoliated graphene. More recently, the RQHE has been observed also in epitaxial graphene with moderate mobilities (Jobst *et al.*, 2010; Shen *et al.*, 2009; Wu *et al.*, 2009).

*c. Experimental observation of relativistic Landau levels.* The  $\sqrt{Bn}$  dispersion of relativistic LLs has been observed experimentally in transmission spectroscopy, where one shines monochromatic light on the sample and measures the intensity of the transmitted light. Such experiments have been performed both on epitaxial (Sadowski *et al.*, 2006) and exfoliated graphene (Jiang *et al.*, 2007a).

When the monochromatic light is in resonance with a dipole-allowed transition from the (partially) filled ( $\lambda, n$ ) to the (partially) unoccupied LL ( $\lambda', n \pm 1$ ), it is absorbed due to an electronic excitation between the two levels. Notice that, in a non-relativistic 2D electron gas, the only allowed dipolar transition is that from the last occupied LL  $n$  to the first unoccupied one  $n + 1$ . The transition energy is  $\hbar\omega_C$ , independently of  $n$ , and one therefore observes a single absorption line (cyclotron resonance) that is robust to electron-electron interactions, as a consequence of Kohn's theorem (Kohn, 1961).

In graphene, however, there are many more allowed transitions due to the presence of two electronic bands,

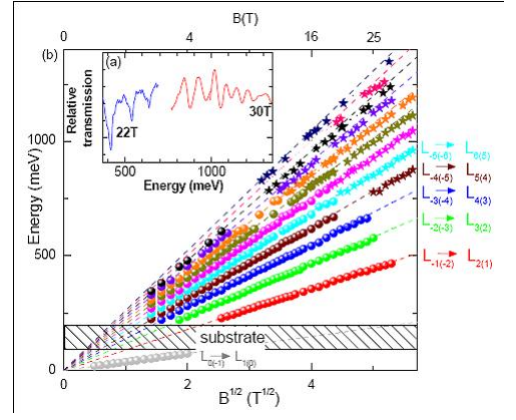


Figure 12 Transmission spectroscopy on epitaxial multilayer graphene (Plochocka *et al.*, 2008). The inset shows a representative transmission spectrum. The main figure represents the positions of the absorption lines as a function of the square-root of the magnetic field. The dashed lines correspond to transitions calculated at linear order, in agreement with the Dirac equation, whereas one notices downward deviations in the high-energy limit.

the conduction and the valence band, and the transitions have the energies

$$\Delta_{n,\lambda} = \frac{\hbar v_F}{l_B} \left[ \sqrt{2(n+1)} - \xi\sqrt{2n} \right], \quad (105)$$

where  $\lambda = +$  denotes an intraband and  $\lambda = -$  an interband transition (Abergel and Fal'ko, 2007; Iyengar *et al.*, 2007; Sadowski *et al.*, 2006). One therefore obtains families of resonances the energy of which disperses as  $\Delta_{n,\lambda} \propto \sqrt{B}$ , as it has been observed in the experiments [see Fig. 12, where we show the results from Ref. (Plochocka *et al.*, 2008)]. Notice that the dashed lines in Fig. 12 are fits with a single fitting parameter (the Fermi velocity  $v_F$ ), which matches well all experimental points for different values of  $n$  in the low-energy regime.

Moreover, the relativistic LLs have later been directly observed in scanning-tunneling spectroscopy in graphene on a graphite substrate<sup>12</sup> (Li *et al.*, 2009a) as well as on epitaxial graphene (Song *et al.*, 2010).

## B. Limits of the Dirac Equation in the Description of Graphene Landau Levels

Transmission spectroscopy is an ideal tool for the study of the high-energy part of the LL spectrum when considering the transitions ( $\lambda = -, n$ )  $\rightarrow$  ( $\lambda = +, n \pm 1$ ), for  $n \gg 1$ . As discussed in Sec. I.C.2, one expects deviations [of order  $\mathcal{O}(|\mathbf{q}|^2 a^2)$ ] from the linear dispersion in this limit. These deviations renormalize the energy of the LLs and thus the transition energies.

<sup>12</sup> With the help of the same technique, relativistic LLs had before been identified even in graphite (Li and Andrei, 2007).

In order to quantify the effect (Plochocka *et al.*, 2008), we may use the Peierls substitution (72) and the expressions (80) in the terms (51) and (52) corresponding to the higher-order diagonal and off-diagonal band terms, respectively. This yields the Hamiltonian

$$H_B^\xi = \begin{pmatrix} h' & h_\xi^* \\ h_\xi & h' \end{pmatrix}, \quad (106)$$

where the diagonal elements read

$$h' = \hbar\omega' \frac{3t_{nnn}a}{\sqrt{2}tl_B} \hat{a}^\dagger \hat{a}, \quad (107)$$

and the off-diagonal ones are

$$h_\xi = \xi \hbar\omega' \left( \hat{a}^\dagger - \xi \frac{aw_1}{2\sqrt{2}l_B} \hat{a}^2 - \frac{a^2w_2^2}{4l_B^2} \hat{a}^\dagger \hat{a} \right). \quad (108)$$

Naturally, to lowest order in  $a/l_B$ , one obtains again the Hamiltonian (81). The dimensionless parameters  $w_1$  and  $w_2$  are artificially added to the expressions and play the role of fitting parameters in the comparison with experimental measurements, as will be discussed below. They measure the deviation from the tight-binding-model expectation,  $w_1 = w_2 = 1$ . Notice furthermore that, since we are interested in the  $n \gg 1$  limit, we do not care about corrections related to the ordering of the ladder operators, such that we identify  $a^{\dagger 2}a^2 \simeq a^2a^{\dagger 2} \simeq (a^\dagger a)^2$  in the following parts.

In the calculation of the LL spectrum, one may proceed in the same manner as in Sec. II.A.2 – the eigenvalue equation (84) for the second spinor component now becomes

$$h_\xi h_\xi^\dagger v_n \simeq (\epsilon_n - h')^2 v_n, \quad (109)$$

which is asymptotically correct in the large- $n$  limit, where we may neglect the commutator  $[h_\xi, h']$  on the right-hand side of the equation.<sup>13</sup> The combination  $\hat{H}_\xi \equiv h_\xi h_\xi^\dagger$  is now interpreted as some *fake* Hamiltonian which needs to be diagonalized in order to obtain the modified LLs. Notice that  $n$  remains a good quantum number if one considers  $h'$  on the right-hand side of the eigenvalue equation. The left-hand side consists of a term

$$\hat{H}_0 \simeq (\hbar\omega')^2 \left[ \hat{a}^\dagger \hat{a} - \frac{4w_2^2 - w_1^2}{8} \left( \frac{a}{l_B} \right)^2 (\hat{a}^\dagger \hat{a})^2 \right] \quad (110)$$

that contains powers of  $\hat{a}^\dagger \hat{a}$  and thus respects the quantum number  $n$ , but in addition it contains the trigonal-warping term

$$\hat{H}_{t.w.} = -\xi \frac{w_1 (\hbar\omega')^2 a}{2\sqrt{2}l_B} (\hat{a}^{\dagger 3} + \hat{a}^3), \quad (111)$$

which does not commute with  $\hat{a}^\dagger \hat{a}$  and which needs to be treated apart. If we neglect this trigonal-warping term for a moment, the LL energies are obtained from the quadratic equation

$$(\hbar\omega')^2 \left[ n - \frac{4w_2^2 - w_1^2}{8} \frac{a^2}{l_B^2} n^2 \right] \simeq \left( \epsilon_n - \hbar\omega' \frac{3t_{nnn}a}{\sqrt{2}tl_B} n \right)^2. \quad (112)$$

In order to account for the trigonal-warping term in the eigenvalue equation (109), we may use a perturbative treatment, which is justified because of the small parameter  $a/l_B$ . There is no contribution at first order since  $\langle n | \hat{a}^{\dagger 3} | n \rangle = 0$  due to the orthogonality of the eigenstates  $\langle n | n' \rangle = \delta_{n,n'}$ . At second order, one obtains

$$\delta_n = -\frac{(\hbar\omega')^2}{8} \left( \frac{a}{l_B} \right)^2 \times 3n [1 + \mathcal{O}(1/n)], \quad (113)$$

which needs to be added to the right-hand side in Eq. (112). Interestingly, trigonal warping thus yields the same correction to the energies of the relativistic LLs as the third-order term in the expansion of the band dispersion, although trigonal warping occurs at second order in the absence of a magnetic field, as we have discussed in Sec. I.C.2. This effect is due to the anisotropy of the band correction; in the presence of a magnetic field, the  $\cos(3\varphi_{\mathbf{q}})$  term in Eq. (54) is averaged over the angle  $\varphi_{\mathbf{q}}$ , and therefore only contributes at second order in the perturbation theory described above. This eventually yields a correction of order  $(a/l_B)^2$  to the LL energy, as does the third-order term in the correction of the band dispersion.

One finally obtains, in the large- $n$  limit, where these corrections become relevant, the energies of the relativistic LLs (Plochocka *et al.*, 2008)

$$\epsilon_{\lambda n} = \hbar \frac{v_F}{l_B} \frac{3t_{nnn}}{t} \frac{a}{l_B} n + \lambda \hbar \frac{v_F}{l_B} \sqrt{2n} \left\{ 1 - \frac{3w^2}{8} \left( \frac{a}{l_B} \right)^2 n [1 + \mathcal{O}(1/n)] \right\}, \quad (114)$$

independent of the valley index  $\xi$ , where  $\mathcal{O}(1/n)$  stands for corrections of order  $1/n$ . Notice that the fitting parameters  $w_1$  and  $w_2$  cannot be determined independently from a fit to the spectroscopic measurement, but only the combination  $w^2 \equiv (w_1^2 + 2w_2^2)/3$ . Equation (114) generalizes a calculation for the relativistic LLs when only  $nmn$  hopping is taken into account (Peres *et al.*, 2006).

In Fig. (12), we show experimental results obtained from high-field transmission spectroscopy on multi-layer epitaxial graphene (Plochocka *et al.*, 2008). Qualitatively, one notices a downward renormalization of the transition energies

$$\Delta_n = \epsilon_{\lambda=+,n} - \epsilon_{\lambda=-,n} \quad (115)$$

in the interband regime for large values of  $n$ , in agreement with Eq. 114. Notice that because transmission spectroscopy is sensitive to energy-level differences, the

<sup>13</sup> The commutator would yield relative corrections that are on the order of  $1/n$  and  $a/l_B$  as compared to the energy scale  $(t_{nnn}/t)(a/l_B)n$  that dominates  $h'$ .

$nnn$  correction in Eq. (114) yields only a correction on the order of  $(t_{nnn}/t)(a/l_B)/n \lesssim 1\%/n$  at  $B \sim 25$  T as compared to the energy scale  $t(a/l_B)n$  of the transition, whereas the other term yields a correction on the order of  $(a/l_B)^2 \times n \sim 0.5\% \times n$ . The latter corrections thus become more relevant in the large- $n$  limit than the  $nnn$  correction. Indeed, the experiment (Plochocka *et al.*, 2008) was not capable of probing the electron-hole symmetry breaking associated with the  $nnn$  term, whereas a quantitative study of the high-energy transitions revealed a good semi-quantitative agreement with the calculated LL spectrum (114). However, it has been shown that the simple-minded tight-binding approach (with  $w = 1$ ) underestimates the higher-order band corrections and that the best fit to Eq. (114) is obtained for a value of  $w = 2.8$ . The origin of this discrepancy is yet unexplained, and it may be interesting to perform high-field transmission spectroscopy measurement also on single-layer exfoliated graphene in order to understand whether the stronger downward renormalization of the LLs is due to interlayer couplings in the epitaxial multi-layer sample.

### C. Landau Level Spectrum in the Presence of an Inplane Electric Field

A remarkable consequence of the relativistic character of electrons in graphene and the Lorentz invariance of the Dirac equation is their behavior in crossed magnetic and electric fields, where the magnetic field remains perpendicular to the graphene sheet and the electric field is applied in the plane. Remember that in a non-relativistic 2D electron systems, the electric field  $\mathbf{E} = E\mathbf{e}_y$  (in the  $y$ -direction) simply lifts the LL degeneracy and adds a term  $\hbar(E/B)k$  to the LL energies, where  $k$  is the wave vector in the  $x$ -direction. At a fixed wave vector  $k$ , the LL spacing is unaffected by the in-plane field.

The situation is different for relativistic electrons in graphene, as a consequence of the Lorentz invariance of the Dirac equation. One may choose a reference frame in which the electric field vanishes as long as the *drift* velocity  $v_D = E/B$  is smaller than the Fermi velocity, which plays the role of an upper bound for the physically significant velocities in the same manner as the speed of light in relativity (magnetic regime).<sup>14</sup> In addition to the lifted LL degeneracy, the LL spacing is reduced (Lukose *et al.*, 2007; Peres and Castro, 2007), as may be seen from a Lorentz boost into the reference frame which moves at the drift velocity and in which the electric field vanishes. In this reference frame, the magnetic field is reduced by the factor

$$\sqrt{1 - (E/v_F B)^2}, \quad (116)$$

<sup>14</sup> In the opposite case,  $v_D > v_F$ , one may choose a reference system in which the magnetic field vanishes (electric regime) (Jackson, 1999).

such that the LLs (85), which scale as  $\sqrt{B'} = \sqrt{B}[1 - (E/v_F B)^2]^{1/4}$  with the magnetic field, read

$$\epsilon'_{\lambda,n} = \lambda \frac{\hbar v_F}{l_B} [1 - (E/v_F B)^2]^{1/4} \sqrt{2n}, \quad (117)$$

where the primes indicate the physical quantities in the moving frame of reference. When measuring the energy in the original (lab) frame of reference, the above energy spectrum also needs to be transformed into this frame of reference, which amounts to being multiplied by another factor (116), such that the spectrum of relativistic LLs in the presence of an in-plane electric field becomes (Lukose *et al.*, 2007)

$$\epsilon_{\lambda,n;k} = \lambda \frac{\hbar v_F}{l_B} [1 - (E/v_F B)^2]^{3/4} \sqrt{2n} + \hbar \frac{E}{B} k. \quad (118)$$

The quantum-mechanical derivation of this result will be discussed in more detail in Sec. II.D.1 in the context of the generalized Weyl Hamiltonian in a magnetic field.

### D. Landau Levels in Deformed Graphene

As we have discussed in Sec. I.D, a uniaxial strain deforms the graphene sheet and modifies the electronic structure. The induced anisotropy of the Fermi velocity  $w_x \neq w_y$  is essentially washed out by the magnetic field, which yields an effective averaging over the Fermi surface,  $v_F \rightarrow v'_F = \sqrt{w_x w_y}$ . More spectacular are the two further consequences of the deformation; (a) the tilt of the Dirac cones accounted for in the generalized Weyl Hamiltonian (66) and (b) the topological phase transition due to the Dirac point motion. The implication for the LL spectrum are briefly reviewed in the following sections.

#### 1. The generalized Weyl Hamiltonian in a magnetic field

With the help of the Peierls substitution (72) and the expression of the kinetic momentum in terms of ladder operators (80), the generalized Weyl Hamiltonian (66) may be cast into the form

$$H_B^\xi = \xi \frac{\hbar \sqrt{2w_x w_y}}{l_B} \begin{pmatrix} \frac{\tilde{w}_0}{2} (\hat{a} e^{i\varphi} + \text{H.c.}) & \hat{a} \\ \hat{a}^\dagger & \frac{\tilde{w}_0}{2} (\hat{a} e^{i\varphi} + \text{H.c.}) \end{pmatrix}. \quad (119)$$

where

$$\tilde{w}_0 e^{i\varphi} \equiv \frac{w_{0x}}{w_x} + i \frac{w_{0y}}{w_y}, \quad (120)$$

in terms of the effective tilt parameter (70) and the angle  $\varphi$  between the  $x$ -axis and the direction of the effective tilt  $(w_{0x}/w_x, w_{0y}/w_y)$ , renormalized by the Fermi velocities  $w_x$  and  $w_y$  in the  $x$ - and  $y$ -direction, respectively.

The Hamiltonian (119) may be solved quantum-mechanically in a straight-forward, but lengthy manner (Morinari *et al.*, 2009; Peres and Castro, 2007). Instead,

one may also obtain the result in a simpler semi-classical treatment (Goerbig *et al.*, 2008), with the help of the Onsager relation (Lifshitz and Kosevich, 1956; Onsager, 1952) according to which the surface  $S(\epsilon)$  enclosed by a trajectory of constant energy  $\epsilon$  in reciprocal space is quantized as

$$S(\epsilon)l_B^2 = (2\pi)^2 \int_0^\epsilon d\epsilon' \rho(\epsilon') = 2\pi(n + \gamma), \quad (121)$$

where  $n$  is an integer denoting the energy level which coincides with the Landau level in the full quantum treatment. The additional contribution  $\gamma$  is related to a Berry phase acquired by an electron during its cyclotron orbit. Usually, one has  $\gamma = 1/2$  except if there is an extra Berry phase of  $\pi$ , which in our case yields  $\gamma = 0$ , as for graphene with no tilt (Mikitik and Sharlai, 1999). If one considers a density of states which scales as  $\rho(\epsilon) \propto \epsilon^\alpha$ , the energy levels thus scale as

$$\epsilon_n \sim [B(n + \gamma)]^{1/(1+\alpha)}, \quad (122)$$

in the large- $n$  limit.

Because the density of states vanishes linearly at the Dirac point, as in the case of no tilt, i.e.  $\alpha = 1$ , the scaling argument (122) yields the energy levels,

$$\epsilon_{\lambda,n} \simeq \lambda \sqrt{2} \frac{\hbar v_F^*}{l_B} \sqrt{n}, \quad (123)$$

as for unconstrained graphene, apart from a renormalization of the Fermi velocity. The latter is readily obtained from the calculation of the total number of states below the energy  $\epsilon$  within the positive energy cone,

$$N_+(\epsilon) = \frac{1}{(2\pi)^2 \hbar^2 w_x w_y} \int_{\epsilon_+(\tilde{q}) \leq \epsilon} d\tilde{q}_x d\tilde{q}_y = \frac{1}{2\pi \hbar^2 v_F^{*2}} \frac{\epsilon^2}{2}, \quad (124)$$

where we have defined  $\tilde{q}_{x/y} \equiv w_{x/y} q_{x/y}$ , and the renormalized Fermi velocity is

$$v_F^{*2} = \left[ w_x w_y (1 - \tilde{w}_0^2)^{3/2} \right], \quad (125)$$

in terms of the effective tilt parameter (70). This yields the result

$$\epsilon_{\lambda,n} = \lambda \frac{\hbar \sqrt{w_x w_y}}{l_B} (1 - \tilde{w}_0^2)^{3/4} \sqrt{2n} \quad (126)$$

for the LL spectrum in the presence of a tilt, which coincides with the one obtained from the full quantum treatment (Morinari *et al.*, 2009; Peres and Castro, 2007). One finally notices that the LL spacing becomes zero for  $\tilde{w}_0 = 1$ , which corresponds to the condition (69) of maximal tilt for the Dirac cones, as discussed in Sec. I.D – indeed for values of  $\tilde{w}_0$  larger than 1, the isoenergetic lines are no longer closed elliptic orbits but open hyperbolas, for which the energy is not quantised.

## 2. Tilted Dirac cones in a crossed magnetic and electric field

One notices that the form (126) of LLs for tilted Dirac cones is the same as that of the LL spectrum (118) if one interprets the drift velocity  $v_D = E/v_F B$  as an effective electric-field induced tilt. The magnetic regime  $E/B < v_F$  corresponds then to the regime of closed orbits ( $\tilde{w}_0 < 1$ ) and the open hyperbolic orbits may be identified with the electric regime  $E/B > v_F$ . Mathematically, the generalized Weyl Hamiltonian with an in-plane electric field may still be cast into the form (119)

$$H_B^\xi \rightarrow H_{E/B}^\xi = H_B^{\xi'} + \hbar \frac{E}{B} k \mathbb{1}, \quad (127)$$

where  $H_B^{\xi'}$  is the same as that of Eq. (119) if one replaces the tilt parameter  $\tilde{w}_0 \exp(i\varphi)$  by (Goerbig *et al.*, 2009)

$$\tilde{w}_\xi(E) e^{i\varphi_\xi(E)} \equiv \frac{w_{\xi x}}{w_x} + i \frac{w_{\xi y}}{w_y}. \quad (128)$$

Here, the renormalized tilt velocity is given by

$$\mathbf{w}_\xi = (w_{\xi x}, w_{\xi y}) \equiv \mathbf{w}_0 - \xi \frac{\mathbf{E} \times \mathbf{B}}{B^2}, \quad (129)$$

and the angle  $\varphi_\xi$  is the angle between this velocity and the  $x$ -axis.

The resulting energy spectrum is given by

$$\epsilon_{\lambda,n;k}^\xi(E) = \lambda \frac{\hbar \sqrt{w_x w_y}}{l_B} [1 - \tilde{w}_\xi(E)^2]^{3/4} \sqrt{2n} + \hbar \frac{E}{B} k. \quad (130)$$

Naturally one obtains the result (118) for undeformed graphene in an in-plane electric field, for  $w_x = w_y = v_F$  and  $\mathbf{w}_0 = 0$ , as well as the LL spectrum (126) for the generalized Weyl Hamiltonian with tilted Dirac cones for zero in-plane field ( $E = 0$ ). However, the most interesting situation arises when both the tilt and an in-plane field are present, in which case one observes a lifting of the valley degeneracy that is maximal when the electric field is applied perpendicular to the tilt velocity,  $\mathbf{E} \perp \mathbf{w}_0$  (Goerbig *et al.*, 2009).

Notice that, in order to obtain an effect on the order of  $\sim 1\%$ , extremely large electric fields would be required (on the order of  $10^6$  V/m) for a 10% deformation of the lattice (Goerbig *et al.*, 2009). It seems therefore difficult to observe the effect in graphene, e.g. in high-field transmission spectroscopy or transport measurements, whereas the effect may be more visible in  $\alpha$ -(BEDT-TTF)<sub>2</sub>I<sub>3</sub>, where the Dirac cones are naturally tilted (Katayama *et al.*, 2006; Kobayashi *et al.*, 2007) and where lower electric fields would be required for a comparable effect due to a roughly ten times smaller effective Fermi velocity.

## III. ELECTRONIC INTERACTIONS IN GRAPHENE – INTEGER QUANTUM HALL REGIME

In the preceding sections, we have discussed the electronic properties of graphene within a one-particle model,

i.e. we have neglected the Coulomb interaction between the electrons. In many materials, the one-particle picture yields the correct qualitative description of the electronic properties and is modified only quantitatively if one includes the electron-electron interactions within perturbation theory (Giuliani and Vignale, 2005; Mahan, 1993). Notice, however, that there exists a class of materials – strongly correlated electron systems – the electronic properties of which may not be described correctly, not even on the qualitative level, within a one-particle picture.

In order to quantify the role of the electronic interactions, i.e. the correlations, in graphene, one needs to compare the characteristic Coulomb energy  $E_{int} = e^2/\varepsilon\ell$  at the average inter-electronic distance ( $\varepsilon$  is the dielectric constant describing the environment the 2D electron gas is embedded in) to the kinetic one  $E_{kin}(k_F)$  at the same length scale, given in terms of the Fermi wave vector  $k_F$ ,  $\ell \sim k_F^{-1}$ ,

$$r_s = \frac{E_{int}}{E_{kin}}. \quad (131)$$

If this dimensionless interaction parameter becomes very large,  $r_s \gg 1$ , the electrons are strongly correlated. In non-relativistic 2D metals with a parabolic band dispersion,  $E_{kin} \sim \hbar^2 k_F^2/m_b$ , the dimensionless parameter reads

$$r_s = \frac{m_b e^2}{\hbar^2 \varepsilon} \ell \sim \frac{1}{a_0^* k_F}, \quad (132)$$

in terms of the effective Bohr radius  $a_0^* = a_0 \varepsilon m_0/m_b$ , where  $a_0 = 0.5 \text{ \AA}$  is the Bohr radius in vacuum and  $m_b/m_0$  the ratio between the band and the bare electron mass. The relevance of electronic correlations therefore increases in the dilute limit when  $\ell \gg a_0^*$ . Notice that the parameter  $r_s$ , which is also called Wigner-Seitz radius, plays the role of a length measured in units of the effective Bohr radius  $a_0^*$ .

The same argument applied to graphene yields a completely different result. Whereas the scaling of the Coulomb energy remains the same, that of the kinetic energy is changed due to the linearity of the band dispersion. As a consequence the dimensionless interaction parameter in graphene reads

$$\alpha_G = \frac{E_{int}}{E_{kin}} = \frac{e^2}{\hbar \varepsilon v_F} \simeq \frac{2.2}{\varepsilon}, \quad (133)$$

independent of the carrier density.<sup>15</sup> The correlations are therefore in an intermediate regime but may be decreased if the graphene sheet is embedded in an environment with a large dielectric constant. Notice that the

<sup>15</sup> In contrast to an electron system with a parabolic band dispersion, this parameter can no longer be interpreted as a dimensionless radius, and we therefore use the notation  $\alpha_G$  rather than  $r_s$ .

expression (133) is the same as that of the fine structure constant  $\alpha = e^2/\hbar \varepsilon c = 1/137$  in quantum electrodynamics (Weinberg, 1995) if one replaces the Fermi velocity by the velocity of light, which is roughly 300 times larger. One therefore calls  $\alpha_G$  alternatively the *graphene fine structure constant*.

*Long-range versus short-range interactions.* Another important aspect of interacting electrons is the range of the interaction potential. Whereas the underlying Coulomb potential  $e^2/\varepsilon r$  is long-range, short-range interaction models such as the Hubbard model are often – and successfully – used in the description of correlated metals. The use of such a short-range interaction may be justified by the screening properties of interacting electrons, which are correctly captured in a Thomas-Fermi approach (Giuliani and Vignale, 2005; Mahan, 1993) according to which the Coulomb interaction potential is screened above a characteristic screening length  $\lambda_{TF} \sim 1/k_{TF}$ .<sup>16</sup> In 2D, the Thomas-Fermi wave vector

$$k_{TF} \simeq r_s k_F \quad (134)$$

is given in terms of the dimensionless interaction parameter (131) and the Fermi wave vector  $k_F$ .<sup>17</sup>

One notices that, for metals with a parabolic dispersion relation, the Thomas-Fermi wave vector is simply given in terms of the inverse effective Bohr radius,  $k_{TF} \sim 1/a_0^*$ , independent of the electronic density. Unless the band mass is very small as compared to the bare electron mass or the dielectric constant of the host material very large, the Coulomb interaction is therefore screened on the atomic scale. A description of such systems in the framework of short-range interaction models, such as the Hubbard model, then becomes better justified than in systems with a small band mass or a prominent dielectric constant (such as in 2D electron systems in GaAs heterostructures). Typical examples, where short-range interaction model yields valuable physical insight, are heavy-fermion compounds [for a review see Ref. (Coleman, 2003)].

The situation is again drastically different in graphene where the Thomas-Fermi wave vector (134) becomes

$$k_{TF}^G \simeq \alpha_G k_F \simeq \frac{2.2}{\varepsilon} k_F \sim \sqrt{n_{el}}, \quad (135)$$

i.e. it vanishes at the Dirac points where the carrier density goes to zero, and the screening length then diverges.<sup>18</sup> Notice that even for doped graphene, where

<sup>16</sup> Notice that the Thomas-Fermi approach is restricted to static screening effects, whereas dynamic screening require a more complex treatment, e.g. in the framework of the random-phase approximation.

<sup>17</sup> In three space dimensions, the relation reads  $k_{TF}^2 \simeq r_s k_F^2$ .

<sup>18</sup> Due to this divergence of the screening length, one principally needs to describe screening beyond the level of linear-response theory (Katsnelson, 2006).

one may typically induce carrier densities on the order of  $10^{12} \text{ cm}^{-2}$ , the screening length is  $\lambda_{TF} \gtrsim 10 \text{ nm}$ , i.e. much larger than the lattice scale.

One thus comes to the conclusion that the relevant electronic interactions in graphene are long-range Coulomb interactions that may not be captured, in contrast to other materials with a parabolic band dispersion, within models such as the Hubbard model (Herbut, 2006, 2007a). We therefore investigate, in this section, the fate of the long-range Coulomb interaction in a strong magnetic field. In Sec. III.A, we decompose the Coulomb interaction Hamiltonian in the two-spinor basis of the low-energy electronic wave functions in graphene and comment on its symmetry with respect to the valley pseudospin. The role of these interactions in the particle-hole excitation spectrum is studied in Sec. III.B, where we discuss the resulting collective excitations in the IQHE regime, which allows for a perturbative treatment. The strong-correlation regime of partially filled LLs (regime of the fractional quantum Hall effect) is presented separately in Sec. V.

### A. Decomposition of the Coulomb interaction in the Two-Spinor Basis

Generally, the Coulomb interaction for 2D electrons may be accounted for by the Hamiltonian

$$H_{int} = \frac{1}{2} \sum_{\mathbf{q}} v(\mathbf{q}) \rho(-\mathbf{q}) \rho(\mathbf{q}), \quad (136)$$

in terms of the Fourier components  $\rho(\mathbf{q}) = \int d^2r \exp(-i\mathbf{q} \cdot \mathbf{r}) \psi^\dagger(\mathbf{r}) \psi(\mathbf{r})$  of the electronic density  $\psi^\dagger(\mathbf{r}) \psi(\mathbf{r})$  and the 2D Fourier transformed  $1/r$  Coulomb potential,  $v(\mathbf{q}) = 2\pi e^2 / \varepsilon |\mathbf{q}|$ . If one takes into account the electronic spin  $\sigma = \uparrow, \downarrow$ , the Coulomb interaction respects the associated SU(2) symmetry, and the Fourier components are then simply the sum of the densities  $\rho_\sigma(\mathbf{q})$  in both spin orientations,

$\rho(\mathbf{q}) = \rho_\uparrow(\mathbf{q}) + \rho_\downarrow(\mathbf{q})$ . For notational convenience, we neglect the spin index in the following discussion keeping in mind that the spin SU(2) symmetry is respected. The density operators may be decomposed in the basis of the spinor wave functions (96) and (97) for relativistic electrons in graphene,

$$\rho(\mathbf{q}) = \sum_{\substack{\lambda n, m; \xi \\ \lambda' n', m'; \xi'}} \psi_{\lambda n, m; \xi}^\dagger e^{-i\mathbf{q} \cdot \mathbf{r}} \psi_{\lambda' n', m'; \xi'} c_{\lambda n, m; \xi}^\dagger c_{\lambda' n', m'; \xi'}, \quad (137)$$

where  $c_{\lambda n, m; \xi}^{(\dagger)}$  are fermion operators in second quantization that annihilate (create) an electron in the quantum state

$$\begin{aligned} \psi_{\lambda n, m; \xi = +} &= \begin{pmatrix} 1_n^* |n-1, m\rangle \\ \lambda 2_n^* |n, m\rangle \end{pmatrix} e^{i\mathbf{K} \cdot \mathbf{r}} \\ \text{and } \psi_{\lambda n, m; \xi = -} &= \begin{pmatrix} -\lambda 2_n^* |n, m\rangle \\ 1_n^* |n-1, m\rangle \end{pmatrix} e^{-i\mathbf{K} \cdot \mathbf{r}}. \end{aligned} \quad (138)$$

In order to avoid confusion in the case of inter-valley coupling, we use now a representation in which the first spinor component represents the amplitude on the A sublattice and the second on the B sublattice for both valleys. Contrary to the expressions (96) and (97), the state (138) is valid for both  $n = 0$  and  $n \neq 0$  by using the short-hand notation  $1_n^* \equiv \sqrt{(1 - \delta_{n,0})/2}$  and  $2_n^* \equiv \sqrt{(1 + \delta_{n,0})/2}$ . Furthermore, we have explicitly taken into account the rapidly oscillating part  $\exp(i\xi \mathbf{K} \cdot \mathbf{r})$  due to the two different valleys, whereas the expressions (96) and (97) are only concerned with the slowly varying envelope function. Explicitly, the Fourier components of the density operator (137) then read

$$\rho(\mathbf{q}) = \sum_{\substack{\lambda n, \lambda' n' \\ \xi, \xi'}} \mathcal{F}_{\lambda n, \lambda' n'}^{\xi, \xi'}(\mathbf{q}) \bar{\rho}_{\lambda n, \lambda' n'}^{\xi, \xi'}(\mathbf{q}), \quad (139)$$

in terms of the *reduced* density operators

$$\bar{\rho}_{\lambda n, \lambda' n'}^{\xi, \xi'}(\mathbf{q}) = \sum_{m, m'} \langle m | e^{-i[\mathbf{q} + (\xi - \xi') \mathbf{K}] \cdot \mathbf{R}} | m' \rangle c_{\lambda n, m; \xi}^\dagger c_{\lambda' n', m'; \xi'}, \quad (140)$$

which may also be interpreted as *magneto-exciton* operators associated with a particular inter-LL transition (see Sec. IV.A), and the *form factors*

$$\mathcal{F}_{\lambda n, \lambda' n'}^{\xi, \xi'}(\mathbf{q}) \equiv \mathcal{F}_{\lambda n, \lambda' n'}^{\xi, \xi}(\mathbf{q}) = 1_n^* 1_{n'}^* \langle n-1 | e^{-i\mathbf{q} \cdot \boldsymbol{\eta}} | n'-1 \rangle + \lambda \lambda' 2_n^* 2_{n'}^* \langle n | e^{-i\mathbf{q} \cdot \boldsymbol{\eta}} | n' \rangle \quad (141)$$

for intra-valley and

$$\mathcal{F}_{\lambda n, \lambda' n'}^{+, -}(\mathbf{q}) = \lambda 1_n^* 2_{n'}^* \langle n | e^{-i(\mathbf{q} + 2\mathbf{K}) \cdot \boldsymbol{\eta}} | n'-1 \rangle - \lambda' 1_n^* 2_{n'}^* \langle n-1 | e^{-i(\mathbf{q} + 2\mathbf{K}) \cdot \boldsymbol{\eta}} | n' \rangle = [\mathcal{F}_{\lambda' n', \lambda n}^{-, +}(-\mathbf{q})]^* \quad (142)$$

for inter-valley processes. Here, we have used the decomposition  $\mathbf{r} = \mathbf{R} + \boldsymbol{\eta}$  of the position operator into its guiding center and cyclotron coordinate (see Sec. II.A.1) and the fact that  $f_1(\boldsymbol{\eta}) f_2(\mathbf{R}) |n, m\rangle = f_1(\boldsymbol{\eta}) |n\rangle \otimes f_2(\mathbf{R}) |m\rangle$ , for two

arbitrary functions  $f_1$  and  $f_2$ . The full expressions for the matrix elements in Eqs. (140), (141), and (142) may be found in Appendix A.

In terms of the reduced density operators (140), the interaction Hamiltonian (136) reads

$$H_{int} = \frac{1}{2} \sum_{\mathbf{q}} \sum_{\substack{\lambda_1 n_1 \dots \lambda_4 n_4 \\ \xi_1 \dots \xi_4}} v_{\lambda_1 n_1 \dots \lambda_4 n_4}^{\xi_1 \dots \xi_4}(\mathbf{q}) \bar{\rho}_{\lambda_1 n_1, \lambda_3 n_3}^{\xi_1, \xi_3}(-\mathbf{q}) \bar{\rho}_{\lambda_2 n_2, \lambda_4 n_4}^{\xi_2, \xi_4}(\mathbf{q}), \quad (143)$$

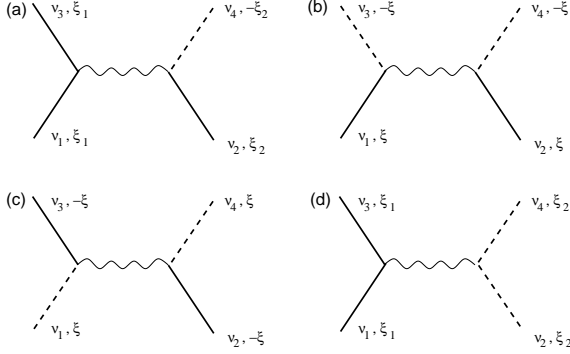


Figure 13 Diagrammatic representation of the interaction vertex (we use the short-hand notation  $\nu_i = (\lambda_i n_i, m_i)$  for the quantum numbers); (a) vertex associated with terms of the form  $v_{\lambda_1 n_1 \dots \lambda_4 n_4}^{\xi, \xi', -\xi'}$  or  $v_{\lambda_1 n_1 \dots \lambda_4 n_4}^{\xi, -\xi, \xi', \xi'}$ , (b) vertex of *Umklapp* type,  $v_{\lambda_1 n_1 \dots \lambda_4 n_4}^{\xi, -\xi, -\xi}$ , (c) vertex of *backscattering* type,  $v_{\lambda_1 n_1 \dots \lambda_4 n_4}^{\xi, -\xi, -\xi, \xi}$  and (d) vertex respecting the SU(2) valley-pseudospin symmetry  $v_{\lambda_1 n_1 \dots \lambda_4 n_4}^{\xi, -\xi, \xi', -\xi'}$ .

where the interaction vertex is defined as

$$v_{\lambda_1 n_1 \dots \lambda_4 n_4}^{\xi_1 \dots \xi_4}(\mathbf{q}) = \frac{2\pi e^2}{\varepsilon |\mathbf{q}|} \mathcal{F}_{\lambda_1 n_1, \lambda_3 n_3}^{\xi_1, \xi_3}(-\mathbf{q}) \mathcal{F}_{\lambda_2 n_2, \lambda_4 n_4}^{\xi_2, \xi_4}(\mathbf{q}). \quad (144)$$

### 1. SU(2) valley symmetry

One notices that, in contrast to the SU(2) symmetry associated with the physical spin, the Hamiltonian (143) does not respect a similar valley-pseudospin symmetry due to possible inter-valley couplings. An SU(2) valley-pseudospin symmetry would be respected for the case  $\xi_1 = \xi_3$  and  $\xi_2 = \xi_4$ , i.e. if the interaction vertex (144)

$$v_{\lambda_1 n_1 \dots \lambda_4 n_4}^{\xi_1 \dots \xi_4}(\mathbf{q}) \propto \delta_{\xi_1, \xi_3} \delta_{\xi_2, \xi_4}. \quad (145)$$

One may show, however, that the SU(2) valley-pseudospin symmetry is *approximately* respected when considering the different classes of interaction vertices depicted in Fig. 13.

- Consider the diagram in Fig. 13(a), which represents a vertex of the type  $v_{\lambda_1 n_1 \dots \lambda_4 n_4}^{\xi, \xi', -\xi'}$  or  $v_{\lambda_1 n_1 \dots \lambda_4 n_4}^{\xi, -\xi, \xi', \xi'}$ . In this case, the particle on the left remains in the same valley whereas that on the

right changes the valley. Such a process would require a momentum transfer of  $\pm \mathbf{K}$ , i.e. of the wave vector connecting the two valleys, and therefore does not respect momentum conservation, in the absence of a magnetic field. Naturally, momentum is not a good quantum number here due to the magnetic field, but momentum conservation manifests itself by an exponential suppression of such processes. In order to appreciate this point, we need to consider the Gaussian in the form factors (141) and (142),

$$\mathcal{F}_{\lambda n, \lambda' n'}^{\xi, \xi'}(\mathbf{q}) \propto e^{-|\mathbf{q} + (\xi - \xi') \mathbf{K}|^2 l_B^2 / 4}, \quad (146)$$

as discussed in Appendix A [see Eq. (A2)]. One therefore sees that the interaction vertex contains a Gaussian term

$$\begin{aligned} v_{\lambda_1 n_1 \dots \lambda_4 n_4}^{\xi, \xi', -\xi'}(\mathbf{q}) &\propto e^{-(q^2 + |\mathbf{q} \pm \mathbf{K}|^2) l_B^2 / 4} \\ &\sim e^{-(|\mathbf{q}'|^2 + |\mathbf{K}|^2 / 4) l_B^2 / 2} \\ &\sim e^{-|\mathbf{K}|^2 l_B^2 / 8} \sim e^{-\# l_B^2 / a^2}, \end{aligned} \quad (147)$$

where  $\#$  represents an unimportant numerical factor and where we have shifted the momentum  $\mathbf{q}' = \mathbf{q} \pm \mathbf{K}/2$  in the second step. The processes associated with the diagram in Fig. 13(a) are thus exponentially suppressed in  $l_B^2 / a^2 \simeq 10^4 / B[\text{T}]$  and may safely be neglected in the range of physically accessible magnetic fields.

- The same fate is reserved for the diagram in Fig. 13(b), which represents a process of *Umklapp* type. In this case, the vertex reads

$$\begin{aligned} v_{\lambda_1 n_1 \dots \lambda_4 n_4}^{\xi, -\xi, -\xi}(\mathbf{q}) &\propto e^{-(|\mathbf{q} + \mathbf{K}|^2 + |\mathbf{q} - \mathbf{K}|^2) l_B^2 / 4} \\ &\sim e^{-|\mathbf{K}|^2 l_B^2 / 2} \sim e^{-\# l_B^2 / a^2}, \end{aligned} \quad (148)$$

which is again exponentially small in  $l_B^2 / a^2$ .

- The situation is different for *backscattering*-type diagrams [Fig. 13(c)], in which case the interaction vertex is

$$v_{\lambda_1 n_1 \dots \lambda_4 n_4}^{\xi, -\xi, -\xi, \xi}(\mathbf{q}) \propto e^{-(|\mathbf{q} \pm \mathbf{K}|^2 + |\mathbf{q} \pm \mathbf{K}|^2) l_B^2 / 4}. \quad (149)$$

One may then redefine the wave vector  $\mathbf{q}' = \mathbf{q} \pm \mathbf{K}$ , which is eventually an integration variable in the

interaction Hamiltonian (143), and the interaction vertex becomes

$$v_{\lambda_1 n_1 \dots \lambda_4 n_4}^{\xi, -\xi, -\xi, \xi}(\mathbf{q}') \propto \frac{2\pi e^2}{\varepsilon |\mathbf{q}' \mp \mathbf{K}|} e^{-q'^2 l_B^2 / 2} \quad (150)$$

$$\sim \frac{2\pi e^2}{\varepsilon |\mathbf{K}|} e^{-q'^2 l_B^2 / 2}.$$

As an order of magnitude, with  $|\mathbf{K}| \sim 1/a$ , one then notices that the backscattering interaction vertex is suppressed by a factor of  $a/l_B \sim 0.005 \times \sqrt{B[\text{T}]}$  as compared to the leading energy scale  $e^2/\varepsilon l_B$ .

- The leading interaction vertex is therefore the SU(2) valley-pseudospin symmetric one depicted in Fig. 13(d), for which the rapidly oscillating contribution at  $\mathbf{K}$  vanishes, as may be seen directly from the form factors (142).

The above argument, which generalizes symmetry considerations for the interactions in a single relativistic LL (Alicia and Fisher, 2006; Doretto and Morais Smith, 2007; Goerbig *et al.*, 2006; Herbut, 2007b), shows that although the valley SU(2) symmetry is not an exact symmetry, such as the SU(2) symmetry associated with the physical spin, it is *approximately* respected by the long-range Coulomb interaction. Valley-symmetry breaking terms are due to lattice effects beyond the continuum limit and therefore suppressed by the small factor  $a/l_B$ , which quantifies precisely corrections due to effects on the lattice scale. If one takes into account the additional spin degree of freedom, the resulting four-fold spin-valley degeneracy may then be described within the larger SU(4) symmetry group, which turns out to be relevant in the description of strong-correlation effects in partially filled LLs (Sec. V).

---

## 2. SU(4) spin-valley symmetric Hamiltonian

The SU(4)-symmetric part of the interaction Hamiltonian (143) finally reads

$$H_{int}^{sym} = \frac{1}{2} \sum_{\mathbf{q}} \sum_{\lambda_1 n_1 \dots \lambda_4 n_4} v_{\lambda_1 n_1 \dots \lambda_4 n_4}^{sym}(\mathbf{q}) \bar{\rho}_{\lambda_1 n_1, \lambda_3 n_3}(-\mathbf{q}) \bar{\rho}_{\lambda_2 n_2, \lambda_4 n_4}(\mathbf{q}), \quad (151)$$

where the symmetric interaction vertex is

$$v_{\lambda_1 n_1 \dots \lambda_4 n_4}^{sym}(\mathbf{q}) = \frac{2\pi e^2}{\varepsilon |\mathbf{q}|} \mathcal{F}_{\lambda_1 n_1, \lambda_3 n_3}(-\mathbf{q}) \mathcal{F}_{\lambda_2 n_2, \lambda_4 n_4}(\mathbf{q}), \quad (152)$$

in terms of the reduced density operators

$$\bar{\rho}_{\lambda n, \lambda' n'}(\mathbf{q}) \equiv \sum_{\xi=\pm} \rho_{\lambda n, \lambda' n'}^{\xi, \xi}(\mathbf{q}) = \sum_{\xi=\pm} \sum_{\sigma=\uparrow, \downarrow} \sum_{m, m'} \langle m | e^{-i\mathbf{q} \cdot \mathbf{R}} | m' \rangle c_{\lambda n, m; \xi, \sigma}^\dagger c_{\lambda' n', m'; \xi, \sigma}, \quad (153)$$

where we have explicitly taken into account the spin index  $\sigma = \uparrow, \downarrow$  in the last line.

We finally notice that the graphene form factors (141) may also be rewritten in terms of the LL form factors

$$F_{n, n'}(\mathbf{q}) = \langle n | e^{-i\mathbf{q} \cdot \boldsymbol{\eta}} | n' \rangle, \quad (154)$$

which arise in a similar decomposition of the Coulomb interaction in Landau states in the non-relativistic 2D electron gas, as

$$\mathcal{F}_{\lambda n, \lambda' n'}(\mathbf{q}) = 1_n^* 1_{n'}^* F_{n-1, n'-1}(\mathbf{q}) + \lambda \lambda' 2_n^* 2_{n'}^* F_{n, n'}(\mathbf{q}). \quad (155)$$

To summarize the differences and the similarities between the interaction Hamiltonians in graphene and the non-relativistic 2D electron system, one first realizes that its structure is the same if one replaces the LL form factor (154) by the graphene form factors (141) and if one takes into account the larger (approximate) internal symmetry SU(4), due to the spin-valley degeneracy, instead of the spin SU(2) symmetry.

In the remainder of this section, we neglect the symmetry-breaking part of the Hamiltonian and consider the Coulomb interaction to respect the SU(2) valley symmetry.

## B. Particle-Hole Excitation Spectrum

The considerations of the previous subsection allow us to discuss the role of the Coulomb interaction within a perturbative approach in the IQHE regime for  $\nu = \pm 2(2n + 1)$ , where the (non-interacting) ground state is non-degenerate and separated by the cyclotron gap  $\sqrt{2}(\hbar v_F/l_B)(\sqrt{n+1} - \sqrt{n})$  from its excited states. Quite generally, the inter-LL transitions evolve into coherent collective excitations, as a consequence of these Coulomb interactions. Prominent examples in the non-relativistic 2D electron gas are the upper-hybrid mode (sometimes also called *magneto-plasmon*), which is the magnetic-field counterpart of the usual 2D plas-



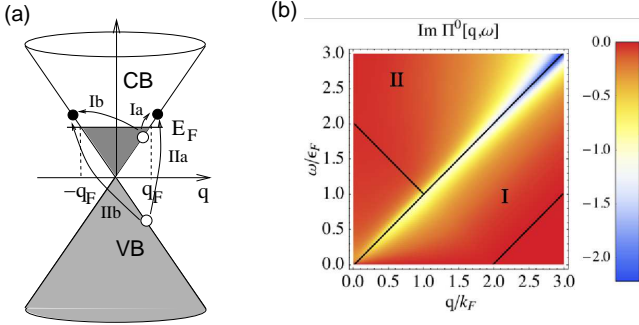


Figure 14 Zero-field particle-hole excitation spectrum for doped graphene. (a) Possible intraband (I) and interband (II) single-pair excitations in doped graphene. The excitations close to the Fermi energy may have a wave-vector transfer comprised between  $q = 0$  (Ia) and  $q = 2q_F$  (Ib), in terms of the Fermi wave vector  $q_F$ . (b) Spectral function  $\text{Im } \Pi_0(\mathbf{q}, \omega)$  in the wave-vector/energy plane. The regions corresponding to intra- and interband excitations are denoted by (I) and (II), respectively.

mon (Giuliani and Vignale, 2005), and *magneto-excitons* (Kallin and Halperin, 1984). In the present subsection, we discuss how these modes manifest themselves in graphene in comparison with the non-relativistic 2D electron gas.

### 1. Graphene particle-hole excitation spectrum at $B = 0$

Before discussing the particle-hole excitation spectrum (PHES) for graphene in the IQHE regime, we briefly review the one for  $B = 0$  as well as its associated collective modes (Ando, 2006a; Hwang and Das Sarma, 2007; Shung, 1986; Wunsch *et al.*, 2006). Quite generally, the PHES is determined by the spectral function

$$S(\mathbf{q}, \omega) = -\frac{1}{\pi} \text{Im } \Pi(\mathbf{q}, \omega), \quad (156)$$

which may be viewed as the spectral weight of the allowed particle-hole excitations, in terms of the polarizability  $\Pi(\mathbf{q}, \omega)$ , which plays the role of a density-density response function (Giuliani and Vignale, 2005; Mahan, 1993).

The particle-hole excitations for non-interacting electrons in doped graphene are depicted in Fig. 14.<sup>19</sup> In contrast to the PHES of electrons in a single parabolic band (the non-relativistic 2D electron gas), there are two different types of excitations: intraband excitations [labeled by I in Fig. 14(a)], where both the electron and the hole reside in the conduction band (CB), and interband excitations [labeled by II in Fig. 14(a)], where an electron is promoted from the valence band (VB) to the CB. In undoped graphene, there exist naturally only interband excitations (II). If the electron and the hole have an energy

close to the Fermi energy, the allowed excitations imply a wave-vector transfer that lies in between  $q = 0$  (Ia) and  $q = 2q_F$  (Ib). At non-zero values  $\epsilon$  of the transferred energy, one needs to search for available quantum states at larger wave vectors, and the particle-hole pair wave vector is then restricted to  $\epsilon/\hbar v_F < q < 2q_F + \epsilon/\hbar v_F$ , as a consequence of the linear dispersion relation in graphene. This gives rise to the region I, which describes the *intra-band particle-hole continuum*, and its linear boundaries in the PHES described by the spectral function in Fig. 14(b).

In addition to intraband excitations, one notices that interband excitations become possible above a threshold energy of  $\epsilon_F$ , where an electron at the top of the VB (at  $\mathbf{q} = 0$ ) may be promoted to an empty state slightly above the Fermi energy. The associated wave-vector transfer is naturally  $q = q_F$ . The point  $(q_F, \epsilon_F)$  marks the bottom of the region II in Fig. 14(b), which determines the region of allowed interband excitations (*interband particle-hole continuum*). Direct interband excitations with zero wave-vector transfer are possible above an energy of  $2\epsilon_F$ .

Another aspect of the PHES in Fig. 14 is the strong concentration of spectral weight around the central diagonal  $\omega = \hbar v_F |\mathbf{q}|$ . This concentration is a particularity of graphene due to the electrons' chirality (Polini *et al.*, 2008). Indeed, if one considers a  $2q_F$  backscattering process in the vicinity of the Fermi energy in the CB, Eq. (50) indicates that the chirality, i.e. the projection of the sublattice-pseudospin on the direction of the wave vector, is preserved. The inversion of the direction of propagation in the  $2q_F$  process would therefore require an inversion of the A and B sublattices that is not supported by most of the scattering or interaction processes. This effect is reflected by a strong suppression of the spectral weight when approaching the right boundary of the region I in the PHES associated with processes of the type Ib in Fig. 14(a). Similarly, the conservation of the electrons' chirality (50) favors  $2q_F$  processes in the interband region (II) and the suppression of direct  $\mathbf{q} = 0$  interband excitations of the type IIa in Fig. 14(a). Notice that, although the direction of the wave vector is inverted in a  $2q_F$  process, this indicates still the absence of backscattering because the group velocity  $\mathbf{v} = \nabla_{\mathbf{q}} \epsilon_{\mathbf{q}}^\lambda / \hbar = \lambda v_F \mathbf{q} / |\mathbf{q}|$  remains unchanged – the change in the sign due to the inversion of the wave vector is indeed canceled by the one associated with the change of the band index.

*a. Formal calculation of the spectral function.* In order to obtain the spectral function, it is apparent from Eq. (156) that one needs to calculate the polarizability  $\Pi(\mathbf{q}, \omega)$  of the 2D system, which may be found with the help of the Green's functions  $G(\mathbf{q}, \omega)$ ,

$$\Pi(\mathbf{q}, \omega) = -i \text{Tr} \int \frac{d\omega'}{2\pi} \sum_{\mathbf{q}'} G(\mathbf{q}', \omega') G(\mathbf{q} + \mathbf{q}', \omega + \omega'), \quad (157)$$

<sup>19</sup> We consider here only the case of a Fermi energy  $\epsilon_F$  in the conduction band, for simplicity.

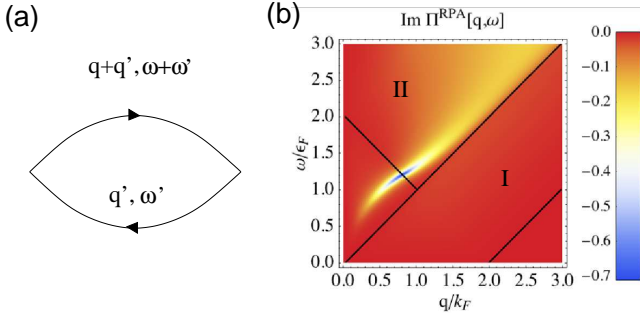


Figure 15 (a) Particle-hole bubble diagram (polarizability), in terms of Green's functions  $G(\mathbf{q}, \omega)$  (lines). (b) Spectral function  $\text{Im} \Pi_{RPA}(\mathbf{q}, \omega)$  for doped graphene in the wave-vector/energy plane. The electron-electron interactions are taken into account within the RPA. We have chosen  $\alpha_G = 1$  here.

where  $\text{Tr}$  means the trace since the Greens functions are  $2 \times 2$  matrices as a consequence of the matrix character of the kinetic Hamiltonian. Diagrammatically, the polarizability may be represented by the so-called bubble diagram shown in Fig. 15(a), and one finds for non-interacting electrons in graphene (Ando, 2006a; Hwang and Das Sarma, 2007; Polini *et al.*, 2008; Shung, 1986; Wunsch *et al.*, 2006)

$$\Pi^0(\mathbf{q}, \omega) = \frac{g}{\mathcal{A}} \sum_{\mathbf{q}', \lambda, \lambda'} \frac{n(\tilde{\epsilon}_{\mathbf{q}'}^{\lambda'}) - n(\tilde{\epsilon}_{\mathbf{q}'+\mathbf{q}}^{\lambda'})}{\tilde{\epsilon}_{\mathbf{q}'}^{\lambda'} - \tilde{\epsilon}_{\mathbf{q}'+\mathbf{q}}^{\lambda'} + \hbar\omega + i\delta} C_{\lambda\lambda'}(\mathbf{q}', \mathbf{q}'+\mathbf{q}), \quad (158)$$

where  $\tilde{\epsilon}_{\mathbf{q}}^{\lambda} = \lambda \hbar v_F |\mathbf{q}| - \epsilon_F$  is the energy of the quantum state  $\psi_{\lambda}(\mathbf{q})$  measured from the Fermi energy  $\epsilon_F$ ,  $g = 4$  takes into account the four-fold spin-valley degeneracy, and  $n(\tilde{\epsilon}_{\mathbf{q}}^{\lambda})$  is the Fermi-Dirac distribution function that reduces to a Heavyside step function  $n(\tilde{\epsilon}_{\mathbf{q}}^{\lambda}) = \Theta(-\tilde{\epsilon}_{\mathbf{q}}^{\lambda})$  at zero temperature. Equation (158) is nothing other than the Lindhard function (Giuliani and Vignale, 2005; Mahan, 1993), apart from the factor

$$C_{\lambda\lambda'}(\mathbf{q}', \mathbf{q}'+\mathbf{q}) \equiv \frac{1 + \lambda\lambda' \cos \theta_{\mathbf{q}', \mathbf{q}'+\mathbf{q}}}{2}, \quad (159)$$

in terms of the angle  $\theta_{\mathbf{q}', \mathbf{q}'+\mathbf{q}}$  between  $\mathbf{q}'$  and  $\mathbf{q}'+\mathbf{q}$ , which takes into account the particular chirality properties of graphene – as already mentioned above, this chirality factor vanishes for backscattering processes, i.e. for intraband ( $\lambda = \lambda'$ )  $2q_F$  processes with  $\theta_{\mathbf{q}', \mathbf{q}'+\mathbf{q}} = \pi$  as well as for interband ( $\lambda = -\lambda'$ )  $q = 0$  processes with  $\theta_{\mathbf{q}', \mathbf{q}'+\mathbf{q}} = 0$  or  $2\pi$ .

Notice finally that the quantity  $\delta$  in Eq. (158) is an infinitesimal energy in the case of pure graphene and may be used (for finite values) as a phenomenological measure of the impurity broadening  $\delta \simeq \hbar/\tau$ , in terms of a life time  $\tau$  of the excitations.

*b. Polarizability in the random-phase approximation.* The diagrammatic approach is particularly adapted for taking into account the electronic interactions on the

level of the random-phase approximation (RPA), which amounts to calculating a geometric series of bubble diagrams and which has shown to yield reliable results for doped graphene (Hwang and Das Sarma, 2007; Sabio *et al.*, 2008; Wunsch *et al.*, 2006). The RPA has also been applied to undoped graphene (González *et al.*, 1994, 1999), but its validity has been questioned (Gangadharaiah *et al.*, 2008; Kotov *et al.*, 2007) because of the vanishing density of states, which would require to take into account diagrams beyond the RPA (Katsnelson, 2006). The RPA polarizability then becomes

$$\Pi^{RPA}(\mathbf{q}, \omega) = \frac{\Pi^0(\mathbf{q}, \omega)}{\epsilon^{RPA}(\mathbf{q}, \omega)}, \quad (160)$$

in terms of the polarizability (158) for non-interacting electrons and the dielectric function

$$\epsilon^{RPA}(\mathbf{q}, \omega) = 1 - \frac{2\pi e^2}{\epsilon |\mathbf{q}|} \Pi^0(\mathbf{q}, \omega). \quad (161)$$

The spectral function associated with the RPA polarizability (160), which is shown in Fig. 15(b), reveals the characteristic coherent 2D *plasmon* mode, which corresponds to the solution of the implicit equation  $\epsilon^{RPA}(\mathbf{q}, \omega_{pl}) = 0$  and the dispersion relation of which reads

$$\omega_{pl}(q) \simeq \sqrt{\frac{2e^2 \epsilon_F}{\hbar^2 \epsilon}} q \quad (162)$$

in the small- $q$  limit (Shung, 1986; Wunsch *et al.*, 2006). Interestingly, this equation is valid also for non-relativistic electrons in conventional 2D electron systems (Stern, 1967) if one takes into account the difference in the density dependence of the Fermi energy ( $\epsilon_F = \pi n_{el}/m_b$  for non-relativistic 2D electrons and  $\epsilon_F = \hbar v_F \sqrt{\pi n_{el}}$  in graphene) as well as that in the Fermi velocity ( $v_F = \sqrt{2\epsilon_F/m_b}$  for non-relativistic electrons, as compared to a constant  $v_F$  in graphene). Notice that the dispersion relation is restricted to small values of  $q$  (as compared to the Fermi wave vector  $k_F$ ), whereas the numerical solution presented in Fig. 15 indicates that the asymptotic dependence of the plasmon mode is indeed given by the central diagonal  $\omega_{uh}(q) \gtrsim v_F q$  (Shung, 1986; Wunsch *et al.*, 2006). Therefore, contrary to the plasmon in 2D metals with a parabolic dispersion relation, the plasmon in graphene does not enter region I, but only the interband particle-hole continuum (region II). In this region, the Landau damping is less efficient, and the coherence of the mode thus survives to a certain extent without decaying into incoherent particle-hole excitations.

## 2. Polarizability for $B \neq 0$

In the case of a strong magnetic field applied perpendicular to the graphene sheet, one needs to take into ac-

count the quantization of the kinetic energy into relativistic LLs described in Sec. II.A.1, as well as the spinorial eigenfunctions  $\psi_{n\lambda,m}^\xi$  in the calculation of the po-

larizability. One finds a similar expression for the zero-temperature polarizability of non-interacting electrons as in Eq. (158),

$$\Pi_B^0(\mathbf{q}, \omega) = g \sum_{\lambda n, \lambda' n'} \frac{\Theta(\epsilon_F - \lambda \hbar \omega' \sqrt{n}) - \Theta(\epsilon_F - \lambda' \hbar \omega' \sqrt{n'})}{\lambda \hbar \omega' \sqrt{n} - \lambda' \hbar \omega' \sqrt{n'} + \hbar \omega + i\delta} |\mathcal{F}_{\lambda n, \lambda' n'}(\mathbf{q})|^2, \quad (163)$$

in terms of the graphene form factors (141) and the characteristic frequency  $\omega' = \sqrt{2}v_F/l_B$  introduced in Sec. II.A.1. One notices that the first part is nothing other than a Lindhard function (Giuliani and Vignale, 2005; Mahan, 1993) for relativistic LLs filled up to the Fermi energy  $\epsilon_F = \hbar(v_F/l_B)\sqrt{2N_F}$ , which is chosen to be situated between a completely filled ( $N_F$ ) and a completely empty ( $N_F+1$ ) LL in the CB (IQHE regime). The second factor is the modulus square of the graphene form factors which plays the role of the chirality factor  $C_{\lambda, \lambda'}(\mathbf{q}', \mathbf{q} + \mathbf{q})$  in the absence of a magnetic field (Roldán *et al.*, 2009, 2010; Shizuya, 2007).<sup>20</sup>

As for the zero-field case, one may distinguish two contributions to the polarizability, one that may be viewed as a vacuum polarizability  $\Pi^{vac}(\mathbf{q}, \omega)$  and that stems from interband excitations when the Fermi level is at the Dirac point, and a second one that comes from intraband excitations in the case of doped graphene. Because undoped graphene with zero carrier density does not correspond to an IQHE situation – as we have already discussed in Sec. II.A, the zero-energy LL  $n = 0$  is only half-filled then –, we define, here, the vacuum polarizability with respect to the completely filled zero-energy level.

In order to describe more explicitly the different contributions to the polarizability, we define the auxiliary quantities (Roldán *et al.*, 2009)

$$\Pi_{\lambda n, \lambda' n'}(\mathbf{q}, \omega) = \frac{|\mathcal{F}_{\lambda n, \lambda' n'}(\mathbf{q})|^2}{\lambda \hbar v_F \sqrt{n} - \lambda' \hbar v_F \sqrt{n'} + \hbar \omega + i\delta + (\omega^+ \rightarrow -\omega^-)} \quad (164)$$

where  $\omega^+ \rightarrow \omega^-$  indicates the replacement  $\hbar \omega + i\delta \rightarrow -\hbar \omega - i\delta$  and

$$\Pi_{\lambda n}(\mathbf{q}, \omega) = \sum_{\lambda'} \sum_{n'=0}^{n-1} \Pi_{\lambda n, \lambda' n'}(\mathbf{q}, \omega) + \sum_{\lambda'} \sum_{n'=n+1}^{N_c} \Pi_{\lambda n, \lambda' n'}(\mathbf{q}, \omega) + \Pi_{\lambda n, -\lambda n}(\mathbf{q}, \omega) \quad (165)$$

<sup>20</sup> A similar expression for the polarizability has also been obtained in Refs. (Berman *et al.*, 2008; Tahir and Sabeeh, 2008) though with approximate form factors.

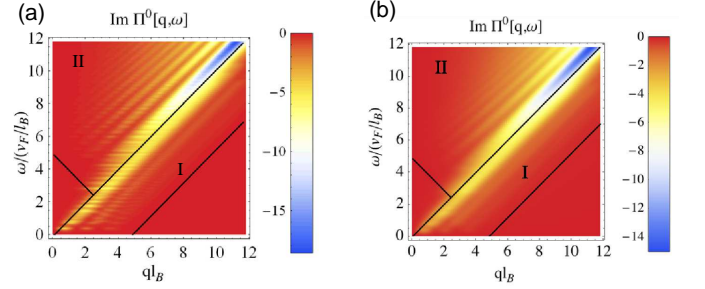


Figure 16 Particle-hole excitation spectrum for graphene in a perpendicular magnetic field. We have chosen  $N_F = 3$  in the CB and a LL broadening of  $\delta = 0.05\hbar v_F/l_B$  (a) and  $\delta = 0.2\hbar v_F/l_B$  (b). The ultraviolet cutoff is chosen such that  $N_c = 70$ .

which verify  $\Pi_{\lambda n}(\mathbf{q}, \omega) = -\Pi_{-\lambda n}(\mathbf{q}, \omega)$ . The vacuum polarization may then be defined as

$$\Pi^{vac}(\mathbf{q}, \omega) = - \sum_{n=1}^{N_c} \Pi_{+n}(\mathbf{q}, \omega) \quad (166)$$

where  $N_c$  is a cutoff that delimits the validity of the continuum approximation. Notice that, already in the absence of a magnetic field, the validity of the continuum approximation is delimited by a maximal energy  $\sim t$ . One may then introduce an upper level cutoff with the help of  $\epsilon_{N_c} = \hbar(v_F/l_B)\sqrt{2N_c} \sim t$ , that leads to  $N_c \sim 10^4/B[T]$ , which is a rather high value even for strong magnetic fields. However, due to the fact that the separation between LLs in graphene decreases with  $n$ , it is always possible to obtain reliable *semi-quantitative* results from smaller values of  $N_c$ .

The spectral function  $S(\mathbf{q}, \omega) = -\text{Im} \Pi_B^0(\mathbf{q}, \omega)/\pi$  is shown in Fig. 16 for  $N_F = 3$  and for two different values of the phenomenologically introduced LL broadening  $\delta$ . One notices first that the spectral weight is restricted to the two regions I and II corresponding to the intraband and interband particle-hole continuum, respectively, in the zero-field limit. This is not astonishing because the electron-hole pair wave vector remains a good quantum number also in the presence of a magnetic field and because the overlap between the electron and hole wave functions is largest in these regions; if one considers the pair with its overall charge neutrality, its motion is unaffected by the magnetic field. Indeed, the pair momentum

may be viewed as the sum of the pseudomomenta associated with the guiding-center variable for the electron,  $\mathbf{R} \times \mathbf{e}_z/l_B^2$ , and the hole  $-\mathbf{R}' \times \mathbf{e}_z/l_B^2$ , respectively. Each of the pseudomomenta is naturally a constant of motion because so is the guiding center, as we have discussed in Sec. II.A.1. One therefore obtains the relation

$$\mathbf{q} = \Delta\mathbf{R} \times \mathbf{e}_z/l_B^2 \quad \text{or} \quad \Delta R = |\mathbf{q}|l_B^2, \quad (167)$$

where  $\Delta\mathbf{R} = \mathbf{R} - \mathbf{R}'$  is the distance between the guiding center of the electron and that of the hole. The boundaries of the PHES in Fig. 16 may then be obtained from the decomposition (90), which yields  $\eta' - \eta \leq \Delta R \leq \eta' + \eta$ , with the help of the average values  $\eta \equiv \langle |\boldsymbol{\eta}| \rangle = l_B\sqrt{2n+1}$  and  $\eta' = l_B\sqrt{2n'+1}$ ,

$$\sqrt{2n'+1} - \sqrt{2n+1} \leq ql_B \leq \sqrt{2n'+1} + \sqrt{2n+1}. \quad (168)$$

Because the energy scales also with  $\sqrt{n}$ , one obtains the linear boundaries of the particle-hole continua as in the zero-field case mentioned above.

In contrast to these similarities with the zero-field PHES, one notices a structure in the spectral weight that is due to the strong magnetic field. As a consequence of the relativistic LL quantization, the spectral weight corresponds to inter-LL transitions at energies  $\omega = \sqrt{2}\hbar(v_F/l_B)(\sqrt{n} - \lambda\sqrt{n'})$ , where  $n > N_F$  and  $n' \leq N_F$  (for  $\lambda = +$ ) or  $n' > 0$  (for  $\lambda = -$ ). For larger values of  $N_F$ , or quite generally when increasing the energy, the level density increases due to the  $\sqrt{n}$  scaling of the LLs and the transitions. The LL structure is therefore only visible in the lower part of PHES, in the clean limit  $\delta = 0.05\hbar v_F/l_B$  [Fig. 16(a)], whereas the inter-LL transitions are blurred at larger energies or even for the lower transitions in the case of less clean samples [Fig. 16(b), for  $\delta = 0.2\hbar v_F/l_B$ ].<sup>21</sup>

In addition to the (blurred) LL structure in the PHES, one notices another structure of the spectral weight, which is organised in lines parallel to the central diagonal  $\omega = \hbar v_F|\mathbf{q}|$ . This weight is again decreased when approaching the right boundary of the intraband continuum (region I) and the left one of the interband continuum (region II), due to the above-mentioned chirality properties of electrons in graphene. The emergence of diagonal lines is a consequence of the graphene form factors (141) the modulus square of which intervenes in the polarization function. Indeed, these form factors  $\mathcal{F}_{\lambda(n+m),\lambda'n}(\mathbf{q})$  are (associated) Laguerre polynomials with  $n+1$  zeros (Gradshteyn and Ryzhik, 2000) due to the overlap between the wave function of the hole in the level  $\lambda'n$  and that of the electron in the LL  $\lambda(n+m)$  (Roldán *et al.*, 2010). These zeros in the inter-LL transitions are organised in lines that disperse parallel to the central diagonal and thus give rise to zones of vanishing spectral weight.

<sup>21</sup> The value  $\delta = 0.2\hbar v_F/l_B$  is a reasonable estimate for today's exfoliated graphene samples on an SiO<sub>2</sub> substrate (Ando, 2007a).

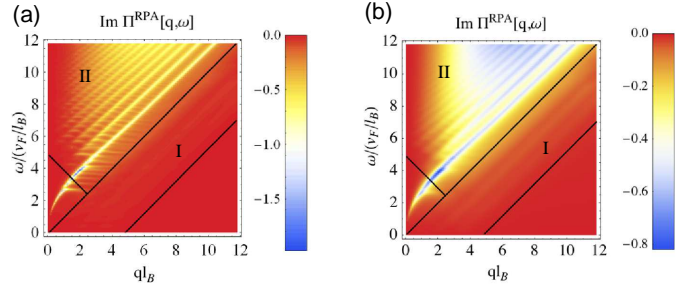


Figure 17 Particle-hole excitation spectrum for graphene in a perpendicular magnetic field. The Coulomb interaction is taken into account within the RPA. We have chosen  $N_F = 3$  in the CB and a LL broadening of  $\delta = 0.05\hbar v_F/l_B$  (a) and  $\delta = 0.2\hbar v_F/l_B$  (b). The ultraviolet cutoff is chosen such that  $N_c = 70$ .

Interestingly, it is this structure of diagonal lines that survives in more disordered samples in which the horizontal lines associated with inter-LL transitions start to overlap, i.e. once the LL spacing is smaller than the level broadening  $\delta$ .<sup>22</sup>

### 3. Electron-electron interactions in the random-phase approximation: upper-hybrid mode and linear magnetoplasmons

The PHES of non-interacting electrons in graphene gives already insight into the collective modes which one may expect once electron-electron interactions are taken into account. Indeed the regions of large spectral weight evolve into coherent collective excitations as a consequence of these interactions. Because the regions of large spectral weight are organised in lines parallel to the central diagonal  $\omega = \hbar v_F|\mathbf{q}|$ , as mentioned above, one may expect that the dominant collective excitations are roughly linearly dispersing modes instead of the more conventional weakly dispersing *magneto-excitons*, which emerge from the inter-LL transitions (Kallin and Halperin, 1984). It has though been argued that such magneto-excitons may play a role at low energies in clean samples with low doping (Iyengar *et al.*, 2007) and that they may renormalize the cyclotron energy at zero wave vector (Bychkov and Martinez, 2008).

As in the zero-field case, we take into account the Coulomb interaction within the RPA [see Eq. (160)]. The resulting spectral function is shown in Fig. 17 for the same choice of parameters as in the non-interacting case (Fig. 16). Furthermore, we have chosen a dimensionless interaction parameter  $\alpha_G = 1$ , here, which corresponds

<sup>22</sup> This behavior is in stark contrast to that of non-relativistic 2D electrons, where the LL spacing is constant and given by the cyclotron energy  $\hbar eB/m_b$ . If this quantity is larger than the level broadening  $\delta$ , there is no qualitative difference between low and high energies, and the horizontal lines associated with the inter-LL excitations (multiples of the cyclotron energy) remain well separated.

to a dielectric constant of  $\varepsilon \simeq 2$ .

One notices the prominent mode that evolves in the originally forbidden region for particle-hole excitations. This mode, which is called *upper-hybrid mode*, is the magnetic-field descendent of the 2D plasmon mode (162) and acquires a density-dependent cyclotron gap  $\omega_C = eBv_F^2/\epsilon_F = eBv_F/\hbar v_F\sqrt{\pi n_{el}}$ . Its dispersion relation in the small- $q$  limit is then given by

$$\begin{aligned}\omega_{uh}(q) &\simeq \sqrt{\omega_{pl}^2(q) + \omega_C^2} \\ &\simeq \sqrt{\frac{2\hbar e^2 v_F \sqrt{\pi n_{el}}}{\hbar^2 \varepsilon} q + \left(\frac{eBv_F^2}{\hbar v_F \sqrt{\pi n_{el}}}\right)^2},\end{aligned}\quad (169)$$

as may be shown easily within a hydrodynamic approach that has been successfully applied to the upper-hybrid mode in non-relativistic 2D electron systems (Chiu and Quinn, 1974). It is apparent from Fig. 17 that this mode remains coherent also within the region II, which corresponds to the  $B = 0$  interband particle-hole continuum.

In addition to the upper-hybrid mode, one notices linearly dispersing coherent modes in the regions I and II that emerge from the lines of large spectral weight in the non-interacting PHEs, as expected from the qualitative discussion above. We may call these modes *linear magneto-plasmons* (Roldán *et al.*, 2009, 2010) in order to distinguish them clearly from the upper-hybrid mode (169) and the weakly dispersing magneto-excitons at low doping (Iyengar *et al.*, 2007). These modes are more prominent in the interband than in the intraband region although they are also visible there. They are genuine to graphene with its characteristic  $\sqrt{Bn}$  LLs that inevitably overlap in energy, above a critical LL  $n$ , if level broadening is taken into account, and they may not be captured in the usual magneto-exciton approximation where the collective modes are adiabatically connected to the inter-LL excitations (Bychkov and Martinez, 2008; Iyengar *et al.*, 2007; Kallin and Halperin, 1984).

#### 4. Dielectric function and static screening

We terminate this section with a brief discussion of the dielectric function (161) in the static limit

$$\varepsilon^{RPA}(\mathbf{q}) \equiv \varepsilon^{RPA}(\mathbf{q}, \omega = 0) = 1 - \frac{2\pi e^2}{\varepsilon|\mathbf{q}|} \Pi^0(\mathbf{q}, \omega = 0), \quad (170)$$

by comparing the  $B \neq 0$  to the zero-field case, as shown in Fig. 18. As mentioned above, one may distinguish two separate contributions to the static polarizability, the vacuum polarizability  $\Pi^{vac}(\mathbf{q}) \equiv \Pi^{vac}(\mathbf{q}, \omega = 0)$  due to interband excitations and the intraband contribution  $\Pi^{dop}(\mathbf{q}) \equiv \Pi^{dop}(\mathbf{q}, \omega = 0)$ , which is only present in doped graphene,

$$\Pi^0(\mathbf{q}, \omega = 0) = \Pi^{vac}(\mathbf{q}) + \Pi^{dop}(\mathbf{q}). \quad (171)$$

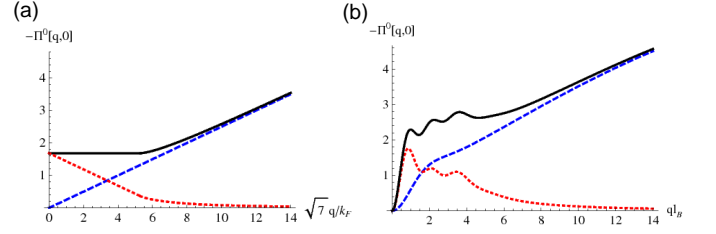


Figure 18 Static polarization function  $\Pi^0(\mathbf{q}, \omega = 0)$  for non-interacting electrons in graphene without (a) and with (b) a magnetic field. To compare both cases, we have chosen a Fermi wave vector  $q_F = \sqrt{2N_F + 1}/l_B = \sqrt{7}/l_B$  that corresponds to  $N_F = 3$ . The full black line represents the total polarizability, whereas the red dotted and the blue dashed lines show the intraband and the interband contributions, respectively. From (Roldán *et al.*, 2010).

One notices that up to  $2q_F$ , the zero-field static polarizability [Fig. 18(a)] remains constant. Indeed, the interband contribution (blue dashed line) increases linearly with the wave vector (Ando, 2006a; González *et al.*, 1999)

$$-\Pi^{vac}(\mathbf{q}) = \frac{q}{4\hbar v_F} \quad (172)$$

and thus cancels the linear decrease of the intraband contribution (red dotted line),

$$-\Pi^{dop}(|\mathbf{q}| \lesssim 2q_F) \simeq \rho(\epsilon_F) \left(1 - \frac{q}{2q_F}\right), \quad (173)$$

where

$$\rho(\epsilon_F) = \frac{\epsilon_F}{2\pi\hbar^2 v_F^2} \quad (174)$$

is the density of states per unit area at the Fermi energy. At wave vectors larger than  $2q_F$ , the intraband contribution dies out, and the polarizability is dominated by interband excitations.

With the help of these two contributions, we may rewrite the static dielectric function (170) as

$$\varepsilon^{RPA}(\mathbf{q}) = \varepsilon_\infty \left(1 + \frac{\pi\alpha_G}{2\varepsilon_\infty} \frac{\Pi^{dop}(\mathbf{q})}{\Pi^{vac}(\mathbf{q})}\right), \quad (175)$$

where we have defined

$$\varepsilon_\infty \equiv \varepsilon^{RPA}(|\mathbf{q}| \rightarrow \infty) = 1 + \frac{\pi}{2}\alpha_G, \quad (176)$$

i.e. the value that the static dielectric function approaches at large wave vectors. Notice that this is precisely the RPA result for the intrinsic dielectric constant for undoped graphene (González *et al.*, 1999). The above form of the static dielectric function may be cast into a Thomas-Fermi form,

$$\varepsilon^{TF}(\mathbf{q}) \simeq \varepsilon_\infty \left(1 + \alpha_G^* \frac{q_F}{q}\right), \quad (177)$$

in terms of the *effective coupling constant*

$$\alpha_G^* = \frac{\alpha_G}{\varepsilon_\infty} = \frac{\alpha_G}{1 + \pi\alpha_G/2}, \quad (178)$$

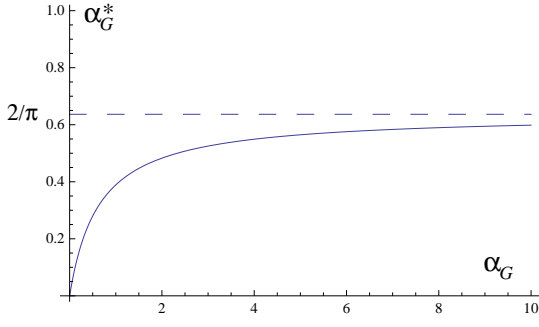


Figure 19 Effective coupling constant  $\alpha_G^*$  as a function of the bare coupling  $\alpha_G$ . The dashed line indicates the asymptotic value  $2/\pi$  obtained for large values of the bare coupling ( $r_s \gg 1$ ).

which is plotted in Fig. 19.

One notices that interband excitations yield a contribution to the dielectric constant that originally takes into account the dielectric environment in which the graphene sheet is embedded,  $\varepsilon \rightarrow \varepsilon^* = \varepsilon\varepsilon_\infty$ . This is a direct consequence of the linear behavior of the vacuum polarization (172) as a function of the wave vector and thus specific to graphene. Furthermore, one may also define an effective Thomas-Fermi wave vector  $q_{TF}^* = q_{TF}/\varepsilon_\infty = \alpha_G^*q_F$ , which describes the screening length in the presence of the vacuum polarization. As a consequence of the saturation of the effective coupling constant (178) at large values of  $\alpha_G$ , the effective Thomas-Fermi vector is thus always on the order of the Fermi wave vector unless  $\alpha_G \ll 1$ , where  $\alpha_G^* \sim \alpha_G$ . The relevant effective parameters are summarized in the table below for freestanding graphene and graphene on mainly used substrates.<sup>23</sup>

graphene	$\varepsilon$	$\alpha_G$	$\varepsilon_\infty$	$\alpha_G^*$
in vacuum	1	2.2	4.5	0.5
on SiO <sub>2</sub>	2.5	0.9	2.4	0.38
on h-BN	2.3	1	2.4	0.39
on SiC	5.5	0.4	1.6	0.25

Table I Dielectric constant  $\varepsilon$ ,  $\varepsilon_\infty$ , bare coupling  $\alpha_G$ , and effective coupling  $\alpha_G^*$  for graphene in vacuum and popular substrates.

Finally, the screened Coulomb interaction potential may be approximated as

$$v_{scr}(q) \simeq \frac{2\pi e^2}{\varepsilon\varepsilon_\infty(1 + \alpha_G^*q_F/q)q}. \quad (179)$$

One notices from this expression that processes at wave vectors  $q \ll q_F$ , where the interband excitations play a

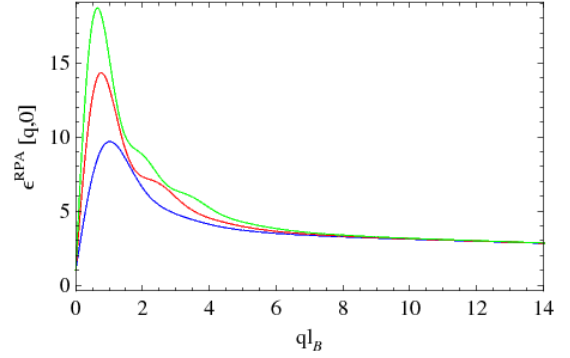


Figure 20 Static dielectric function for graphene in the IQHE regime for  $N_F = 1, 2$  and  $3$  (blue, red and green curves, in increasing order). From (Roldán *et al.*, 2010).

negligible role [see Fig. 18(a)], are still governed by the bare coupling constant  $\alpha_G \sim v_{scr}(q \ll q_F)/\hbar v_F q$ . However, processes at or above the Fermi wave vector, such as those that are relevant in the electronic transport, are characterized by the effective coupling constant  $\alpha_G^* \sim v_{scr}(q \gtrsim q_F)/\hbar v_F q$ , which saturates at a value of  $2/\pi$  as mentioned above. If we consider the value (133),  $\alpha_G \simeq 2.2$ , for the bare coupling constant of graphene in vacuum, the effective coupling is roughly four times smaller  $\alpha_G^* \simeq 0.5$ , such that the electrons in doped graphene approach the weak-coupling limit. The situation is different in undoped graphene, where recent renormalization-group (Herbut *et al.*, 2009a,b; Juričić *et al.*, 2009) and lattice gauge theoretical calculations (Drut and Lähde, 2009a,b) indicate a flow towards strong coupling at moderate values of  $\alpha_G$ .

In Fig. 18(b), we have plotted the static polarizability for graphene in the IQHE regime. Qualitatively, the result agrees with the zero-field behavior, with a (roughly) linearly increasing vacuum polarizability and a decreasing intraband contribution, apart from some superimposed oscillations due to the overlap functions that are reflected by the form factors (141). An important difference is manifest in the small wave-vector limit of the polarizability. In contrast to the zero-field case, where the polarizability saturates at a non-zero density of states, the system is gapped in the IQHE regime with a resulting vanishing density of states at the Fermi energy. This gives rise to a  $q^2$  behavior of the polarizability at small wave vectors. Furthermore, the static dielectric function, which is shown in Fig. 20 (Roldán *et al.*, 2010; Shizuya, 2007), does no longer diverge in this limit, contrary to the zero-field Thomas-Fermi result (177). Indeed, the small- $q$  behavior may be approximated as

$$\varepsilon^{RPA}(q) - 1 \propto \alpha_G N_F^{3/2} q l_B, \quad (180)$$

which is the same as for non-relativistic 2D elec-

<sup>23</sup> The dielectric constant  $\varepsilon$  is then the average of the dielectric constant of the substrate material and that of the vacuum.

trons (Aleiner and Glazman, 1995).<sup>24</sup> The maximum of the static dielectric function is obtained at  $ql_B \sim 1/q_F l_B \sim 1/\sqrt{2N_F + 1}$ , at the value  $\varepsilon_{\max} \simeq \varepsilon^{RPA}(q \sim 1/l_B \sqrt{2N_F + 1}) \sim \alpha_G N_F$ . It therefore scales as  $\varepsilon_{\max} \propto N_F$  in contrast to a  $\sqrt{N_F}$  scaling in non-relativistic 2D systems (Aleiner and Glazman, 1995). At large wave vectors, the static dielectric function saturates at the same value  $\varepsilon_\infty$  as in zero magnetic field.

#### IV. MAGNETO-PHONON RESONANCE IN GRAPHENE

In the previous section, we have discussed the role of electron-electron interactions in the IQHE regime, where a perturbative (diagrammatic) approach may be applied. Similarly, one may treat the electron-phonon interaction in a perturbative manner in this regime. This is the subject of the present section, before discussing again electron-electron interactions in the strong coupling limit of partially filled LLs (Sec. V).

As a consequence of the honeycomb-lattice structure of graphene, with two inequivalent sublattices, there are four in-plane phonons, two acoustic and two optical ones. Each phonon type occurs in a longitudinal (longitudinal acoustic, LA, and longitudinal optical, LO) and a transverse (transverse acoustic, TA, and transverse optical, TO) mode. In addition to these four phonons, one finds two out-of-plane phonons, one acoustic (ZA) and one optical (ZO) [for a review of phonons in graphene, see Refs. (Saito *et al.*, 1998) and (Wirtz and Rubio, 2004)]. Here, we concentrate on the in-plane optical phonons LO and TO, which couple to the electronic degrees of freedom. More specifically, we discuss these phonons at the  $\Gamma$  point ( $E_{2g}$  modes) in the center of the first BZ, which are attributed to the G-band at  $\hbar\omega_{ph} \simeq 0.2$  eV in the Raman spectra [see e.g. Refs. (Ferrari *et al.*, 2006; Graf *et al.*, 2007; Gupta *et al.*, 2006; Pisana *et al.*, 2007; Yan *et al.*, 2007)].

One of the most prominent effects of electron-phonon coupling in metals and semiconductors is the so-called Kohn anomaly (Kohn, 1959), which consists of a singularity in the phonon dispersion due to a singularity in the electronic density-density response function. The analog of the Kohn anomaly in graphene yields a logarithmic divergence of the phonon frequency when the bare phonon frequency coincides with twice the Fermi energy (Ando, 2006b; Castro Neto and Guinea, 2007; Lazzeri and Mauri, 2006). We investigate how this renormalization manifests itself in graphene in a strong magnetic field (Ando, 2007b; Goerbig *et al.*, 2007). In Sec. IV.A, we consider the specific form of the electron-phonon coupling and discuss its consequences for the

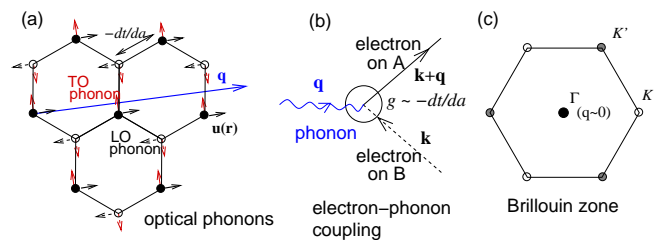


Figure 21 Electron-phonon coupling in graphene. (a) Optical phonons in graphene, with a wave vector  $\mathbf{q}$  in the vicinity of the  $\Gamma$  point at the center of the first BZ [see part (c)]. The amplitude of the LO phonon is in the direction of propagation (black arrows), that of the TO phonon perpendicular (red arrows). The optical phonons modify the bond lengths of the honeycomb lattice. (b) As a consequence of the modified bond lengths, the electronic hopping is varied, and the electron-phonon coupling is off-diagonal in the sublattice index.

renormalization of the optical phonons at the  $\Gamma$  point in Sec. IV.B. More specifically, we consider both non-resonant (Sec. IV.B.1) and resonant coupling (Sec. IV.B.2), the latter being specific to graphene in a magnetic field when the phonon is in resonance with an allowed inter-LL transition (*magneto-phonon resonance*) (Goerbig *et al.*, 2007).

##### A. Electron-Phonon Coupling

The LO and TO phonons in graphene are schematically represented in Fig. 21(a). As already mentioned above, we concentrate on phonons at small wave vectors, in the vicinity of the  $\Gamma$  point. The origin of the electron-phonon coupling may easily be understood from the variation of the bond length caused by the phonon, which affects the electronic hopping amplitude between  $nm$  carbon atoms. As we have discussed in Sec. I.D, the effect may be quantified with the help of Harrison's law (Harrison, 1981), which yields  $\partial t/\partial a \simeq -4.3$  eV/Å [see Eq. (57)]. The order of magnitude for the bare electron-phonon energy is then obtained by multiplying this variation with the typical length scale  $\sqrt{\hbar/M\omega_{ph}}$ , which characterizes the amplitude of a lattice vibration of frequency  $\omega_{ph}$  within the harmonic approximation. The intervening mass  $M$  is that of the carbon atom. Indeed, a tight-binding calculation (Ando, 2006b; Ishikawa and Ando, 2006) corroborates this argument, apart from a numerical prefactor  $3/2$ , and yields a bare electron-phonon coupling

$$g = -\frac{3}{2} \frac{\partial t}{\partial a} \sqrt{\frac{\hbar}{M\omega_{ph}}} \simeq 0.26 \text{ eV}. \quad (181)$$

This value agrees well with ab-initio calculations (Piscanec *et al.*, 2004), although it is though slightly lower than the value determined experimentally, which ranges from  $g \simeq 0.3$  eV (Faugeras *et al.*, 2009; Pisana *et al.*, 2007) to  $g \simeq 0.36$  eV (Yan *et al.*, 2007).

Furthermore, one notices that, because the electron-phonon coupling is mediated by a bond variation between

<sup>24</sup> Notice, however, that the expression becomes exact only in the large- $N_F$  limit and that in non-relativistic 2D electron systems, the coupling constant  $r_s$  also depends on  $N_F$ ,  $r_s \sim N_F^{-1/2}$ .

sites that belong to two different sublattices, the coupling constant is *off-diagonal* in the sublattice basis. This is diagrammatically depicted in Fig. 21(b).

### 1. Coupling Hamiltonian

The above considerations help us to understand the different terms in the Hamiltonian,

$$H = H_{el} + H_{ph} + H_{coupl}$$

which serves as the basis for the analysis of the electron-phonon coupling. The Hamiltonian for 2D electrons in a magnetic field,

$$\begin{aligned} H_{el} &= \sum_{\xi} \int d^2r \psi_{\xi}^{\dagger}(\mathbf{r}) \mathcal{H}_B^{\text{eff},\xi} \psi_{\xi}(\mathbf{r}) \\ &= \sum_{\lambda n, m; \xi} \epsilon_{\lambda, n} c_{\lambda n, m; \xi}^{\dagger} c_{\lambda n, m; \xi} \end{aligned} \quad (182)$$

may be written, in second quantization, in terms of the one-particle Hamiltonian (75) and the fermionic fields

$$\psi_{\xi}(\mathbf{r}) = \sum_{\lambda n, m} \psi_{\lambda n, m; \xi}(\mathbf{r}) c_{\lambda n, m; \xi},$$

where  $\psi_{\lambda n, m; \xi}(\mathbf{r})$  is the wave function in position space associated with the spinor (138).

The lattice vibration is characterized by the relative displacement  $\mathbf{u}(\mathbf{r})$  between the two sublattices, which may be decomposed in terms of the bosonic operators  $b_{\mu, \mathbf{q}}$  and  $b_{\mu, \mathbf{q}}^{\dagger}$ ,

$$\mathbf{u}(\mathbf{r}) = \sum_{\mu, \mathbf{q}} \sqrt{\frac{\hbar}{2N_{uc}M\omega_{\mu}(\mathbf{q})}} \left( b_{\mu, \mathbf{q}} + b_{\mu, -\mathbf{q}}^{\dagger} \right) \mathbf{e}_{\mu, \mathbf{q}} e^{-i\mathbf{q}\cdot\mathbf{r}}, \quad (183)$$

where  $\mathbf{e}_{\mu, \mathbf{q}}$  denotes the two possible linear polarizations ( $\mu = \text{LO, TO}$ ) at the wave vector  $\mathbf{q}$  and  $N_{uc} = \mathcal{A}/(3\sqrt{3}a^2/2)$  is the number of unit cells in the system. The phonon Hamiltonian then reads, on the level of the harmonic approximation,

$$H_{ph} = \sum_{\mu, \mathbf{q}} \hbar\omega_{\mu}(\mathbf{q}) b_{\mu, \mathbf{q}}^{\dagger} b_{\mu, \mathbf{q}}, \quad (184)$$

in terms of the phonon dispersion  $\omega_{\mu}(\mathbf{q})$ . Notice that, at the  $\Gamma$  point, the frequencies of the LO and TO phonons coincide, and one has  $\omega_{ph} \equiv \omega_{\mu}(\mathbf{q} = 0)$ . It is then convenient to describe the phonon modes in terms of circularly polarized modes,  $u_{\odot}(\mathbf{r}) = [u_x(\mathbf{r}) + iu_y(\mathbf{r})]/\sqrt{2}$  and  $u_{\ominus}(\mathbf{r}) = u_{\odot}^*(\mathbf{r})$ .

Finally, taking into account the above considerations on the electron-phonon coupling, the coupling Hamiltonian reads (Ando, 2006b; Castro Neto and Guinea, 2007; Ishikawa and Ando, 2006)

$$H_{coupl} = g \sqrt{\frac{2M\omega_{ph}}{\hbar}} \sum_{\xi} \int d^2r \psi_{\xi}^{\dagger}(\mathbf{r}) [\boldsymbol{\sigma} \wedge \mathbf{u}(\mathbf{r})] \psi_{\xi}(\mathbf{r}), \quad (185)$$

where  $\boldsymbol{\sigma} \wedge \mathbf{u}(\mathbf{r}) = [\boldsymbol{\sigma} \times \mathbf{u}(\mathbf{r})]_z = \sigma^x u_y(\mathbf{r}) - \sigma^y u_x(\mathbf{r})$  is the 2D cross product between the Pauli matrices and the displacement field.

### 2. Hamiltonian in terms of magneto-exciton operators

As a consequence of the off-diagonal character of the electron-phonon coupling (185), one notices that the intervening matrix elements are proportional to  $\delta_{n, n\pm 1}$ , and one thus obtains the selection rules

$$\lambda n \rightarrow \lambda'(n \pm 1), \quad (186)$$

in analogy with the magneto-optical selection rules discussed in Sec. II.A.1. Furthermore, if we fix the energy of the dipole transition (105) to be<sup>25</sup>  $\Delta_n \equiv \Delta_{n, \lambda=-} = \sqrt{2}\hbar(v_F/l_B)(\sqrt{n+1} + \sqrt{n})$ , there are two possible transitions, which may be distinguished by the circular polarization of the phonon they are coupled to. Indeed, the form of the electron-phonon coupling (185) indicates that the  $\odot$ -polarized phonon is coupled to the transition  $-(n+1) \rightarrow +n$ , whereas the  $\ominus$ -polarized phonon couples to the  $-n \rightarrow +(n+1)$  interband transition (Goerbig *et al.*, 2007).

It is then convenient to introduce *magneto-exciton* operators, associated with the above-mentioned inter-LL transitions

$$\begin{aligned} \phi_{\odot}^{\dagger}(n, \xi) &= \frac{i\sqrt{1+\delta_{n,0}}}{\mathcal{N}_n^{\odot}} \sum_m c_{+n, m; \xi}^{\dagger} c_{-(n+1), m; \xi}, \\ \phi_{\ominus}^{\dagger}(n, \xi) &= \frac{i\sqrt{1+\delta_{n,0}}}{\mathcal{N}_n^{\ominus}} \sum_m c_{+(n+1), m; \xi}^{\dagger} c_{-n, m; \xi}, \end{aligned} \quad (187)$$

where the index  $\mathcal{A} = \odot, \ominus$  characterizes the angular momentum of the excitation and where the normalization factors

$$\begin{aligned} \mathcal{N}_n^{\odot} &= \sqrt{2(1+\delta_{n,0})N_B [\bar{\nu}_{-(n+1)} - \bar{\nu}_{+n}]} \\ \text{and } \mathcal{N}_n^{\ominus} &= \sqrt{2(1+\delta_{n,0})N_B [\bar{\nu}_{-n} - \bar{\nu}_{+(n+1)}]} \end{aligned}$$

are used to ensure the bosonic commutation relations of the exciton operators,  $[\phi_{\mathcal{A}}(n, \xi), \phi_{\mathcal{A}'}^{\dagger}(n', \xi')] = \delta_{\mathcal{A}, \mathcal{A}'} \delta_{\xi, \xi'} \delta_{n, n'}$ , including the two-fold spin degeneracy. These commutation relations are obtained within the mean-field approximation with  $\langle c_{\lambda n, m; \xi}^{\dagger} c_{\lambda' n', m'; \xi'} \rangle = \delta_{\xi, \xi'} \delta_{\lambda, \lambda'} \delta_{n, n'} \delta_{m, m'} (\delta_{\lambda, -} + \delta_{\lambda, +} \bar{\nu}_{\lambda n})$ , where  $0 \leq \bar{\nu}_{\lambda n} \leq 1$  is the partial filling factor of the  $n$ -th LL, normalized to 1.

One notices that the magneto-exciton operators are, apart from a normalization constant, nothing other

<sup>25</sup> We consider mainly interband transitions here, which may have a chance to be in resonance with the phonon of energy  $\hbar\omega_{ph} \sim 0.2$  eV.



than the reduced density operators (140),  $\phi_{\zeta}^{\dagger}(n, \xi) \propto \bar{\rho}_{+n, -(n+1)}^{\xi, \xi}(\mathbf{q} = 0)$  and  $\phi_{\zeta}^{\dagger}(n, \xi) \propto \bar{\rho}_{+(n+1), -n}^{\xi, \xi}(\mathbf{q} = 0)$ , respectively, at zero wave vector. Notice furthermore that, because of the relative sign  $\xi$  between the kinetic part (182) and the electron-phonon coupling Hamiltonian (185), the optical phonons couple to the *valley-anti-symmetric* magneto-exciton combination  $\phi_{\mathcal{A}, as}(n) = [\phi_{\mathcal{A}}(n, \xi = +) - \phi_{\mathcal{A}}(n, \xi = -)]/\sqrt{2}$ . This needs to be contrasted to the magneto-optical coupling (Abergel and Fal'ko, 2007; Iyengar *et al.*, 2007; Sadowski *et al.*, 2006), where the photon couples to the *valley-symmetric* mode  $\phi_{\mathcal{A}, s}(n) = [\phi_{\mathcal{A}}(n, \xi = +) + \phi_{\mathcal{A}}(n, \xi = -)]/\sqrt{2}$ .

The magneto-exciton operators (187) allow one to rewrite the electron-phonon Hamiltonian at the  $\Gamma$  point ( $\mathbf{q} = 0$ ) in a bosonic form as (Goerbig *et al.*, 2007)

$$H = \sum_{\tau=s, as} \sum_{\mathcal{A}, n} \Delta_n \phi_{\mathcal{A}, \tau}^{\dagger}(n) \phi_{\mathcal{A}, \tau}(n) + \sum_{\mathcal{A}} \hbar \omega_{ph} b_{\mathcal{A}}^{\dagger} b_{\mathcal{A}} + \sum_{\mathcal{A}, n} g_{\mathcal{A}}(n) \left[ b_{\mathcal{A}}^{\dagger} \phi_{\mathcal{A}, as}(n) + b_{\mathcal{A}} \phi_{\mathcal{A}, as}^{\dagger}(n) \right], \quad (188)$$

in terms of the *effective coupling constants*

$$g_{\zeta}(n) = g \sqrt{(1 + \delta_{n,0}) \gamma \sqrt{\bar{\nu}_{-(n+1)} - \bar{\nu}_{+n}}},$$

$$\text{and } g_{\zeta}(n) = g \sqrt{(1 + \delta_{n,0}) \gamma \sqrt{\bar{\nu}_{-n} - \bar{\nu}_{+(n+1)}}}, \quad (189)$$

with the constant  $\gamma \equiv 3\sqrt{3}a^2/2\pi l_B^2$ . One therefore remarks that, although the bare coupling constant  $g$  is rather large [see Eq. (181)], the effective coupling is reduced by a factor of  $a/l_B$ ,

$$g_{\mathcal{A}}(n) \sim g \frac{a}{l_B} \sim 1 \dots 2 \text{ meV} \sqrt{B[\text{T}]}. \quad (190)$$

## B. Phonon Renormalization and Raman Spectroscopy

The Hamiltonian (188) shows that a phonon may be destroyed by exciting a magneto-exciton, and the associated Dyson equation for the dressed phonon propagator  $D(\omega)$  reads

$$D_{\mathcal{A}}(\omega) = D_0(\omega) + D_0(\omega) \chi_{\mathcal{A}}(\omega) D_{\mathcal{A}}(\omega), \quad (191)$$

in terms of the bare bosonic phonon propagator

$$D_0(\omega) = \frac{1}{\hbar} \frac{2\omega}{\omega^2 - \omega_{ph}^2} \quad (192)$$

and

$$\chi_{\mathcal{A}}(\omega) = \sum_{n=N_F+1}^{N_c} \frac{2\Delta_n g_{\mathcal{A}}^2(n)}{\hbar^2 \omega^2 - \Delta_n^2} + \frac{2\tilde{\Delta}_{N_F} g_{\mathcal{A}}^2(n)}{\hbar^2 \omega^2 - \tilde{\Delta}_{N_F}^2}. \quad (193)$$

The form of the last expression is transparent; the magneto-exciton is a boson, and its propagator is therefore of the same form as that of the bare phonon. It

is equivalent to a particle-hole propagation associated with a polarization bubble [see Fig. 15(a)], but the expression (193) also takes into account the square of the effective coupling constant which is due to the double occurrence of the electron-phonon coupling – first when the phonon is converted into a magneto-exciton and the second time when the magneto-exciton is destroyed by creating a phonon. The last term in Eq. (193) takes into account the (only) possible intra-band magneto-exciton from the last filled LL  $N_F$  to  $N_F + 1$  with energy  $\tilde{\Delta}_{N_F} = \sqrt{2}(\hbar v_F/l_B)(\sqrt{N_F+1} - \sqrt{N_F})$ , which we have omitted in the Hamiltonian (188) because it is irrelevant for resonant coupling. The parameter  $N_c$  is the same high-energy cutoff, defined by  $\epsilon_{N_c} = \hbar(v_F/l_B)\sqrt{2N_c} \sim t$ , as in Sec. III.B of the preceding chapter.

The renormalized phonon frequencies  $\tilde{\omega}_{\mathcal{A}}$  may be obtained from the Dyson equation (191), by searching the poles of the dressed phonon propagator

$$D_{\mathcal{A}}(\omega)^{-1} = 0 = D_{\mathcal{A}}(\tilde{\omega}_{\mathcal{A}})^{-1} - \chi_{\mathcal{A}}(\tilde{\omega}_{\mathcal{A}}), \quad (194)$$

and one finds (Ando, 2007b; Goerbig *et al.*, 2007)

$$\tilde{\omega}_{\mathcal{A}}^2 - \omega_{ph}^2 = \frac{4\omega_{ph}}{\hbar} \left[ \sum_{n=N_F+1}^{N_c} \frac{\Delta_n g_{\mathcal{A}}^2(n)}{\hbar^2 \tilde{\omega}_{\mathcal{A}}^2 - \Delta_n^2} + \frac{\tilde{\Delta}_{N_F} g_{\mathcal{A}}^2(N_F)}{\hbar^2 \tilde{\omega}_{\mathcal{A}}^2 - \tilde{\Delta}_{N_F}^2} \right]. \quad (195)$$

### 1. Non-resonant coupling and Kohn anomaly

Before discussing resonant coupling, i.e. when the phonon frequency is in resonance with a possible inter-LL excitation, in a strong magnetic field, we comment on the relation between Eq. (195) and the (non-resonant) renormalization of the phonon frequency in zero magnetic field. The zero-field limit may indeed be obtained from Eq. (195) if one replaces the sum  $\sum_n$  by an integral  $\int dn$ , i.e. if the spacing between the LLs vanishes,  $\tilde{\Delta}_{N_F} \rightarrow 0$ . Linearizing Eq. (195), if one replaces  $\tilde{\omega}_{\mathcal{A}} \rightarrow \omega_{ph}$  in the denominators, and using the approximation  $\sqrt{n} + \sqrt{n+1} \approx 2\sqrt{n}$  yields

$$\tilde{\omega} \simeq \tilde{\omega}_0 + \tilde{\lambda} \left[ \sqrt{2N_F} \frac{v_F}{l_B} - \frac{\omega_{ph}}{4} \ln \left( \frac{\omega_{ph} + 2\sqrt{2N_F} v_F/l_B}{\omega_{ph} - 2\sqrt{2N_F} v_F/l_B} \right) \right], \quad (196)$$

where  $\tilde{\lambda} = (2/\sqrt{3}\pi)(g/t)^2 \simeq 3.3 \times 10^{-3}$  is the dimensionless electron-phonon coupling constant introduced in Refs. (Ando, 2006b, 2007b), and

$$\tilde{\omega}_0 \simeq \omega_{ph} + \frac{2}{\hbar} \int_0^{N_c} dn \frac{\Delta_n g_{\mathcal{A}}^2(n)}{\hbar^2 \omega_{ph}^2 - \Delta_n^2} \quad (197)$$

is the physical phonon frequency at zero doping. Indeed, the frequency  $\omega_{ph}$  is not relevant in a physical measurement in graphene even if it occurs in the Hamiltonian, but one measures  $\tilde{\omega}_0$  at zero doping and  $B = 0$ . Equation (196) coincides precisely with the zero-field result (Ando, 2006b; Castro Neto and Guinea,

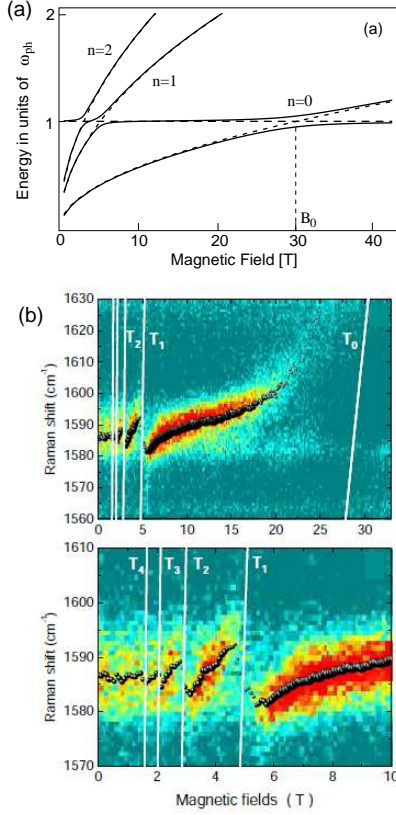


Figure 22 (a) From Ref. (Goerbig *et al.*, 2007). Anticrossing of coupled phonon-magneto-exciton modes as a function of the magnetic field. (b) From Ref. (Faugeras *et al.*, 2009). Colour plot of the Raman spectra as a function of the magnetic field. The continuous white lines indicate the magnetic field for which the phonon is in resonance with an inter-LL excitation of energy  $\Delta_n$ . *Top*: data of the full  $B$ -field range. *Bottom*: zoom on the range from 0 to 10 T.

2007; Lazzeri and Mauri, 2006) if one identifies the chemical potential with the energy of the last filled LL,  $\mu = \sqrt{2N_F} \hbar v_F / l_B$  (Goerbig *et al.*, 2007).

## 2. Resonant coupling

Apart from the non-resonant coupling discussed in the preceding section, the high-field electron-phonon coupling reveals a linear effect when the phonon is in resonance with a particular magneto-exciton,  $\hbar\omega_{ph} \simeq \Delta_n$ . In this case, the sum on the right-hand side in Eq. (195) is dominated by a single term and may be approximated by  $2(\omega_{ph}/\hbar)g_A^2(n)/(\hbar\tilde{\omega}_A - \Delta_n)$ . This results in a fine structure of mixed phonon-magneto-exciton modes,  $\phi_{A,as}(n)\cos\theta + b_A\sin\theta$  with frequency  $\tilde{\omega}_A^+$  and  $\phi_{A,as}(n)\sin\theta - b_A\cos\theta$  with frequency  $\tilde{\omega}_A^-$  [where  $\cot 2\theta = (\Delta_n - \hbar\tilde{\omega}_0)/2g_A$ ]. The frequencies of these mixed

boson modes read (Ando, 2007b; Goerbig *et al.*, 2007)

$$\tilde{\omega}_A^\pm(n) = \frac{1}{2} \left( \frac{\Delta_n}{\hbar} + \tilde{\omega}_0 \right) \mp \sqrt{\frac{1}{4} \left( \frac{\Delta_n}{\hbar} - \tilde{\omega}_0 \right)^2 + g_A^2(n)}, \quad (198)$$

and the resulting phonon-magneto-exciton anticrossing is depicted in Fig. 22(a).

The above-mentioned anticrossing of the coupled phonon-magneto-exciton modes has been observed in recent Raman experiments on epitaxial graphene. Remember that Raman spectroscopy is sensitive to the phonon component of the mixed modes (Faugeras *et al.*, 2009). The results are shown in Fig. 22(b) and corroborate the theoretically expected behavior (Ando, 2007b; Goerbig *et al.*, 2007). Indeed, one may obtain the oscillating behavior from a numerical solution of Eq. (195) if one expresses the equation in terms of  $\tilde{\omega}_0$  instead of  $\omega_{ph}$  and if one takes into account a finite broadening of the levels. If the phonon is out of resonance with an inter-LL transition, its frequency is essentially field-independent and coincides with the energy of the  $E_{2g}$  line at  $1586 \text{ cm}^{-1} \simeq 0.2 \text{ eV}$ . When it approaches the resonance (by increasing the magnetic field), its energy is shifted upwards as a consequence of the anticrossing but rapidly dies out in intensity once the magneto-exciton component becomes dominant in the  $\tilde{\omega}_A^+$  mode. Upon further increase of the magnetic field, the  $\tilde{\omega}_A^-$  mode becomes more phonon-like and therefore visible in the Raman spectra.

The fine structure of the high-field resonant electron-phonon coupling may furthermore be investigated by sweeping the chemical potential when the magnetic field is held fixed at resonance. The effect is most pronounced for the resonance  $\hbar\omega_{ph} \simeq \Delta_{n=0}$ , which is expected at  $B \simeq 30 \text{ T}$  [see Fig. 22(a)]. In this case, the mode consists of an equal-weight superposition of the phonon and the magneto-exciton ( $\cos\theta = \sin\theta = 1/\sqrt{2}$ ), and the  $E_{2g}$  band would appear as two lines, at the energies  $\hbar\tilde{\omega}^\pm = \hbar\tilde{\omega}_0 \pm g_A$ , for the case of undoped graphene.<sup>26</sup> With the above estimation (181) for the bare electron-phonon coupling constant, one obtains for the line splitting  $2g_A \sim 16 \text{ meV}$  ( $\sim 130 \text{ cm}^{-1}$ ), which largely exceeds the G-band width observed in Refs. (Ferrari *et al.*, 2006; Graf *et al.*, 2007; Gupta *et al.*, 2006; Pisana *et al.*, 2007; Yan *et al.*, 2007).

It is apparent from the expressions (190) for the effective coupling constants  $g_\circ$  and  $g_\ominus$  that the splitting may be controlled by the LL filling factor. Exactly at zero doping, both coupling constants coincide,  $g_\circ = g_\ominus$ , but upon electron doping the transition  $-1 \rightarrow 0$  associated with the  $\circ$ -polarization becomes weaker due to the reduced number of final states in  $n = 0$ , whereas the  $0 \rightarrow +1$  transition (with polarization  $\ominus$ ) is strengthened.

<sup>26</sup> Notice, however, that only an oscillation of the phonon mode, and not a splitting, has been observed in the experiment by Faugeras *et al.* (Faugeras *et al.*, 2009).

As a consequence, the associated coupling constants are increased and decreased, respectively, until the coupling constant  $g_{\odot}$  vanishes at  $\nu = 2$ .

The above-mentioned filling-factor dependence has a direct impact on the Raman lines (Goerbig *et al.*, 2007). Whereas at  $\nu = 0$ , one expects two lines separated by the energy  $2g_{\odot} = 2g_{\ominus}$ , the degeneracy in the circular polarization is lifted between  $0 < \nu < 2$ .<sup>27</sup> One therefore expects to observe four lines instead of two, where the inner ones are associated with the polarization  $\ominus$ , whereas the outer ones with increased splitting correspond to the opposite polarization  $\odot$ . The separation between the inner lines vanishes then at  $\nu = 2$ , where the splitting of the outer lines is maximal and where one expects to observe three lines.

## V. ELECTRONIC CORRELATIONS IN PARTIALLY FILLED LANDAU LEVELS

This last section is devoted to the physics of interacting electrons in the strong-correlation limit of a partially filled LL. The motivation stems from non-relativistic quantum Hall systems in GaAs heterostructures, where these correlations lead to the formation of incompressible quantum-liquid phases, which display the fractional quantum Hall effect (FQHE) (Tsui *et al.*, 1982), as well as of exotic electron-solid phases, such as the high-field Wigner crystal (Andrei *et al.*, 1988; Williams *et al.*, 1991) or the theoretically predicted bubble and stripe phases (Fogler *et al.*, 1996; Koulakov *et al.*, 1996; Moessner and Chalker, 1996). The latter are likely to be at the origin of highly anisotropic transport properties at half-filled higher LLs (Du *et al.*, 1999; Lilly *et al.*, 1999), particular electron transport under microwave irradiation (Lewis *et al.*, 2005, 2004, 2002), and an intriguing reentrance of the IQHE in  $n = 1$  and  $n = 2$  (Cooper *et al.*, 1999; Eisenstein *et al.*, 2002).

It is therefore natural to ask whether such strongly-correlated phases exist also in graphene and if so what the differences are with respect to non-relativistic 2D electrons. Moreover, the fact that the electrons reside at the surface opens up the possibility to probe these phases by spectroscopic means, such as scanning tunneling spectroscopy, which has already been applied successfully in the analysis of the electron density distribution of exfoliated (Martin *et al.*, 2008) and epitaxial graphene (Mallet *et al.*, 2007), as well as graphene on graphite substrates (Li *et al.*, 2009b).

After a short discussion of the Coulomb interaction in graphene as compared to non-relativistic 2D electrons, we introduce the basic model of interacting electrons

in a partially filled relativistic LL (Sec. V.A). This model yields a qualitative understanding of the above-mentioned correlated electronic phases in the context of graphene, as compared to non-relativistic electrons. In Sec. V.B, we apply this model to the quantum Hall ferromagnetism with an internal SU(4) symmetry that is the relevant symmetry in graphene LLs and discuss its relation with the experimentally observed degeneracy lifting of the zero-energy LL  $n = 0$  (Zhang *et al.*, 2006). We terminate this section with a review of the specific FQHE in graphene (Sec. V.C), which has recently been observed in the two-terminal (Bolotin *et al.*, 2009; Du *et al.*, 2009) as well as in the four-terminal geometry (Dean *et al.*, 2011; Ghahari *et al.*, 2011).

### A. Electrons in a Single Relativistic Landau Level

Quite generally, the origin of strongly-correlated electron phases is a quenched kinetic energy, where the partially filled LL is separated by the cyclotron gap from the neighboring ones such that inter-LL excitations constitute high-energy degrees of freedom. The Coulomb interaction, which may though be small with respect to the cyclotron gap, remains then as the only relevant energy scale which dominates the low-energy degrees of freedom if we can neglect disorder effects. This leads to the seemingly counter-intuitive finding of strongly-correlated phases in weakly-correlated matter.

In order to quantify the degree of separation between the energy scales, one may use a similar argument as the one that led us to the definition of the dimensionless interaction parameter (131), introduced at the beginning of Sec. III. Indeed, one needs to compare the Coulomb interaction energy  $E_{int} = e^2/\varepsilon R_C$  at the characteristic length scale  $R_C = l_B\sqrt{2n+1}$  to the LL spacing  $\hbar\omega_C = \hbar eB/m_b$ , where we concentrate on non-relativistic electrons first,

$$r_s^B = \frac{e^2}{\hbar\varepsilon v_F(n, B)}, \quad \text{with} \quad v_F(n, B) \equiv R_C\omega_C. \quad (199)$$

If one identifies the Fermi wave vector  $k_F \simeq \sqrt{2n}/l_B$ , one obtains the same expression as for the zero-field coupling constant (132),

$$r_s^B = r_s = \frac{m_b e^2}{\hbar^2 \varepsilon} k_F^{-1} \sim \frac{1}{a_0^* k_F}. \quad (200)$$

This means that the degree of LL mixing is still governed by  $r_s$ , and the inter-LL excitations are well separated from the low-energy intra-LL degrees of freedom unless  $r_s$  becomes very large. Notice, however, that  $r_s \sim 1$  in most 2D electron systems.

In the case of partially filled relativistic LLs in graphene, one is tempted to apply the same argument – if the Coulomb interaction  $e^2/\varepsilon R_C$  is sufficiently small as compared to the LL spacing  $\tilde{\Delta}_n$ , the relevant degrees of freedom are those which couple quantum states in the

<sup>27</sup> We present the argument for a Fermi energy in the CB, i.e.  $\nu > 0$ , but the situation is generic, and the argument also applies in the VB if one interchanges the polarizations.

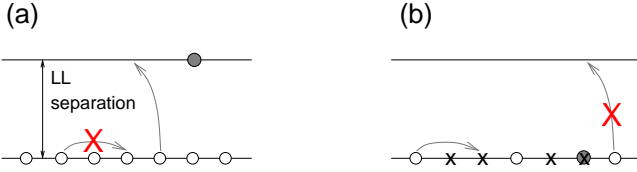


Figure 23 (a) Completely filled topmost LL. Due to the Pauli principle, the only possible excitations are inter-LL transitions. (b) Partially filled LL. For sufficiently small values of  $r_s$  (or  $\alpha_G$ ), the inter-LL excitations constitute high-energy degrees of freedom that may be omitted at low energies, where the relevant degrees couple states within the same LL.

same LL, whereas inter-LL excitations may be considered as frozen out (see Fig. 23). Although this seems a reasonable assumption for the lowest LLs, one is confronted with the apparent problem that the LL spacing rapidly decreases once the Fermi level resides in higher LLs,

$$\tilde{\Delta}_n = \sqrt{2} \frac{\hbar v_F}{l_B} (\sqrt{n+1} - \sqrt{n}) \simeq \frac{\hbar v_F}{l_B \sqrt{2n}}. \quad (201)$$

Notice, however, that this decrease is balanced by the  $1/\sqrt{2n}$  scaling of the characteristic Coulomb interaction, such that even in higher LLs the separation between low- and high-energy degrees of freedom is governed by the dimensionless coupling constant

$$\alpha_G^B = \frac{e^2/\varepsilon l_B \sqrt{2n}}{\hbar v_F/l_B \sqrt{2n}} = \frac{e^2}{\hbar \varepsilon v_F} = \alpha_G, \quad (202)$$

which coincides with the scale-invariant zero-field coupling constant (133). From the interaction point of view, the restriction of the electron dynamics to a single partially filled LL in the large- $n$  limit is therefore as justified as for the lowest relativistic LLs. Naturally, this statement only holds true in the absence of disorder that induces stronger LL mixing for  $n \gg 1$  than in  $n = 0$  or  $\pm 1$ .

### 1. SU(4)-symmetric model

Formally, the above-mentioned separation into high- and low-energy degrees of freedom may be realized with the help of the reduced density operators (140). For the moment, we only consider the case where  $\xi = \xi'$ , i.e. we concentrate on the valley-symmetric model, in which case the reduced (intra-valley) density operators (153) fall into two distinct classes: for  $n \neq n'$  or  $\lambda \neq \lambda'$ , the operators  $\bar{\rho}_{\lambda n, \lambda' n'}(\mathbf{q})$  describe density fluctuations corresponding to inter-LL transitions of an energy equal to or larger than the LL separation  $\tilde{\Delta}_n$ , whereas the *projected density operators*

$$\begin{aligned} \bar{\rho}(\mathbf{q}) &\equiv \bar{\rho}_{\lambda n, \lambda n}(\mathbf{q}) \\ &= \sum_{\xi=\pm} \sum_{\sigma=\uparrow, \downarrow} \sum_{m, m'} \langle m | e^{-i\mathbf{q}\cdot\mathbf{R}} | m' \rangle c_{\lambda n, m; \xi, \sigma}^\dagger c_{\lambda n, m'; \xi, \sigma} \end{aligned} \quad (203)$$

describe the density fluctuations inside the LL  $\lambda n$  that interest us here. Notice that we have dropped the index  $\lambda n$  in the definition of the projected density operators; they satisfy the quantum-mechanical commutation relations (Girvin *et al.*, 1986)

$$[\bar{\rho}(\mathbf{q}), \bar{\rho}(\mathbf{q}')] = 2i \sin\left(\frac{\mathbf{q}' \wedge \mathbf{q} l_B^2}{2}\right) \bar{\rho}(\mathbf{q} + \mathbf{q}'), \quad (204)$$

where  $\mathbf{q}' \wedge \mathbf{q} = (\mathbf{q}' \times \mathbf{q})_z = q'_x q_y - q'_y q_x$  is the 2D vector product between  $\mathbf{q}'$  and  $\mathbf{q}$ , and these commutation relations are *independent* of the LL index  $\lambda n$ . The information about the LL is indeed waved to the effective interaction potential

$$v_n(\mathbf{q}) = \frac{2\pi e^2}{\varepsilon q} [\mathcal{F}_n(\mathbf{q})]^2, \quad (205)$$

in terms of the LL form factors [see Eq. (141) and their explicit form (A2), discussed in Appendix A]

$$\begin{aligned} \mathcal{F}_n(\mathbf{q}) &= \frac{1}{2} \left[ (1 - \delta_{n,0}) L_{n-1} \left( \frac{q^2 l_B^2}{2} \right) \right. \\ &\quad \left. + (1 + \delta_{n,0}) L_n \left( \frac{q^2 l_B^2}{2} \right) \right] e^{-q^2 l_B^2/4}, \end{aligned} \quad (206)$$

independent of the band index  $\lambda$  (Goerbig *et al.*, 2006; Nomura and MacDonald, 2006). The Hamiltonian resulting from Eq. (151)

$$H_n = \frac{1}{2} \sum_{\mathbf{q}} v_n(\mathbf{q}) \bar{\rho}(-\mathbf{q}) \bar{\rho}(\mathbf{q}) \quad (207)$$

therefore defines, together with the commutation relation (204) the model of strongly-correlated electrons restricted to a single relativistic LL. The model respects the SU(4) spin-valley symmetry, and naturally, there is no kinetic energy scale because all processes involve states within the same LL.

*a. Algebraic properties.* The SU(4) spin-valley symmetry is formally described with the help of the spin and valley-pseudospin operators

$$\bar{S}^\mu(\mathbf{q}) = (S^\mu \otimes \mathbb{1}) \otimes \bar{\rho}(\mathbf{q}) \quad \text{and} \quad \bar{I}^\mu(\mathbf{q}) = (\mathbb{1} \otimes I^\mu) \otimes \bar{\rho}(\mathbf{q}), \quad (208)$$

respectively, that are tensor products between the projected density operators (203) and the operators  $S^\mu$  and  $I^\mu$ , which are (up to a factor 1/2) Pauli matrices and that describe the spin and valley degrees of freedom, respectively. The operators  $(S^\mu \otimes \mathbb{1})$  and  $(\mathbb{1} \otimes I^\mu)$  are the generators of the SU(2)  $\times$  SU(2) subgroup of SU(4). However, once combined in a tensor product with the projected density operators  $\bar{\rho}(\mathbf{q})$ , the SU(2)  $\times$  SU(2)-extended magnetic translation group is no longer closed due to the non-commutativity of

the Fourier components of the projected density operators. The commutators  $[\bar{S}^\mu(\mathbf{q}), \bar{I}^\nu(\mathbf{q}')] yield the remaining generators of the SU(4)-extended magnetic translation group (Douçot *et al.*, 2008; Ezawa and Hasebe, 2002; Ezawa *et al.*, 2003).$

Physically, the operators introduced in Eq. (208) play the role of projected spin and valley-pseudospin densities, where the LL projection is induced by the projected charge-density operator  $\bar{\rho}(\mathbf{q})$ . Their non-commutativity with the projected charge density,  $[\bar{S}^\mu(\mathbf{q}), \bar{\rho}(\mathbf{q}')] \neq 0$  and  $[\bar{I}^\mu(\mathbf{q}), \bar{\rho}(\mathbf{q}')] \neq 0$ , which are due to the commutation relation (204), is at the origin of the (pseudo-)spin-charge entanglement in quantum Hall systems: as we discuss in more detail in Sec. V.B.2, this entanglement yields (pseudo-)spin-texture states that carry an electric in addition to their topological charge.

*b. Validity of the model.* With the help of the Hamiltonian (207), we may render more transparent the model assumption of electrons restricted to a single relativistic LL. We need to show that the energy scale that governs the model (207) and its resulting phases is indeed given by  $e^2/\varepsilon R_C$  and not  $e^2/\varepsilon l_B$ . As an upper bound for the energy scale, one may use the energy of a completely filled LL described by  $\langle c_{\lambda n, m; \xi, \sigma}^\dagger c_{\lambda n, m'; \xi, \sigma} \rangle = \delta_{m, m'}$ , the mean-field energy  $\langle H_n \rangle / N$  of which is simply the exchange energy,<sup>28</sup>

$$E_X^n = -\frac{1}{2} \sum_{\mathbf{q}} v_n(\mathbf{q}) = -\frac{e^2}{2\varepsilon} \int_0^\infty dq [\mathcal{F}_n(q)]^2. \quad (209)$$

In order to estimate the integral in the large- $n$  limit, one may use the scaling form (Abramowitz and Stegun, 1970; Gradshteyn and Ryzhik, 2000) of the Laguerre polynomials

$$L_n \left( \frac{q^2 l_B^2}{2} \right) e^{-q^2 l_B^2 / 4} \simeq J_0(q l_B \sqrt{2n+1}), \quad (210)$$

in terms of the Bessel function  $J_0(x)$ , such that one obtains by a simple change of the integration variable  $\int_0^\infty dq [\mathcal{F}_n(q)]^2 \simeq (l_B \sqrt{2n})^{-1} \int_0^\infty dx [J_0(x)]^2 = c/l_B \sqrt{2n}$ , where  $c$  is a numerical factor of order one. The exchange energy of a completely filled LL  $n$  therefore scales with  $n \gg 1$  as

$$E_X^n \simeq -c \frac{e^2}{\varepsilon l_B \sqrt{2n}} \simeq -c \frac{e^2}{\varepsilon R_C}, \quad (211)$$

in agreement with the model assumption of a separation between high- and low-energy degrees of freedom and the definition (202) of the coupling constant  $\alpha_G^B$ .

## 2. Symmetry-breaking long-range terms

When decomposing the Coulomb interaction in the two-spinor basis (Sec. III.A), we have seen that the SU(4)-symmetric model yields the leading energy scale, whereas the only relevant symmetry-breaking term is associated with backscattering processes at an energy scale roughly  $a/l_B$  times smaller than the leading one. When restricted to a single relativistic LL  $\lambda n$ , these backscattering terms yield a contribution

$$H_n^{sb} = \frac{1}{2} \sum_{\xi=\pm} \sum_{\mathbf{q}} v_n^{sb}(\mathbf{q}) \bar{\rho}^{\xi, -\xi}(-\mathbf{q}) \bar{\rho}^{-\xi, \xi}(\mathbf{q}), \quad (212)$$

in terms of the effective *backscattering* potential

$$\begin{aligned} v_n^{sb}(\mathbf{q}) &= \frac{2\pi e^2}{\varepsilon q} \left| \mathcal{F}_{\lambda n, \lambda n}^{+, -}(\mathbf{q}) \right|^2 \\ &= \frac{2\pi e^2}{\varepsilon q} \frac{(1 - \delta_{0, n})}{2n} (q_y - K_y)^2 l_B^2 \\ &\quad \times \left[ L_{n-1}^1 \left( \frac{|\mathbf{q} - \mathbf{K}|^2 l_B^2}{2} \right) \right]^2 e^{-|\mathbf{q} - \mathbf{K}|^2 l_B^2 / 2}, \end{aligned} \quad (213)$$

where we have made use of Eq. (142) and of the explicit expressions for the intervening matrix elements (A4).

The effect of this symmetry-breaking term will be discussed in more detail in Sec. V.B in the context of the SU(4) quantum Hall ferromagnetism. The term (212) is only relevant in relativistic LLs  $n \neq 0$  as a consequence of the factor  $(1 - \delta_{n, 0})$  in the expression (213) for the backscattering potential (Goerbig *et al.*, 2006). This is a consequence of the chiral symmetry of the zero-energy LL (Arikawa *et al.*, 2008) where the sublattice index is confounded with the valley pseudospin, as may be seen from the expression (88) for the associated wave functions. Notice, however, that there may occur other symmetry-breaking terms in  $n = 0$  as a consequence of short-range interactions on the lattice scale (Alicea and Fisher, 2006; Doretto and Morais Smith, 2007; Herbut, 2007b).

## 3. Qualitative expectations for correlated electron phases

The model of interacting electrons in a single relativistic LL has the same structure as the one for non-relativistic LLs – in both cases, one has an interaction Hamiltonian that is quadratic in the projected density operators (203) which satisfy the commutation relations (204). This is a noticeable result in the sense that, whereas non-relativistic 2D electron systems are governed by Galileian invariance, the electrons in graphene are embedded in a Lorentz-invariant “space-time”. However, once restricted to a single LL, the electrons forget about their original spatial symmetry properties and are governed by the magnetic translation algebra, which is at the origin of the commutation relations (204). As a consequence and in contrast to the IQHE, the differences between strongly-correlated electrons in graphene and

<sup>28</sup> The direct energy is compensated by the positively charged background (“jellium model”) (Mahan, 1993)

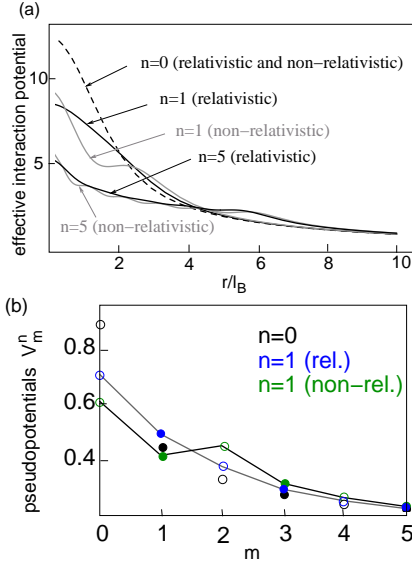


Figure 24 (a) From Ref. (Goerbig *et al.*, 2006); comparison between the relativistic (black curves) and non-relativistic (grey curves) potentials for the LLs  $n = 0, 1$ , and  $5$  in real space. The dashed line shows the potential in  $n = 0$ , which is the same in both the relativistic and the non-relativistic case. (b) Pseudopotentials for  $n = 0$  (black circles),  $n = 1$  relativistic (blue) and  $n = 1$  non-relativistic (green). The lines are a guide to the eye. The open circles represent pseudopotentials with even relative pair angular momentum that are irrelevant in the case of completely spin-valley polarized electronic states. The energies are given in units of  $e^2/\epsilon l_B$ .

non-relativistic 2D electrons do not stem from their respective space-time properties, as one would expect from a mean-field Chern-Simons approach (Khveshchenko, 2007; Peres *et al.*, 2006).

The differences between graphene and non-relativistic 2D electrons are rather to be sought in the larger internal symmetry – instead of an  $SU(2)$  spin symmetry, one has an  $SU(4)$  spin-valley symmetry if one neglects the small symmetry-breaking term (212) in the interactions. Another difference arises from the different effective interaction potential (205), instead of

$$v_n^{\text{non-rel}}(\mathbf{q}) = \frac{2\pi e^2}{\epsilon q} \left[ L_n \left( \frac{q^2 l_B^2}{2} \right) \right]^2 e^{-q^2 l_B^2 / 2} \quad (214)$$

for the usual 2D electron gas. As one may see from the graphene form factors (206), the effective interaction potential in graphene for  $n \neq 0$  is the average of the non-relativistic ones in the adjacent LLs  $n$  and  $n - 1$ , whereas for  $n = 0$  there is no difference between the relativistic and the non-relativistic case (see Fig. 24), as a consequence of the above-mentioned chiral properties.

One notices, furthermore, that the difference between the relativistic and non-relativistic effective interaction potentials become less prominent in the large- $n$  limit [see  $n = 5$  in Fig. 24(a)]. This may be understood from the approximate expression (210) of the form factors, which yields  $\mathcal{F}_n(\mathbf{q}) \simeq [J_0(q l_B \sqrt{2n+1}) + J_0(q l_B \sqrt{2n-1})]/2 \simeq$

$J(q l_B \sqrt{2n}) + \mathcal{O}(1/n)$ . This result agrees indeed to leading order in  $1/n$  with the scaling expression of the form factors (154) for usual non-relativistic 2D electrons.

The strongest difference in the interaction potentials is thus found for  $n = 1$ , which in graphene is quite reminiscent to that in  $n = 0$ , apart from a reduced repulsion at very short distances, whereas for non-relativistic 2D electrons it has an additional structure [see Fig. 24(a)]. The behavior of the effective interaction potential may also be analyzed with the help of Haldane’s pseudopotentials (Haldane, 1983)

$$V_\ell^n = \frac{1}{2\pi} \sum_{\mathbf{q}} v_n(\mathbf{q}) L_\ell(q^2 l_B^2) e^{-q^2 l_B^2 / 2}, \quad (215)$$

which represent the interaction between pairs of electrons in a magnetic field, in a relative angular momentum state with quantum number  $\ell$ . This quantum number is related to the average distance  $l_B \sqrt{2\ell + 1}$  between the two particles constituting the pair and is a good quantum number for any two-particle interaction potential  $v(\mathbf{r}_i - \mathbf{r}_j)$ . The pseudopotentials for graphene are shown in Fig. 24(b) for  $n = 0$  and  $1$ .

Haldane’s pseudopotentials are an extremely helpful quantity in the understanding of the possible FQHE states which one may expect in 2D electron systems. One notices first that as a consequence of the anti-symmetry of a two-particle wave function under fermion exchange, the relative angular-momentum quantum number  $\ell$  must be an *odd* integer, i.e. only the pseudopotentials with odd values of  $\ell$  play a physical role in the description of two interacting electrons of the same type (spin or valley). Even- $\ell$  pseudopotentials become relevant if the  $SU(4)$  spin-valley pseudospin is not completely polarized, in the treatment of two electrons with different internal quantum number  $\sigma$  or  $\xi$ . One then notices that the  $n = 1$  pseudopotentials, apart from the difference in  $V_{\ell=0}$ , are much more reminiscent of those in  $n = 0$  than of those for non-relativistic 2D electrons in the same LL  $n = 1$  [see Fig. 24(b)]. If one considers polarized electrons, one therefore expects essentially the same strongly-correlated electronic phases in graphene for  $n = 1$  as for  $n = 0$  (Goerbig *et al.*, 2006), as also corroborated by numerical studies for FQHE states (Apalkov and Chakraborty, 2006; Goerbig and Regnault, 2007; Papić *et al.*, 2009; Töke and Jain, 2007; Töke *et al.*, 2006) and electron-solid phases (Poplavskyy *et al.*, 2009; Zhang and Joglekar, 2007, 2008). Because the pseudopotentials (215) are systematically larger in  $n = 1$  than in  $n = 0$  (apart from the short-range component for  $\ell = 0$ ), the gaps of the FQHE states in  $n = 1$  are larger than the corresponding ones in  $n = 0$ , as one may also see from numerical calculations (Apalkov and Chakraborty, 2006; Töke *et al.*, 2006).

As much as we have emphasized the similarity between the  $n = 0$  and  $n = 1$  LLs in graphene, we need to stress the difference between the  $n = 1$  LL in graphene as compared to  $n = 1$  in non-relativistic 2D electron systems. Remember that the physical phase diagram in the

non-relativistic  $n = 1$  LL is extremely rich; an intriguing even-denominator FQHE has been observed at  $\nu = 5/2$  (Willett *et al.*, 1987) and probably possesses non-Abelian quasiparticle excitations (Greiter *et al.*, 1991; Moore and Read, 1991). Furthermore, a particular competition between FQHE states and electron-solid phases, which is characteristic of the non-relativistic  $n = 1$  LL (Goerbig *et al.*, 2003, 2004), is at the origin of the reentrance phenomena observed in transport measurements (Eisenstein *et al.*, 2002; Lewis *et al.*, 2005). These phenomena are absent in the  $n = 0$  LL, and the similarity between the  $n = 0$  and the relativistic  $n = 1$  LL thus leads to the expectation that FQHE states corresponding to the  $5/2$  state in non-relativistic quantum Hall systems and the above-mentioned reentrance phenomena are absent in the  $n = 1$  LL in graphene. This expectation has recently been corroborated in exact-diagonalization studies on the non-Abelian  $5/2$  state (Wojs *et al.*, 2010).

#### 4. External spin-valley symmetry breaking terms

Before we consider the different phases due to electron-electron interactions, we start with an analysis of the different *external* effects,<sup>29</sup> which are capable of lifting the four-fold spin-valley degeneracy.

The probably most familiar external symmetry-breaking term is the Zeeman effect, which lifts the two-fold spin degeneracy while maintaining the SU(2) symmetry associated with the valley pseudospin. The size of the Zeeman splitting is given by the energy  $\Delta_Z \sim 1.2B[\text{T}] K$ , for a  $g$ -factor that has been experimentally determined as  $g \sim 2$  (Zhang *et al.*, 2006). If we adopt a compact eight-spinor notation to take into account the four different spin-valley components, in addition to the two sublattice components, the Zeeman term has the form

$$\begin{aligned} \Delta_Z^{\text{spin}} &\sim \Psi^\dagger (\mathbb{1}_{\text{valley}} \otimes \mathbb{1}_{AB} \otimes \tau_{\text{spin}}^z) \Psi \\ &\sim \psi_{K,\uparrow}^{A\dagger} \psi_{K,\uparrow}^A - \psi_{K,\downarrow}^{A\dagger} \psi_{K,\downarrow}^A + \psi_{K',\uparrow}^{A\dagger} \psi_{K',\uparrow}^A - \psi_{K',\downarrow}^{A\dagger} \psi_{K',\downarrow}^A \\ &\quad + (A \leftrightarrow B), \end{aligned} \quad (216)$$

where the tensor product consists of the valley pseudospin (represented by the Pauli matrices  $\tau_{\text{valley}}^\mu$  and  $\mathbb{1}_{\text{valley}}$ ), the sublattice pseudospin ( $\tau_{AB}^\mu$  and  $\mathbb{1}_{AB}$ ), and the true spin ( $\tau_{\text{spin}}^\mu$  and  $\mathbb{1}_{\text{spin}}$ ). For a better understanding, we have given the explicit expression in terms of spinor components in the second line of Eq. (216).

A possible valley-degeneracy lifting, that one could describe with the help of a ‘‘valley Zeeman effect’’ similarly to Eq. (216),

$$\Delta_Z^{\text{valley}} \sim \Psi^\dagger (\tau_{\text{valley}}^z \otimes \mathbb{1}_{AB} \otimes \mathbb{1}_{\text{spin}}) \Psi, \quad (217)$$

is more involved because there is no physical field that couples directly to the valley pseudospin, as suggested by the otherwise intuitive form (217). There have however been proposals that such an effect may be achieved with the help of strain-induced disordered gauge fields that mimic large-scale ripples (Meyer *et al.*, 2007) and that yield an easy-plane anisotropy in  $n = 0$  (Abanin *et al.*, 2007a), similarly to the backscattering term (213) in higher LLs. Quite generally, a valley-degeneracy lifting may be achieved indirectly in the zero-energy LL  $n = 0$  via fields that couple to the sublattice index. This is due to the fact that the components  $\psi_{K,\sigma}^A$  and  $\psi_{K',\sigma}^B$  vanish as a consequence of the chiral properties, which identify the sublattice and the valley pseudospins in  $n = 0$ , as we have discussed in Sec. II.A.2.

In order to illustrate this indirect lifting of the valley degeneracy, we consider the term (Haldane, 1988)

$$\mathcal{M}_H = M \Psi^\dagger (\mathbb{1}_{\text{valley}} \otimes \tau_{AB}^z \otimes \mathbb{1}_{\text{spin}}) \Psi, \quad (218)$$

which breaks the lattice inversion symmetry and opens a mass gap at the Dirac point in the absence of a magnetic field. In the presence of a  $B$ -field, the LL spectrum (85) is modified by the term (218) and reads

$$\epsilon_{\lambda,n;\xi} = \lambda \sqrt{M^2 + 2 \frac{\hbar^2 v_F^2}{l_B^2} n}, \quad (219)$$

for  $n \neq 0$ , independent of the valley index  $\xi$ , whereas the fate of the  $n = 0$  LL depends explicitly on  $\xi$ ,

$$\epsilon_{n=0;\xi} = \xi M, \quad (220)$$

such that the valley degeneracy is effectively lifted. Notice, however, that due to the vanishing components  $\psi_{K,\sigma}^A$  and  $\psi_{K',\sigma}^B$ , the mass term (218) is now indistinguishable (in  $n = 0$ ) from the above-mentioned valley Zeeman term (217),

$$\begin{aligned} \mathcal{M}_H^{n=0} &\sim \Psi^\dagger (\mathbb{1}_{\text{valley}} \otimes \tau_{AB}^z \otimes \mathbb{1}_{\text{spin}}) \Psi \\ &\sim \Psi^\dagger (\tau_{\text{valley}}^z \otimes \mathbb{1}_{AB} \otimes \mathbb{1}_{\text{spin}}) \Psi, \end{aligned} \quad (221)$$

whereas this is not the case for the LLs  $n \neq 0$ , where the valley degeneracy is only lifted by an explicit valley Zeeman effect. A mass term of the form (218) typically arises in the presence of a frozen out-of-plane phonon that yields a crumbling of the graphene sheet (Fuchs and Lederer, 2007).

More recent studies have concentrated on a spontaneous deformation of the graphene sheet due to frozen in-plane phonons that yield a Kekulé-type distortion (Hou *et al.*, 2010; Nomura *et al.*, 2009). This distortion, which is associated with a characteristic wave vector  $2\mathbf{K}$  and which therefore couples the two valleys, directly breaks the valley degeneracy, via a term  $\mathcal{M}_K = \mathcal{M}_x + \mathcal{M}_y$ , with

$$\mathcal{M}_{x,y} = \frac{\Delta_{x,y}}{2} \Psi^\dagger (\tau_{\text{valley}}^{x,y} \otimes \mathbb{1}_{AB} \otimes \mathbb{1}_{\text{spin}}) \Psi. \quad (222)$$

<sup>29</sup> By external effects we mean those that are not caused by the mutual Coulomb repulsion between the electrons.

Such a term yields the same energy spectrum (219) and (220) as the mass term (218) if one replaces  $M$  by  $\Delta_{kek}/2$ , with the characteristic energy scale  $\Delta_{kek} = \sqrt{\Delta_x^2 + \Delta_y^2} \simeq 2B[\text{T}] \text{ K}$ , (Ajiki and Ando, 1995; Hou *et al.*, 2010). Notice that this energy scale is slightly larger than, but roughly on the same order as, the Zeeman energy scale.

Finally, we mention another class of terms that break the spin-valley degeneracy and that have received recent interest in the framework of research on topological insulators [for recent reviews see (Hasan and Kane, 2010; Qi and Zhang, 2011)]. In an original work, Haldane argued that a time-reversal-symmetry breaking term with an inhomogeneous flux distribution inside each hexagon opens a gap in a honeycomb lattice with zero magnetic field (Haldane, 1988). Most saliently, he showed that one may thus achieve a quantum Hall effect without an external magnetic field, a system that is now often referred to as the “quantum anomalous Hall insulator” (Hasan and Kane, 2010; Qi and Zhang, 2011). A similar situation arises when spin-orbit interactions are taken into account, which are of the form

$$\mathcal{H}_{SO} = \frac{\Delta_{SO}}{2} \Psi^\dagger (\tau_{\text{valley}}^z \otimes \tau_{AB}^z \otimes \tau_{\text{spin}}^z) \Psi \quad (223)$$

and which provide again the same LL spectrum (219) and (220) if one replaces  $M$  by  $\Delta_{SO}/2$  (Kane and Mele, 2005). In spite of the conceptually appealing prospect of the quantum spin Hall effect, which is revealed by this model because the spin orientation is locked to a particular valley index via the term (223), the associated energy scale  $\Delta_{SO} \sim 10 \text{ mK}$  turns out to be van-

ishingly small in graphene, whereas an extrinsic Rashba-type spin-orbit coupling in graphene can be on the order of 1 K (Min *et al.*, 2006).

## 5. Hierarchy of relevant energy scales

These energy scales associated with external fields need to be compared to the characteristic (bare) interaction energy  $e^2/\epsilon l_B \simeq 625(\sqrt{B[\text{T}]}/\epsilon) \text{ K}$ , which is, for experimentally accessible magnetic fields, much larger than  $\Delta_Z$  or  $\Delta_{kek}$ . As we have discussed in Sec. III.B.4, inter-band LL excitations screen the bare Coulomb interaction and yield a contribution to the dielectric constant. In the absence of a quantizing magnetic field, we have seen that this dielectric constant is given by [see Eq. (176)]

$$\epsilon_\infty = 1 + \frac{\pi}{2} \alpha_G = 1 + \frac{\pi}{2} \frac{e^2}{\hbar \epsilon v_F}, \quad (224)$$

where we remember that  $\epsilon$  is the *extrinsic* dielectric constant of the surrounding medium. As one may notice from Fig. 18, the vacuum contribution  $\Pi^{vac}(\mathbf{q})$  (thick dashed lines) is only marginally modified by the magnetic field, such that one may use  $e^2/\epsilon \epsilon_\infty l_B$  as an approximation for the interaction-energy scale for graphene taking into account inter-band screening.

The relevant energy scales are summarized in the table below for different values of the magnetic field, in comparison with the interaction energy scales, taking into account the effective dielectric constants for several widely used substrates from Tab. I.

energy	value for arbitrary $B$	for $B = 6 \text{ T}$	for $B = 25 \text{ T}$
$\Delta_Z$	$1.2B[\text{T}] \text{ K}$	7 K	30 K
$\Delta_{kek}$	$2B[\text{T}] \text{ K}$	12 K	50 K
$e^2/\epsilon l_B$ (bare)	$625(\sqrt{B[\text{T}]}/\epsilon) \text{ K}$	$(1550/\epsilon) \text{ K}$	$(3125/\epsilon) \text{ K}$
$e^2/\epsilon \epsilon_\infty l_B$ (vacuum)	$139\sqrt{B[\text{T}]} \text{ K}$	344 K	694 K
$e^2/\epsilon \epsilon_\infty l_B$ (on SiO <sub>2</sub> )	$104\sqrt{B[\text{T}]} \text{ K}$	258 K	521 K
$e^2/\epsilon \epsilon_\infty l_B$ (on h-BN)	$109\sqrt{B[\text{T}]} \text{ K}$	270 K	543 K
$e^2/\epsilon \epsilon_\infty l_B$ (on SiC)	$71\sqrt{B[\text{T}]} \text{ K}$	176 K	355 K
$\Delta_{sb} < (e^2/\epsilon l_B)(a/l_B)$	$< 1B[\text{T}] \text{ K}$	$< 6 \text{ K}$	$< 25 \text{ K}$

Table II Energy scales at different magnetic fields. The first two lines show the energy scales associated with the major external symmetry-breaking fields (Zeeman and Kekulé-type lattice distortion,  $\Delta_Z$  and  $\Delta_{kek}$ , respectively), which scale linearly in  $B$ . Below are shown the interaction-energy scales ( $\propto \sqrt{B}$ ), the bare one with an unspecified dielectric constant and the ones for different substrates taking into account inter-band screening via the term  $\epsilon_\infty$  [Eq. (224)]. The last line yields the interaction-energy scale associated with the intrinsic symmetry breaking due to inter-valley coupling, discussed in Sec. V.A.2.

In view of the above discussion, one may conclude that the SU(4)-symmetric part of the Coulomb interaction

yields the leading energy scale in the problem of electrons in partially filled lower LLs, whereas external terms,



such as the Zeeman effect or spontaneous lattice distortions, play a subordinate role. The remainder of this section is therefore concerned with a detailed discussion of strongly-correlated electron phases that are formed to minimize the Coulomb interaction.

## B. SU(4) Quantum Hall Ferromagnetism in Graphene

A prominent example of the above-mentioned strongly-correlated phases is the generalized quantum Hall ferromagnet. It arises in systems with a discrete internal degree of freedom described by an  $SU(\mathcal{N})$  symmetry, such that each single-particle quantum state  $\psi_{n,m}$  occurs in  $\mathcal{N}$  copies. Prominent examples are the non-relativistic quantum Hall systems when taking into account the electronic spin  $\sigma = \uparrow, \downarrow$  ( $\mathcal{N} = 2$ ) or bilayer quantum Hall systems that consist of two parallel 2D electron gases, where the layer index may be viewed as a “spin”  $1/2$  [ $\mathcal{N} = 2$ , or  $\mathcal{N} = 4$  if one also takes into account the physical spin (Ezawa and Hasebe, 2002; Ezawa *et al.*, 2003)].<sup>30</sup> In this sense, graphene may be viewed as an  $SU(4)$  quantum Hall system as a consequence of its four-fold spin-valley degeneracy.

### 1. Ferromagnetic ground state and Goldstone modes

Quite generally, quantum Hall ferromagnetism arises when the filling factor, defined from the bottom of the LL,<sup>31</sup> is an integer that is not a multiple of  $\mathcal{N}$  (Arovas *et al.*, 1999). From the point of view of the kinetic Hamiltonian, one is thus confronted with a macroscopic ground-state degeneracy. Even if one has an integer filling factor, the situation is thus much more reminiscent of the FQHE, i.e. the relevant energy scale is the Coulomb interaction, and the system may be described in the framework of the model (207) of interacting electrons in a single (relativistic) LL. For the moment, we consider that there are no symmetry-breaking terms, such as the backscattering term (212) or Zeeman-type terms that are discussed below in Sec. V.A.4.

Qualitatively, one may understand the formation of a ferromagnetic ground state as a consequence of the repulsive Coulomb interaction. In order to minimize this interaction, the electrons prefer to form a state described by a maximally anti-symmetric orbital wave function that must then be accompanied by a fully symmetric  $SU(\mathcal{N})$  spin wave function to satisfy an overall fermionic (anti-symmetric) wave function. In a usual metal with a finite band dispersion, this ferromagnetic ordering (e.g. all

electrons in the spin- $\uparrow$  states) is accompanied by a cost in kinetic energy – indeed, the Fermi energy for spin- $\uparrow$  electrons is increased whereas that of spin- $\downarrow$  electrons is lowered. The competition between the gain in interaction and the cost in kinetic energy defines the degree of polarization, i.e. how ferromagnetic the electrons effectively are. In the quantum Hall effect, however, we are confronted with a highly degenerate LL that may be viewed as an infinitely flat band, such that the kinetic-energy cost for complete spin polarization is zero.

As an example of an  $SU(\mathcal{N})$  quantum Hall ferromagnet, one may consider the state

$$|\text{FM}\rangle = \prod_{i=1}^k \prod_{m=0}^{N_B-1} c_{m,i}^\dagger |\text{vac}\rangle, \quad (225)$$

which consists of  $k < \mathcal{N}$  arbitrarily chosen completely filled subbranches [ $i \in \{(K, \uparrow), (K', \uparrow), (K, \downarrow), (K', \downarrow)\}$ , for the  $SU(\mathcal{N} = 4)$  symmetry in graphene LLs], where we have omitted the LL index  $\lambda n$  at the fermion operators to simplify the notation. The arbitrariness in the choice of the  $SU(\mathcal{N})$  spin subbranches may be viewed as a spontaneous symmetry breaking that accompanies the ferromagnetism. Indeed, the state (225) is no longer invariant under an  $SU(\mathcal{N})$  rotation, but only under a rotation described by the subgroup  $SU(k) \times SU(\mathcal{N} - k)$ , where the first factor indicates a symmetry transformation in the fully occupied subbranches  $i = 1, \dots, k$  and the second factor one in the empty subbranches  $i = k+1, \dots, \mathcal{N}$ . Therefore the quantum Hall ferromagnet (225) is associated with an order parameter with a spontaneous symmetry breaking described by the coset space  $SU(\mathcal{N})/SU(k) \times SU(\mathcal{N} - k) \times U(1) \sim U(\mathcal{N})/U(k) \times U(\mathcal{N} - k)$ , where the additional  $U(1)$  is due to the phase difference between the occupied and the unoccupied subbranches (Arovas *et al.*, 1999; Yang *et al.*, 2006).

The coset space, with its  $\mathcal{N}^2 - k^2 - (\mathcal{N} - k)^2 = 2k(\mathcal{N} - k)$  complex generators, defines also the Goldstone modes, which are nothing other than the  $k(\mathcal{N} - k)$  spin-wave excitations of the ferromagnetic ground state (225).<sup>32</sup> The number of the spin-wave modes may also have been obtained from a simple inspection into the LL-subbranch spectrum. Indeed, a spin wave can be described with the help of the components of the projected density operators (203),

$$\bar{\rho}_{ij}(\mathbf{q}) = \sum_{m,m'} \langle m | e^{-i\mathbf{q}\cdot\mathbf{R}} | m' \rangle c_{m,i}^\dagger c_{m',j}, \quad (226)$$

which represent coherent superpositions at wave vector  $\mathbf{q}$  of excitations from the occupied subbranch  $j$  to the empty subbranch  $i$ . One has then  $k$  possibilities for the choice of the initial subbranch  $j$  and  $\mathcal{N} - k$  for the final

<sup>30</sup> For a review on non-relativistic multi-component systems see Ref. (Ezawa, 2000; Moon *et al.*, 1995).

<sup>31</sup> Remember that the filling factor in graphene is defined with respect to the center of the  $n = 0$  LL. There is thus a shift of 2 in the filling factor as compared to the non-relativistic case.

<sup>32</sup> The complex generators come in by pairs of conjugate operators, and each pair corresponds to one mode.

one, and one obtains therefore  $k(\mathcal{N} - k)$  different spin-wave excitations, in agreement with the above group-theoretical analysis.

Notice that all spin-wave excitations have the same dispersion, which may be calculated within a mean-field approximation (Alicia and Fisher, 2006; Doretto and Morais Smith, 2007; Kallin and Halperin, 1984; Yang *et al.*, 2006),

$$\begin{aligned} E_{\mathbf{q}} &= \langle \text{FM} | \bar{\rho}_{ij}(-\mathbf{q}) H_n \bar{\rho}_{ij}(\mathbf{q}) - H_n | \text{FM} \rangle \\ &= 2 \sum_{\mathbf{k}} v_n(\mathbf{k}) \sin^2 \left( \frac{\mathbf{q} \wedge \mathbf{k} l_B^2}{2} \right), \end{aligned} \quad (227)$$

which saturates at large values of  $q = |\mathbf{q}|$ ,

$$E_{q \rightarrow \infty} = 2E_X^n = \sum_{\mathbf{k}} v_n(\mathbf{k}), \quad (228)$$

i.e. at twice the value of the exchange energy (209). This result is not astonishing insofar as the large- $q$  limit corresponds, as we have discussed in Sec. III.B.2 [see Eq. (167)], to an electron-hole pair where the electron is situated far away from the hole. The energy (228) is therefore nothing other than the cost in exchange energy to create a *spin-flip* excitation, i.e. an electron with reversed spin and a hole in the ferromagnetic ground state. Because of the large distance between the electron and the hole in such an excitation and the resulting decoupled dynamics, one may be tempted to view this energy as the activation gap of the quantum-Hall state at  $\nu = k$ , but we see below in Sec. V.B.2 that there exist elementary charged excitations (skyrmions) that have, in some LLs, a lower energy than these spin-flip excitations.

In the opposite limit of small wave vectors ( $ql_B \ll 1$ ), one may not understand the excitation in terms of decoupled holes and electrons, and the excitation can therefore not contribute to the charge transport. A Taylor expansion of the sine in the spin-wave dispersion (227) yields the usual  $q^2$  dispersion of the spin-wave Goldstone modes,

$$E_{q \rightarrow 0} = \frac{\rho_s^n}{2} q^2 l_B^2, \quad (229)$$

in terms of the *spin stiffness*

$$\rho_s^n = \frac{1}{4\pi} \sum_{\mathbf{k}} v_n(\mathbf{k}) |\mathbf{k}|^2 l_B^2. \quad (230)$$

One notices that the above results for the excitation energies do not depend on the size of the internal symmetry group, but they can be derived within the SU(2) model of the quantum Hall ferromagnetism (Moon *et al.*, 1995; Sondhi *et al.*, 1993) – the enhanced internal symmetry of graphene (or of a general  $\mathcal{N}$ -component system) affects only the degeneracies of the different modes.

## 2. Skyrmions and entanglement

In addition to the above-mentioned spin-wave modes, the SU( $\mathcal{N}$ ) ferromagnetic ground state (225) is charac-

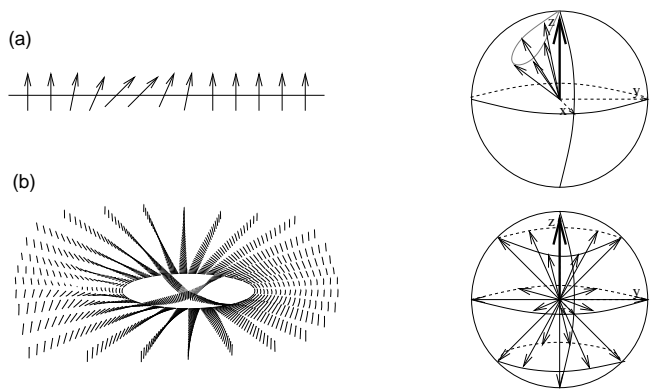


Figure 25 Excitations of the SU(2) ferromagnetic state. (a) Spin waves. Such an excitation can be continuously deformed into the ferromagnetic ground state [spin represented on the Bloch sphere (right) by fat arrow] – the grey curve can be shrunk into a single point (b) Skyrmion with non-zero topological charge [from Ref. (Girvin, 1999)]. The excitation consists of a reversed spin at the origin  $z = 0$ , and the ferromagnetic state is recovered at large distances  $|z/\zeta| \rightarrow \infty$ . Contrary to spin-wave excitations, the spin explores the whole surface of the Bloch sphere and cannot be transformed by a continuous deformation into the majority spin (fat arrow).

terized by a particular elementary excitation that consists of a topological spin texture, the so-called *skyrmion* (Sondhi *et al.*, 1993). Similarly to a spin-wave in the limit  $ql_B \ll 1$ , the variation of the spin texture in a skyrmion excitation is small on the scale of the magnetic length  $l_B$ , such that its energy is determined by the spin stiffness (230) in the small- $q$  limit. Indeed, one may show that its energy is given by (Ezawa, 2000; Moon *et al.*, 1995; Sondhi *et al.*, 1993)

$$E_{sk} = 4\pi \rho_s^n |Q_{top}|, \quad (231)$$

in terms of the topological charge  $Q_{top}$ , which may be viewed as the number of times the Bloch sphere is covered by the spin texture [see Fig. 25(b)] and which we discuss in more detail below. Skyrmions are the relevant elementary excitations of the quantum Hall ferromagnetism if the energy (231) is lower than that of an added electron (or hole) with reversed spin, which is nothing other than the exchange energy (209), i.e. if  $E_{sk} < E_X^n$ . Whereas this condition is fulfilled in non-relativistic LLs only in the lowest one  $n = 0$ , skyrmions are the lowest-energy elementary excitations in the graphene LLs  $n = 0, 1$  and  $2$  (Töke *et al.*, 2006; Yang *et al.*, 2006), as a consequence of the difference in the form factors.

As in the case of the spin waves discussed above, the skyrmion energy is independent of the size of the internal symmetry group, and we will first illustrate the skyrmion texture in an effective SU(2) model, where the texture is formed only from states within the last occupied ( $k$ ) and the first unoccupied ( $k+1$ ) LL subbranch. The skyrmion may then be described with the help of the wave function,

in terms of the complex coordinate  $z = (x - iy)/l_B$ ,

$$|\mathcal{S}_{k,k+1}\rangle = \frac{1}{\sqrt{|\zeta|^2 + |z|^2}} (z |\uparrow^k(z)\rangle + \zeta |\downarrow^{k+1}(z)\rangle) \quad (232)$$

where  $|\uparrow^k(z)\rangle$  corresponds to states in the subbranch  $k$  and  $|\downarrow^{k+1}(z)\rangle$  to those in  $k+1$ , at the position  $z$ . One notices that at the origin  $z = 0$  the “spin” associated with these two components is  $\downarrow$  because the first component of Eq. (232) vanishes, whereas the spins are  $\uparrow$  at  $|z/\zeta| \rightarrow \infty$  (see Fig. 25), where the ferromagnetic ground state is then recovered. The parameter  $\zeta$  plays the role of the skyrmion size, measured in units of  $l_B$  – indeed, for  $|z| = |\zeta|$ , both components are of the same weight and the spin is therefore oriented in the  $xy$ -plane.

The skyrmion excitation (232) can also be illustrated on the so-called Bloch sphere on the surface of which the (normalized) spin moves (see Fig. 25). The angles ( $\theta$  for the azimuthal and  $\phi$  for the polar angle) of the spin orientation on the Bloch sphere correspond to the SU(2) parametrization  $|\psi\rangle = \cos(\theta/2)|\uparrow\rangle + \sin(\theta/2)\exp(i\phi)|\downarrow\rangle$ , and the spin orientation at the circle  $|z| = |\zeta|$  in the complex plane describes the equator of the Bloch sphere. The topology of the skyrmion excitation becomes apparent by the number of full circles the spin draws when going around the origin of the  $xy$ -plane on the circle  $|z| = |\zeta|$ . More precisely, the topological charge  $Q_{top}$  is not defined in terms of such closed paths, but it is the number of full coverings of the Bloch sphere in a skyrmion excitation [ $Q_{top} = 1$  in the example (232)]. Notice that a spin-wave excitation has a topological charge  $Q_{top} = 0$  and corresponds to an excursion of the spin on the Bloch sphere that is not fully covered and that can then be reduced continuously to a single point describing the ferromagnetic ground state [Fig. 25(a)].

The above considerations may be generalized to systems with larger internal symmetries, i.e. to SU( $\mathcal{N}$ ) quantum Hall ferromagnets. The state (232) is invariant under the SU( $\mathcal{N}$ ) subgroup SU( $k-1$ )  $\times$  SU( $\mathcal{N}-k-1$ ), where the first factor describes a rotation of the occupied subbranches that do not take part in the skyrmion excitation and the second factor is associated with a symmetry transformation of the corresponding unoccupied subbranches  $k+2, \dots, \mathcal{N}$ . A similar group-theoretical analysis as the one presented in Sec. V.B.1 yields the number of residual symmetry transformations (Yang *et al.*, 2006)  $2k(\mathcal{N}-k) + 2(\mathcal{N}-1)$ , where the first term describes the Goldstone modes of the ferromagnetic ground state, and the second one corresponds to the  $\mathcal{N}-1$  internal modes of the skyrmion excitation.

In addition to the topological charge, skyrmions in quantum Hall systems carry an electric charge that coincides, for  $\nu = k$  with the topological charge. Indeed, the skyrmion state (232) describes an electron that is expelled from the origin  $z = 0$  in the  $\uparrow$ -component, and its net electric charge is therefore that of a hole. This means that skyrmions are excited when sweeping the filling factor away from  $\nu = k$ , and the net topological charge is

given by  $Q_{tot} = |\nu - k|N_B$ . The number of internal modes is then  $Q_{tot}(\mathcal{N}-1)$ , in addition to one mode per charge that corresponds to a simple translation  $z \rightarrow z + a$  of the excitation (Douçot *et al.*, 2008). As a consequence of the Coulomb repulsion, it is energetically favorable to form a state in which  $Q_{tot}$  skyrmions of charge 1 are homogeneously distributed over the 2D plane than a single defect with charge  $Q_{tot}$  (Moon *et al.*, 1995). A natural (semi-classical) candidate for the ground state of  $Q_{tot}$  skyrmions is then a skyrmion crystal (Brey *et al.*, 1995) that has recently been revisited in the framework of the SU(4) symmetry in graphene (Côté *et al.*, 2007, 2008). In this case, the  $Q_{tot}(\mathcal{N}-1)$  internal modes, which are dispersionless zero-energy modes in the absence of electronic interactions or Zeeman-type symmetry-breaking terms, are expected to yield  $\mathcal{N}-1$  Bloch bands of Goldstone-type, in addition to the  $Q_{tot}$  translation modes that form a magnetic-field phonon mode of the skyrmion crystal with a characteristic  $\omega \propto q^{3/2}$  dispersion (Fukuyama, 1975).

*a. Skyrmions and activation gaps in graphene.* Quite generally, the activation gap in quantum Hall states is the energy required to create a quasi-particle–quasi-hole pair, in which the two partners are sufficiently well separated to contribute independently to the charge transport. In the framework of the quantum Hall ferromagnet, the activation gap may be viewed as the energy to create a skyrmion of topological charge  $Q = 1$  and an anti-skyrmion of charge  $Q = -1$  that are well-separated from each other such that one may neglect their residual interaction. The energy of such a skyrmion–anti-skyrmion pair is then given, in the absence of symmetry-breaking terms, by twice the energy in Eq. (231),

$$\Delta_a^{\text{sym}} = 8\pi\rho_s^n. \quad (233)$$

For graphene, the energies of the theoretical activation gaps for  $n = 0$  and  $n = 1$  are shown in the table below.

	activation gap	arbitrary value of $B$
$n = 0$	$\frac{1}{2}\sqrt{\frac{\pi}{2}}\frac{e^2}{\varepsilon\varepsilon_\infty l_B}$	$400(\sqrt{B[\text{T}]}/\varepsilon\varepsilon_\infty) \text{ K}$
$n = 1$	$\frac{7}{32}\sqrt{\frac{\pi}{2}}\frac{e^2}{\varepsilon\varepsilon_\infty l_B}$	$175(\sqrt{B[\text{T}]}/\varepsilon\varepsilon_\infty) \text{ K}$

Table III Theoretical estimates for the activation gaps in the  $n = 0$  and 1 graphene LLs due to well-separated skyrmion–anti-skyrmion pairs.

For further illustration, we consider the scenario in which the Zeeman effect is the only SU(4)-symmetry breaking term.<sup>33</sup> Due to the Zeeman effect, spin- $\downarrow$  elec-

<sup>33</sup> The energetic argument remains valid in the case where the dominant term is a valley-Zeeman effect if one interchanges the role of the spin and the valley pseudospin.

trons are energetically favored. If only one spin-valley branch of a particular LL is filled ( $k = 1$ ), the spin magnetization of the spin-valley ferromagnet is preferentially oriented in this direction whereas the valley polarization may point in any direction. The activation gap would then be dominated by valley (anti-)skyrmions with no reversed physical spin such that one would not expect any dependence of the gap on the in-plane component of the magnetic field, in agreement with the experimental findings (Jiang *et al.*, 2007b).

The situation is different when both valley branches of the spin- $\downarrow$  branch are occupied; an excitation of the SU(4) ferromagnet with a full spin polarization would then necessarily comprise reversed spins, and the corresponding Zeeman energy must be taken into account in the energy of the (spin) skyrmion-anti-skyrmion pair (233),

$$\Delta_a^Z = 8\pi\rho_s^n + 2N_{rs}\Delta_Z, \quad (234)$$

where  $N_{rs} \sim |\zeta|^2$  is the number of reversed spins in a single (anti-)skyrmion. Notice that this number depends on the competition between the Zeeman effect itself, which tries to reduce the skyrmion size  $\zeta$ , and the cost in exchange energy due to the strong variation in small textures (Moon *et al.*, 1995; Sondhi *et al.*, 1993).<sup>34</sup> The energy of a skyrmion-anti-skyrmion pair in the spin channel (with two completely filled valley sublevels) is therefore larger than that (233) of a pair in the valley channel when only one valley subbranch of the LL is completely filled. Notice that this energy increase may even be significant for large skyrmions because of the larger number of reversed spins. As a thumbrule, the stability of a quantum Hall state is proportional to the activation gap, which has in the present case been identified with the skyrmion-anti-skyrmion energy and which is dominated by the Coulomb interaction energy. Additional external symmetry-breaking terms, such as those discussed in Sec. V.A.4, may enhance this stability although they provide only a small correction to the activation energy.

*b. Spin-valley entanglement in graphene.* In an experimental measurement, one typically has not direct access to the full SU(4) spin that describes the internal degrees of freedom in graphene LLs, but only to the SU(2) part associated with the physical spin, e.g. in a magnetization measurement. It is therefore useful to parametrise the SU(4) spin in a manner such as to keep track of the two SU(2) copies associated with the physical spin and with the valley pseudospin, respectively. This may be achieved with the so-called Schmidt decomposition of the

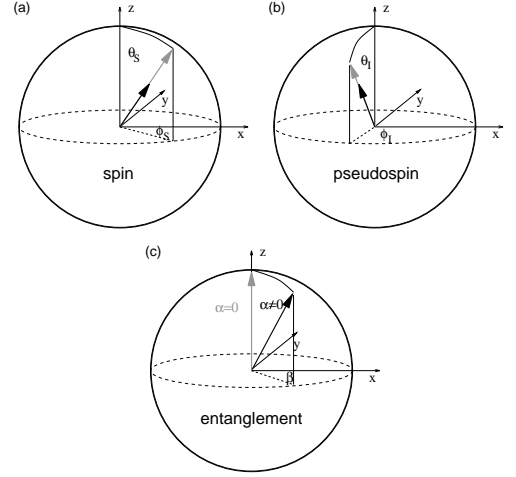


Figure 26 From Ref. (Douçot *et al.*, 2008); Bloch spheres for entangled spin-pseudospin systems. Bloch sphere for the spin (a), pseudospin (b), and a third type of spin representing the entanglement (c). In the case of spin-pseudospin entanglement ( $|\cos\alpha| \neq 1$ ), the (pseudo)spin-magnetizations explore the interior of their spheres, respectively (black arrows).

four-spinor

$$|\Psi(z)\rangle = \cos\frac{\alpha}{2}|\psi_S\rangle|\psi_I\rangle + \sin\frac{\alpha}{2}e^{i\beta}|\chi_S\rangle|\chi_I\rangle, \quad (235)$$

where  $\alpha$  and  $\beta$  are functions of the complex position  $z$ , and the local two-component spinors  $|\psi_S\rangle$ ,  $|\chi_S\rangle$ ,  $|\psi_I\rangle$ , and  $|\chi_I\rangle$  are constructed according to

$$|\psi\rangle = \begin{pmatrix} \cos\frac{\theta}{2} \\ \sin\frac{\theta}{2}e^{i\phi} \end{pmatrix} \quad \text{and} \quad |\chi\rangle = \begin{pmatrix} -\sin\frac{\theta}{2}e^{-i\phi} \\ \cos\frac{\theta}{2} \end{pmatrix}. \quad (236)$$

The angles  $\theta$  and  $\phi$  define the usual unit vector

$$\mathbf{n}(\theta, \phi) = (\sin\theta\cos\phi, \sin\theta\sin\phi, \cos\theta), \quad (237)$$

which explores the surface of the Bloch sphere depicted in Fig. 25. Notice that one has two Bloch spheres, one for the unit vector  $\mathbf{n}(\theta_S, \phi_S)$  associated with the spin angles  $\theta_S$  and  $\phi_S$  and a second one for  $\mathbf{n}(\theta_I, \phi_I)$  for the valley-pseudospin angles  $\theta_I$  and  $\phi_I$  (see Fig. 26). In addition, one may associate a third Bloch sphere with the angles  $\alpha$  and  $\beta$  that describe the degree of factorizability of the wave functions and thus the degree of entanglement between the spin and the valley pseudospin (Douçot *et al.*, 2008).

With the help of the Schmidt decomposition (235), one obtains immediately the reduced density matrices for the spin and the valley-pseudospin sectors

$$\begin{aligned} \rho_S &= \text{Tr}_I(|\Psi\rangle\langle\Psi|) = \cos^2\frac{\alpha}{2}|\psi_S\rangle\langle\psi_S| + \sin^2\frac{\alpha}{2}|\chi_S\rangle\langle\chi_S|, \\ \rho_I &= \text{Tr}_S(|\Psi\rangle\langle\Psi|) = \cos^2\frac{\alpha}{2}|\psi_I\rangle\langle\psi_I| + \sin^2\frac{\alpha}{2}|\chi_I\rangle\langle\chi_I|, \end{aligned} \quad (238)$$

<sup>34</sup> This energy cost may be evaluated from a gradient expansion of the energy in the magnetization fields. At leading order, one obtains, however, a non-linear sigma model that is scale-invariant, such that the energy cost must be calculated at higher orders (Moon *et al.*, 1995).

respectively, and the local spin and valley-pseudospin densities are simply

$$m_S^a = \text{Tr}(\rho_S S^a) = \cos \alpha \langle \psi_S | S^a | \psi_S \rangle = \cos \alpha n^a(\theta_S, \phi_S) \quad (239)$$

and

$$m_I^\mu = \text{Tr}(\rho_I I^\mu) = \cos \alpha \langle \psi_I | I^\mu | \psi_I \rangle = \cos \alpha n^\mu(\theta_I, \phi_I), \quad (240)$$

where  $S^a$  and  $I^\mu$  represent the components of the spin and valley-pseudospin operators, respectively [see Eq. (208)]. One notices from these expressions that, for the case  $\alpha \neq 0$  or  $\pi$  (i.e.  $\cos^2 \alpha < 1$ ), the local (pseudo)spin densities are no longer normalized, but they are of length  $|\mathbf{m}_{S/I}|^2 = \cos^2 \alpha$ . Thus, in a semiclassical picture, the (pseudo)spin dynamics is no longer restricted to the surface of the Bloch sphere, but explores the entire volume enclosed by the sphere (Fig. 26) (Douçot *et al.*, 2008). This result indicates that one may be confronted, in the case of full entanglement (e.g.  $\alpha = \pi/2$ ), with an SU(4) quantum Hall ferromagnet the (spin) magnetization of which completely vanishes, as one would naively expect for an *unpolarized* state.

### 3. Comparison with magnetic catalysis

An alternative scenario proposed for the degeneracy lifting in  $n = 0$  is that of the magnetic catalysis (Ezawa, 2007; Gorbar *et al.*, 2008; Gusynin *et al.*, 2006; Herbut, 2007b, 2008), which was discussed even before the discovery of graphene (Gorbar *et al.*, 2002; Khveshchenko, 2001). According to this scheme, the Coulomb interaction spontaneously generates a mass term for the (originally massless) 2D electrons once the magnetic field increases the density of states at zero energy by the formation of the highly degenerate  $n = 0$  LL. As a consequence of this mass generation, the particles condense in a state of coherent particle-hole pairs (excitonic condensation). The effect is at first sight reminiscent of the excitonic condensation at  $\nu = 1$  in non-relativistic bilayer quantum Hall systems (Ezawa and Iwazaki, 1993; Fertig, 1989; Wen and Zee, 1992a). Its superfluid behavior gives rise to a zero-bias anomaly in the tunneling conductance between the two layers (Spielman *et al.*, 2000) as well as to a simultaneous suppression of the longitudinal and the Hall resistance in a counterflow experiment (Kellogg *et al.*, 2004; Tutuc *et al.*, 2004). The bilayer excitonic condensate may be described as an easy-plane quantum Hall ferromagnet (Moon *et al.*, 1995), where the spin mimics the layer index. The origin of this easy-plane anisotropy stems from the difference in the interactions between electrons in the same layer as compared to the weaker one for electron pairs in different layers.

This comparison with non-relativistic 2D electrons in bilayer systems indicates that there may exist a close relation between the quantum Hall ferromagnetism and the scenario of the magnetic catalysis also in graphene in a strong magnetic field. Notice, however, that the excitonic

state in graphene is not in the same universality class as that of the quantum-Hall bilayer – in the latter case the symmetry of the (interaction) Hamiltonian is U(1) as a consequence of the easy-plane anisotropy, and the symmetry breaking is associated with a superfluid mode that disperses linearly with the wave vector,  $\omega \propto q$ . In contrast to this system, the interaction Hamiltonian (207) has the full SU(4) symmetry, and even for a sufficiently strong Zeeman effect, the symmetry is quite large with  $\text{SU}(2)_\uparrow \times \text{SU}(2)_\downarrow$ , i.e. each spin projection  $\uparrow$  and  $\downarrow$  is governed by the residual SU(2) valley symmetry and has the characteristic  $\omega \propto q^2$  pseudospin-wave modes.

The connection between the two scenarios becomes transparent within a mean-field treatment of the Coulomb interaction Hamiltonian. The quantum Hall ferromagnetic states discussed in the previous subsections may be described equivalently with the help of the mean-field order parameters

$$\langle \Psi^\dagger \left( \tau_{\text{valley}}^\nu \otimes \mathbb{1}_{AB} \otimes \tau_{\text{spin}}^\mu \right) \Psi \rangle, \quad (241)$$

where  $\Psi$  denotes the same eight-spinor as in Sec. V.A.4. Remember that a pure spin quantum Hall ferromagnet is obtained for  $\tau_{\text{valley}}^\nu = \mathbb{1}_{\text{valley}}$ , whereas a pure valley-pseudospin ferromagnet is described by an order parameter (241) with  $\tau_{\text{spin}}^\mu = \mathbb{1}_{\text{spin}}$ . The remaining order parameters describe states with a certain degree of spin-valley entanglement, as discussed above.

Notice, however, that the choice of order parameters is not restricted to those in Eq. (241). Indeed, one may also opt for a mean-field calculation of the interaction Hamiltonian with the order parameters (Gorbar *et al.*, 2008; Gusynin *et al.*, 2006)

$$\mathcal{M}_s = \langle \Psi^\dagger \left( \tau_{\text{valley}}^z \otimes \tau_{AB}^z \otimes \mathbb{1}_{\text{spin}} \right) \Psi \rangle \quad (242)$$

and

$$\mathcal{M}_t = \langle \Psi^\dagger \left( \mathbb{1}_{\text{valley}} \otimes \tau_{AB}^z \otimes \mathbb{1}_{\text{spin}} \right) \Psi \rangle, \quad (243)$$

which describe mass gaps. Indeed, we already encountered a term of the form (243) in Sec. V.A.4 and showed that it lifts the valley degeneracy of the  $n = 0$  LL. Whereas such a term arises naturally in the context of an out-of-plane distortion of the graphene lattice, here, it is generated dynamically via the repulsive electron-electron interaction. The difference between the two mass terms  $\mathcal{M}_s$  and  $\mathcal{M}_t$  stems from the residual symmetry of the  $\text{SU}(2)_\sigma$  groups. The term (242), which may be viewed as a *singlet mass term* explicitly breaks this symmetry, whereas the term (243) has been coined *triplet mass* (Gorbar *et al.*, 2008; Gusynin *et al.*, 2006).

In Sec. V.A.4, we have argued that mass terms of the above form only lift the valley degeneracy in the zero-energy LL  $n = 0$ , whereas they simply renormalize the LL energy for  $n \neq 0$ . Furthermore we have seen that as a consequence of the vanishing spinor components  $\psi_{K,\sigma}^A$  and  $\psi_{K',\sigma}^B$ , the mass term  $\mathcal{M}_t$  is indistinguishable, in

$n = 0$ , from a valley-pseudospin ferromagnetic state,

$$\begin{aligned} \mathcal{M}_t^{n=0} &= \langle \Psi^\dagger (\mathbb{1}_{\text{valley}} \otimes \tau_{AB}^z \otimes \mathbb{1}_{\text{spin}}) \Psi \rangle \\ &\sim \langle \Psi^\dagger (\tau_{\text{valley}}^z \otimes \mathbb{1}_{AB} \otimes \mathbb{1}_{\text{spin}}) \Psi \rangle, \end{aligned} \quad (244)$$

whereas the singlet mass term simply renormalizes the overall chemical potential,

$$\begin{aligned} \mathcal{M}_s^{n=0} &= \langle \Psi^\dagger (\tau_{\text{valley}}^z \otimes \tau_{AB}^z \otimes \mathbb{1}_{\text{spin}}) \Psi \rangle \\ &\sim \langle \Psi^\dagger (\mathbb{1}_{\text{valley}} \otimes \mathbb{1}_{AB} \otimes \mathbb{1}_{\text{spin}}) \Psi \rangle. \end{aligned} \quad (245)$$

These arguments lead to the conclusion that the magnetic catalysis in  $n = 0$ , i.e. the spontaneous generation of a mass gap due to electron-electron interactions, may be fully described in the framework of the SU(4) quantum Hall ferromagnetism. Furthermore, the recent observation of a fully lifted spin-valley degeneracy in the  $n = 1$  graphene LL (Dean *et al.*, 2011) is naturally understood in the framework of quantum Hall ferromagnetism, whereas the mass terms (242) and (243), obtained from magnetic catalysis, would not provide a fully lifted spin-valley degeneracy.

#### 4. The quantum Hall effect at $\nu = \pm 1$ and $\nu = 0$

Before discussing the experimental results on the quantum Hall effect, a clarification on the filling factor is required. In the preceding parts of this section, which were concerned with general aspects of the quantum Hall ferromagnet in LLs with internal degrees of freedom, the filling factor  $\nu = k$  has been defined with respect to the *bottom* of the partially filled LL. However, in graphene, this is at odds with the natural definition of the filling factor (101) in terms of the electronic density measured from the charge neutrality point in undoped graphene – a zero filling factor therefore corresponds to *two* completely filled spin-valley subbranches ( $k = 2$ ) of the  $n = 0$  LL. In the remainder of this section, we therefore make a clear distinction between the two filling factors, and  $\nu$  denotes the filling of the  $n = 0$  LL measured from the bottom of the level, whereas the *natural* filling factor (101) is from now on denoted by  $\nu_G$ . Explicitly, the relation between the two filling factors reads

$$\nu = \nu_G + 2. \quad (246)$$

Early transport measurements in exfoliated graphene on a SiO<sub>2</sub> have revealed broken spin-valley-symmetry states at  $\nu_G = 0, \pm 1$  and  $\pm 4$  (Jiang *et al.*, 2007b; Zhang *et al.*, 2006), where the latter corresponds to the LLs  $\pm 1$ . More recent experiments on exfoliated graphene on a h-BN substrate have furthermore revealed quantum Hall states at  $\nu_G = \pm 3$  (Dean *et al.*, 2011), thus completing the full resolution of the spin-valley quartet, not only in  $n = 0$ , but also in  $\pm 1$ .

The observed states may generally be understood in the framework of the quantum Hall ferromagnetism, but the understanding of the situation at  $\nu_G = 0$  requires

an additional consideration of the subleading external symmetry-breaking terms discussed in Sec. V.A.4. The two-stage picture, which we adopt here based on the above discussions, may be summarized as follows. (a) The quantum Hall ferromagnetic states are formed to minimize the leading energy given by the Coulomb interaction. However, because of the (approximate) SU(4) symmetry of the interaction, the orientation of the quantum Hall ferromagnets is not fixed – a polarization in the spin channel is as probable as one in the valley channel, and this yields the high degeneracy of the Goldstone modes described in Sec. V.B.1. (b) Therefore, in spite of the small energy scale of the external fields, the latter are relevant for the orientation of the ferromagnets and for the degeneracy lifting of the Goldstone modes.

*a. The quantum Hall effect at  $\nu_G = \pm 1$ .* For  $\nu_G = -1$ , only one spin-valley branch is completely filled by electrons.<sup>35</sup> The Zeeman effect would give a small energetic advantage to spin- $\downarrow$  electrons, such that the two spin Goldstone modes associated with collective excitations to the spin- $\uparrow$  acquire a  $q = 0$  gap, given by  $\Delta_Z$ . In contrast to the spin excitations, the Goldstone mode, which couples the two valleys in the spin- $\downarrow$  branch of  $n = 0$ , remains gapless, and the ground state may thus be viewed as a valley-pseudospin ferromagnet in the spin- $\downarrow$  branch. The activation gap would be given by Eq. (233) for pseudospin skyrmion–anti-skyrmion pairs, and its associated scaling  $e^2/\epsilon l_B \propto \sqrt{B}$  has indeed been observed experimentally (Jiang *et al.*, 2007b). The residual valley SU(2) symmetry may be broken by the lattice distortions, which we have discussed in Sec. V.A.4. Whereas an out-of-plane lattice distortion would yield a gapped valley-pseudospin-wave mode, a Kekulé-type in-plane distortion orients the pseudospin ferromagnet in the XY-plane, associated with a gapless U(1) superfluid mode (Nomura *et al.*, 2009). Notice that the lattice distortion, characterized by the energy scale  $\Delta_{kek}$  is not in competition, at  $\nu_G = \pm 1$ , with the Zeeman effect, such that the resulting ferromagnetic state is the same for  $\Delta_Z > \Delta_{kek}$  as for  $\Delta_Z < \Delta_{kek}$ . In the remainder of this section we restrict the discussion of the valley-pseudospin degeneracy lifting to in-plane distortions that seem to be energetically more relevant than out-of-plane distortions, but the overall picture remains unchanged if the latter are more relevant.

*b. The quantum Hall effect at  $\nu_G = 0$ .* The situation is more subtle at  $\nu_G = 0$ , where it is not possible to fully polarize both the spin and the valley pseudospin and where the Zeeman effect is in competition with a lattice distortion.

<sup>35</sup> For  $\nu_G = +1$ , the same arguments apply in terms of holes due to particle-hole symmetry.

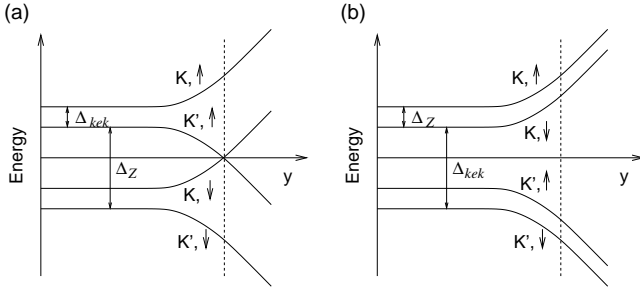


Figure 27 Possible scenarios for the lifted spin-valley degeneracy at  $\nu_G = 0$ . (a)  $\Delta_Z > \Delta_{kek}$  in the bulk. When approaching the edge, the energy difference between the two valleys increases drastically, and two levels ( $K', \uparrow$ ) and ( $K, \downarrow$ ) cross the Fermi energy at the edge depicted by the dashed line (Quantum Hall state). (b)  $\Delta_{kek} > \Delta_Z$  in the bulk. The  $K$  subbranches are already located above the Fermi energy, and those of  $K'$  below, such that the energy difference is simply increased when approaching the edge with no states crossing the Fermi energy (Insulator).

tion that orients the valley pseudospin. For  $\Delta_Z > \Delta_{kek}$ , it is favorable to fill both valley sublevels of the spin- $\downarrow$  branch and the resulting state is a spin ferromagnet with gapped spin-wave excitations. For  $\Delta_Z < \Delta_{kek}$ , a pseudospin-ferromagnetic ground state is favored with both spin sublevels completely filled. The two different situations are depicted in Fig. 27. Most saliently, the two phases reveal drastically different transport properties as one may see from their behavior at the sample edges.

The electronic behavior at the edges may be described within a model of electron confinement, in which the sample edge is described via a *mass* confinement term  $M(y)\tau_{AB}^z$  in the Hamiltonian, which has the symmetry of the term (218) or else, in  $n = 0$ , that of a valley-Zeeman term (217), as argued in Sec. V.A.4. The parameter  $M(y)$  is zero in the bulk and increases drastically at the edge at a certain value of the coordinate  $y$ .<sup>36</sup> Although the model is a simplification to treat the graphene edges in the continuum description of the Dirac equation, a more sophisticated treatment that takes into account the geometry of the edges yields, apart from a fine structure of the levels at the edge, qualitatively similar results (Brey and Fertig, 2006). The mass term  $M(y)$  modifies the valley coupling due to the lattice distortion and yields a  $y$ -dependent term  $\sqrt{\Delta_{kek}^2 + M(y)^2}$ , which therefore equally diverges at the sample edge.<sup>37</sup>

These preliminary considerations on the gap behavior at the edges allow us to appreciate the difference in the expected electronic transport between a spin ferromagnet and a valley-pseudospin ferromagnet at  $\nu_G = 0$ . Indeed, for  $\Delta_Z > \Delta_{kek}$ , one obtains a quantum Hall

state at  $\nu_G = 0$  that is characterized by a bulk gap associated with two counter-propagating edge states [Fig. 27(a)]. In the bulk, where  $M(y) = 0$ , both valley sublevels of the spin- $\downarrow$  branch are filled (spin ferromagnet). When approaching the edge, however, the energy term  $\sqrt{\Delta_{kek}^2 + M(y)^2}$  is enhanced by the rapidly increasing contribution from  $M(y)$ , and the ( $K, \uparrow$ ) level eventually crosses the ( $K', \downarrow$ ) one at the edge at the Fermi energy (Abanin *et al.*, 2007b). This situation corresponds to a quantum Hall state with a bulk insulator and (two counter-propagating) conducting channels. In contrast to usual quantum Hall states, the edge states are not chiral, but the chirality, i.e. the transport direction, of each channel is linked to its spin orientation.<sup>38</sup> The quantum Hall state therefore remains stable unless magnetic impurities couple the two chiralities (Shimshoni *et al.*, 2009). One notices furthermore a change in the spin polarization at the edge; whereas the spin polarization in the bulk is complete, the system becomes spin unpolarized at the edge. If one takes into account the exchange interaction, the change in the polarization takes place over a certain distance, and the conducting properties may be described in terms of spin-carrying one-dimensional edge excitations (Shimshoni *et al.*, 2009).

In the opposite limit with  $\Delta_Z < \Delta_{kek}$  in the bulk [Fig. 27(b)], the system at  $\nu_G = 0$  is already valley-polarized, and an increase of  $\sqrt{\Delta_{kek}^2 + M(y)^2}$  when approaching the edge does not induce a level crossing at the Fermi energy. Thus, there are no zero-energy states at the edge, and the system would be insulating both in the bulk and at the edge.

From an experimental point of view, it is not fully settled which of the two phases describes the state at  $\nu_G = 0$ . Whereas early experiments in exfoliated graphene on  $\text{SiO}_2$  samples were discussed in the framework of a dominant Zeeman effect (Abanin *et al.*, 2007b; Jiang *et al.*, 2007b; Zhang *et al.*, 2006), more recent experiments at very large magnetic fields (Checkelsky *et al.*, 2008, 2009) and on suspended graphene samples with increasing mobility (Du *et al.*, 2009) favor the insulating scenario of Fig. 27(b) with a dominant valley degeneracy lifting. Especially the high-field measurements hint at an easy-plane or  $XY$  (valley-pseudospin) ferromagnetic ground state because the transition between the metallic and the insulating state is reminiscent of a Kosterlitz-Thouless phase transition (Kosterlitz and Thouless, 1973) if one replaces the temperature by the magnetic field as the parameter driving the transition (Checkelsky *et al.*, 2008, 2009; Hou *et al.*, 2010; Nomura *et al.*, 2009). However, it has also been argued that this effect may be understood within the above scenario of a Zeeman-dominated quantum Hall ferromagnet in the bulk, in the framework of a Luttinger-liquid description of the domain wall separat-

<sup>36</sup> For the present argument, we consider translation invariance in the  $x$ -direction.

<sup>37</sup> In the case of an out-of-plane distortion, the term  $M(y)$  simply adds up to the energy scale  $\Delta_Z^{\text{valley}}$  [see Eq. (217)], but the physical picture remains unaltered.

<sup>38</sup> These helical edges are the signature of a quantum spin Hall effect (Hasan and Kane, 2010; Qi and Zhang, 2011).

ing the polarized from the unpolarized region at the edge (Shimshoni *et al.*, 2009).

One notices that both the Zeeman effect and the Kekulé-type lattice distortion are very close in energy (see Tab. II) such that one may speculate that other effects, as e.g. impurities, strongly influence the formation and the orientation of the quantum Hall ferromagnet. Further experimental and theoretical studies therefore seem to be necessary to clearly identify the leading symmetry-breaking mechanisms, which need not be universal, in the zero-energy LL at  $\nu_G = 0$  and  $\pm 1$ .

We finally mention scanning-tunneling spectroscopic results for the level splitting at  $\nu_G = 0$  that were performed on graphene on a graphite substrate (Li *et al.*, 2009a). Although a gap has been observed as one may expect in the framework of the above scenario, it saturates as a function of the magnetic field. This is in disagreement with both the  $\sqrt{B}$ -behavior of an interaction-dominated gap as well as with the linear dependence of the Zeeman or lattice-distortion effects. A probable origin of this gap is the commensurability of the graphene lattice with the graphite substrate that may break the inversion symmetry between the two sublattices by a term of the type (218). The coupling to the substrate being essentially electrostatic, one would then expect no or only a weak magnetic-field dependence of the splitting, as observed in the experiment (Li *et al.*, 2009a).

### C. Fractional Quantum Hall Effect in Graphene

The most salient aspect of strongly-correlated 2D electrons in partially filled LLs is certainly the FQHE, which is due to the formation of incompressible liquid phases at certain *magical* values of the filling factor. As we have already argued in Sec. V.A.3 on the basis of the pseudopotentials, the FQHE is expected to be present in the graphene LLs  $n = 0$  and  $n = 1$ , and the main difference with respect to non-relativistic 2D electron systems should arise from the internal SU(4) symmetry [for a recent theoretical review see Ref. (Papić *et al.*, 2009)].

On the experimental level, recent progress in the fabrication of high-mobility samples, e.g. via current annealing (Bolotin *et al.*, 2008; Du *et al.*, 2008), has allowed for the observation of several FQHE states in graphene. The first observations of a state at  $\nu_G = \pm 1/3$  were reported in 2009 on current-annealed suspended graphene samples in the two-terminal configuration (Bolotin *et al.*, 2009; Du *et al.*, 2009).<sup>39</sup> More recently, in 2010, the FQHE has also been observed in the four-terminal geometry, which allows for the simultaneous measurement of the longitudinal and the Hall resistance, in suspended graphene (Ghahari *et al.*, 2011) and on graphene on a h-BN sub-

strate (Dean *et al.*, 2011).

Before commenting in more detail on these first experimental results (indeed, this part of graphene research has just started), we introduce the theoretical four-component or SU(4) picture of the FQHE in graphene, in terms of generalized Halperin wave functions. These wave functions, which may be viewed as multi-component generalizations of Laughlin's wave function, provide the natural framework for the description of the phenomenon in view of the model of electrons restricted to a single relativistic LL (Sec. V.A)

#### 1. Generalized Halperin wave functions

The theoretical study of the FQHE is intimately related to trial  $N$ -particle wave functions. In 1983, Laughlin proposed a one-component wave function (Laughlin, 1983),

$$\phi_m^L(\{z_k\}) = \prod_{k < l}^N (z_k - z_l)^m e^{-\sum_k^N |z_k|^2/2}, \quad (247)$$

which allows for an understanding of incompressible FQHE states at the filling factors  $\nu = 1/m$  that are determined by the exponent  $m$  for the particle pairs  $k, l$  in Eq. (247). The variable  $z_k = (x_k - iy_k)/l_B$  is the complex position of the  $k$ -th particle, and the form of the Laughlin wave function (247) is dictated by the analyticity condition for wave functions in the lowest LL.<sup>40</sup> Furthermore, the exponent  $m$  must be an odd integer as a consequence of the fermionic statistics imposed on the electronic wave function. Even if Eq. (247) describes only a trial wave function, one can show that it is the *exact* ground state for a class of model interactions that yield, with the help of Eq. (215), the pseudopotentials (Haldane, 1983)

$$V_\ell > 0 \text{ for } \ell < m \quad \text{and} \quad V_\ell = 0 \text{ for } \ell \geq m. \quad (248)$$

Although the Coulomb interaction does not fulfill such strong conditions, the pseudopotentials decrease as  $1/\sqrt{m}$  for large values of  $m$ . Because the incompressible ground state is protected by a gap that is on the order of  $V_1$ , one may view the pseudopotentials  $V_{\ell \geq m}$  as an irrelevant perturbation that does not change the nature of the ground state. Indeed, exact-diagonalization calculations have shown that, for the most prominent FQHE at  $\nu = 1/3$ , the overlap between the true ground state and the Laughlin state (247) is extremely large ( $> 99\%$ ) (Fano *et al.*, 1986; Haldane and Rezayi, 1985).

Soon after Laughlin's original proposal, Halperin generalized the wave function (247) to the SU(2) case of

<sup>39</sup> There are also some weak indications for FQHE states at other filling factors than  $\nu_G = \pm 1/3$  in these samples.

<sup>40</sup> The lowest-LL condition of analytic wave functions may seem a very strong restriction when discussing FQHE states in higher LLs. However, the model (207) indicates that all LLs can be treated as the lowest one,  $n = 0$ , if the interaction potential is accordingly modified. We adopt this point of view here.



electrons with spin, in the absence of a Zeeman effect (Halperin, 1983) – one has then two classes of particles,  $N_\uparrow$  spin- $\uparrow$  and  $N_\downarrow$  spin- $\downarrow$  particles, which are described by the complex positions  $z_{k_\uparrow}^{(\uparrow)}$  and  $z_{k_\downarrow}^{(\downarrow)}$ , respectively. In the (theoretical) absence of interactions between electrons with different spin orientation, the most natural ground-state candidate would then be a simple product of two Laughlin wave functions (247),

$$\phi_{m_\uparrow}^L \left( \left\{ z_{k_\uparrow}^{(\uparrow)} \right\} \right) \phi_{m_\downarrow}^L \left( \left\{ z_{k_\downarrow}^{(\downarrow)} \right\} \right), \quad (249)$$

one for each spin component with the exponents  $m_\uparrow$  and  $m_\downarrow$ , respectively, that need not necessarily be identical. Inter-component correlations may be taken into account by an additional factor

$$\prod_{k_\uparrow}^{N_\uparrow} \prod_{k_\downarrow}^{N_\downarrow} \left( z_{k_\uparrow}^{(\uparrow)} - z_{k_\downarrow}^{(\downarrow)} \right)^n, \quad (250)$$

where the exponent  $n$  can now also be an even integer because the fermionic anti-symmetry condition is concerned only with electrons in the same spin state.

Halperin's idea is easily generalized to the case of more than two components, and the corresponding trial wave function for an  $SU(\mathcal{N})$  quantum Hall system with  $\mathcal{N}$  components reads (Goerbig and Regnault, 2007)

$$\psi_{m_1, \dots, m_{\mathcal{N}}; n_{ij}}^{SU(\mathcal{N})} = \phi_{m_1, \dots, m_{\mathcal{N}}}^L \phi_{n_{ij}}^{inter}, \quad (251)$$

in terms of the product

$$\phi_{m_1, \dots, m_{\mathcal{N}}}^L = \prod_{j=1}^{\mathcal{N}} \prod_{k_j < l_j}^{N_j} \left( z_{k_j}^{(j)} - z_{l_j}^{(j)} \right)^{m_j} e^{-\sum_{j=1}^{\mathcal{N}} \sum_{k_j=1}^{N_j} |z_{k_j}^{(j)}|^2 / 4} \quad (252)$$

of  $\mathcal{N}$  Laughlin wave functions and the term

$$\phi_{n_{ij}}^{inter} = \prod_{i < j}^{\mathcal{N}} \prod_{k_i}^{N_i} \prod_{k_j}^{N_j} \left( z_{k_i}^{(i)} - z_{k_j}^{(j)} \right)^{n_{ij}}, \quad (253)$$

which describes inter-component correlations. As in the case of Halperin's two-component wave function (Halperin, 1983), the exponents  $m_j$  must be odd integers for fermionic particles whereas the exponents  $n_{ij}$  may also be even integers. These exponents define a symmetric  $\mathcal{N} \times \mathcal{N}$  matrix  $M = n_{ij}$ , where the diagonal elements are  $n_{ii} \equiv m_i$ . This exponent matrix encodes the statistical properties of the quasi-particle excitations, such as their (fractional) charge and their statistical angle (Wen and Zee, 1992a,b).

Moreover, the exponent matrix  $M$  determines the component densities  $\rho_j$  – or, equivalently, the component filling factors  $\nu_j = \rho_j / n_B$ ,

$$\begin{pmatrix} \nu_1 \\ \vdots \\ \nu_{\mathcal{N}} \end{pmatrix} = M^{-1} \begin{pmatrix} 1 \\ \vdots \\ 1 \end{pmatrix}, \quad (254)$$

where  $\nu = \nu_1 + \dots + \nu_{\mathcal{N}}$  is the total filling factor measured from the bottom of the lowest LL. Notice that Eq. (254) is only well-defined if the exponent matrix  $M$  is invertible. In this case, all component filling factors  $\nu_j$  are completely determined, whereas otherwise some of the component fillings remain unfixed, e.g.  $\nu_1$  and  $\nu_2$  for the sake of illustration, although the sum of them ( $\nu_1 + \nu_2$ ) is fixed. This is nothing other than a consequence of the underlying ferromagnetic properties of the FQHE state that, similarly to the states at  $\nu = k$  discussed in Sec. V.B, are described by subgroups of  $SU(\mathcal{N})$ .

Finally, we notice that not all  $SU(\mathcal{N})$  wave functions (251) describe incompressible quantum liquids with a homogeneous charge density for all components. A generalization of Laughlin's plasma picture, according to which the modulus square of the trial wave function corresponds to the Boltzmann weight of a classical 2D plasma (Laughlin, 1983), shows that all eigenvalues of the exponent matrix  $M$  must be positive (or zero for states with ferromagnetic order). Otherwise, some of the different components phase-separate in the 2D plane because the inter-component repulsion between them exceeds the intra-component repulsion (de Gail *et al.*, 2008).

## 2. The use of generalized Halperin wave functions in graphene

These general considerations allow us to define the framework for a basic description of the FQHE in graphene where the  $SU(4)$  spin-valley symmetry imposes  $\mathcal{N} = 4$ . Four-component Halperin wave functions are therefore expected to play an equally central role in the description of the graphene FQHE as Laughlin's in a one-component or Halperin's in two-component systems. In the remainder of this section, we attribute the four spin-valley components as 1 = ( $\uparrow, K$ ), 2 = ( $\uparrow, K'$ ), 3 = ( $\downarrow, K$ ), and 4 = ( $\downarrow, K'$ ).

*a. Fractional  $SU(4)$  quantum Hall ferromagnet.* In a first step, we consider a four-component Halperin wave function in which all components are equal (odd) integers,  $m_j = n_{ij} = m$ , regardless of whether they describe intra- or inter-component correlations. One obtains then a completely anti-symmetric orbital wave function that is accompanied by a fully symmetric  $SU(4)$  spin-valley wave function.

As we have argued in Sec. V.B.1, this situation represents precisely a perfect  $SU(4)$  quantum Hall ferromagnet – indeed, for  $m = 1$ , the generalized Halperin wave function (251) is nothing other than the orbital wave function of the state at  $\nu = 1$ , i.e. when one of the subbranches is completely filled. The  $SU(4)$  symmetry is then spontaneously broken, and the group-theoretical analysis presented in Sec. V.B.1 yields 3 degenerate Goldstone modes that are generalized spin waves.

The situation is exactly the same for any other odd exponent  $m$ , but the orbital wave function (251) is then

a Laughlin wave function (247) in terms of the particle positions  $z_k$  regardless of their internal index  $j = 1, \dots, 4$ . The ferromagnetic properties of these wave functions may be described by the same equations as the spin-wave and skyrmion modes derived in Sec. V.B if one takes into account a renormalization of the spin stiffness, as it has been discussed extensively in the literature for SU(2) quantum Hall ferromagnets (Ezawa, 2000; Moon *et al.*, 1995; Sondhi *et al.*, 1993). States described by such a wave function are ground-state candidates for the filling factors  $\nu = 1/m$ , which correspond to the graphene filling factors [see Eq. (246)]  $\nu_G = -2 + 1/m$  or hole states at  $\nu_G = 2 - 1/m$ .

There are now two different manners to break the internal SU(4) symmetry explicitly. The simplest one is the same as for the quantum Hall ferromagnetism at  $\nu_G = 0$  or  $\pm 1$ , in terms of external symmetry-breaking fields such as those discussed in Sec. V.A.4. However, one may also change some of the exponents in the generalized Halperin wave function (251), in which case one also changes the filling factor. One may for instance consider the  $[m; m-1, m]$  wave function with  $m_j = m$  for all  $j$ ,  $n_{13} = n_{24} = m-1$ , and  $n_{12} = n_{14} = n_{23} = n_{34} = m$ , which correspond to a filling factor<sup>41</sup>

$$\nu = \frac{2}{2m-1} \quad \text{or} \quad \nu_G = -2 + \frac{2}{2m-1}. \quad (255)$$

Indeed, the difference in the inter-component exponents explicitly breaks the spin-valley symmetry – electrons in different valleys are more weakly correlated (with an exponent  $m-1$ ) than electrons in the same valley (exponent  $m$ ), regardless of their spin orientation. As a consequence, the filling factors in each of the two valleys,  $\nu_K = \nu_1 + \nu_3$  and  $\nu_{K'} = \nu_2 + \nu_4$ , respectively, are fixed,  $\nu_K = \nu_{K'} = 1/(2m-1)$ , and one may view the wave function as a state with ferromagnetic spin ordering, but that is valley-pseudospin unpolarized. Alternatively, the  $[m; m-1, m]$  wave function may be interpreted as a tensor product of an SU(2) Halperin  $(m, m, m-1)$  pseudospin-singlet wavefunction (Halperin, 1983) and a completely symmetric (ferromagnetic) two-spinor that describes the physical spin. The relevance of the  $[m; m-1, m]$  wave function, with  $m = 3$  ( $\nu = 2/5$ ) has been corroborated in recent exact-diagonalization studies, both in the graphene LLs  $n = 0$  and  $n = 1$  (Papić *et al.*, 2009; Töke and Jain, 2007).

The SU(4) spin-valley symmetry is fully broken, e.g., in the case of the  $[m; m-1, m-1]$  wave function with all  $m_j = m$  and off-diagonal  $n_{ij} = m-1$ . This wave function, which describes a state at

$$\nu = \frac{4}{4m-3} \quad \text{or} \quad \nu_G = -2 + \frac{4}{4m-3}, \quad (256)$$

<sup>41</sup> We only discuss electronic states here, but the arguments are equally valid for the particle-hole symmetric states at  $\nu_G = 2 - 1/(2m-1)$ .

may be viewed as an SU(4) singlet where the filling factors of all spin-valley components are  $1/(4m-3)$ . Exact-diagonalization calculations for  $N = 4$  and 8 particles have shown that the  $[m; m-1, m-1]$  wave function with  $m = 3$  (at  $\nu = 4/9$ ) describes to great accuracy the ground state for a Coulomb interaction (205), with overlaps  $\mathcal{O}_{N=8} = 0.992$  in  $n = 0$  and  $\mathcal{O}_{N=8} = 0.944$  and in the  $n = 1$  graphene LL (Papić *et al.*, 2009).

*b. A route to understanding the graphene FQHE at  $\nu_G = \pm 1/3$ .* The discussion of the above-mentioned states was based on the understanding acquired from quantum Hall systems in semiconductor heterostructures, where the filling factor is defined with respect to the bottom of the  $n = 0$  LL. First experimental observations, however, indicated a prominent FQHE at  $\nu_G = \pm 1/3$ , which corresponds to two completely filled spin-valley sublevels of the graphene  $n = 0$  LL, and a third one that is  $1/3$  filled,  $\nu = 2 + 1/3$ . Such a state would naturally arise in a system where the SU(4) symmetry is strongly broken, e.g. by a strong Zeeman effect. However, as argued in Sec. V.A.4, these external fields are weak as compared to the leading interaction energy scale, and it is therefore natural to ask how such a state may arise from the interaction point of view in the framework of four-component Halperin wave functions.

A Halperin wave function that describes the above-mentioned situation is (Papić *et al.*, 2010)

$$\begin{aligned} \psi_{2+1/3} = & \prod_{\xi=K, K'} \prod_{i < j} \left( z_i^{\uparrow, \xi} - z_j^{\uparrow, \xi} \right)^3 \prod_{i, j} \left( z_i^{\uparrow, K} - z_j^{\uparrow, K'} \right)^3 \\ & \times \prod_{\xi=K, K'} \prod_{i < j} \left( z_i^{\downarrow, \xi} - z_j^{\downarrow, \xi} \right), \end{aligned} \quad (257)$$

or any permutation of the spin-valley components. One notices that this wave function implicitly breaks the SU(4) spin-valley symmetry and, moreover, is not an eigenstate of the full SU(4) pseudospin, such that it cannot describe the ground state in the total absence of an external symmetry-breaking field. However, exact-diagonalization calculations have shown that even a tiny external Zeeman field is capable to stabilize the state (257), which becomes the ground state for  $\Delta_Z^1 \simeq 0.01e^2/\epsilon l_B$  (Papić *et al.*, 2010). Furthermore, the state (257) possesses, in addition to the valley-pseudospin-wave Goldstone mode in the spin- $\uparrow$  branch, low-lying spin-flip excitations for moderately small Zeeman fields, even if the charge (activation) gap is the same as for the usual  $1/3$  Laughlin state. This particular interplay between the leading Coulomb energy and subordinate external spin-valley symmetry breaking terms, illustrated at the  $\nu_G = 1/3$  example, shows the complexity of the graphene FQHE, and further surprises may be expected in future experiments.

### 3. Experiments on the graphene FQHE

We terminate this section on the graphene FQHE with a short discussion of experimental observations in the light of the above-mentioned theoretical four-component picture.

*a. Two-terminal measurements.* In the first observations of the FQHE, the two-terminal configuration was used, where the voltage (and thus the resistance) is measured between the same two contacts used to drive the electric current through the sample (Bolotin *et al.*, 2009; Du *et al.*, 2009). In this two-terminal configuration, it is not possible to measure simultaneously the Hall and the longitudinal resistance. It is nevertheless possible to extract the Hall and the longitudinal conductivities from the two-terminal resistance with the help of a conformal mapping, as a consequence of the 2D nature of the quantum transport in these systems (Abanin and Levitov, 2008; Williams *et al.*, 2009). This technique has been applied to obtain insight into the longitudinal conductivity the expected activated behavior of which yields a rough estimate of the activation gap at  $\nu_G = 1/3$  ( $\Delta_{1/3} \sim 4.4$  K at  $B = 12$  T) (Abanin *et al.*, 2010), which is an order of magnitude smaller than the theoretically expected value (Apalkov and Chakraborty, 2006; Töke *et al.*, 2006).<sup>42</sup>

*b. Four-terminal measurements.* The activation gap of the  $1/3$  FQHE state has also been measured in suspended graphene in the four-terminal configuration, in which the longitudinal resistance can be measured directly and independently from the Hall resistance (Ghahari *et al.*, 2011). In this case, the activation gap has been estimated to be  $\Delta_{1/3} \sim 26...50$  K at  $B = 14$  T, a value that agrees reasonably well with the theoretically expected value (Apalkov and Chakraborty, 2006; Töke *et al.*, 2006) if one considers the energy scale  $e^2/\varepsilon\varepsilon_\infty l_B$ , which takes into account the RPA dielectric constant  $\varepsilon_\infty$  for graphene in vacuum (see Sec. III.B.4).

Finally, we would mention very recent high-field transport measurements in the four-terminal configuration on graphene on a h-BN substrate (Dean *et al.*, 2011). These experiments allowed for a clear identification of several states of the  $1/3$  family, at  $\nu_G = \pm 1/3, \pm 2/3$ , and  $\pm 4/3$  corresponding to the zero-energy LL  $n = 0$ , as well as at  $\nu_G = \pm 7/3, \pm 8/3, \pm 10/3$ , and  $\pm 11/3$  which reside in

the  $n = 1$  LL. The estimation of the activation gap at  $\nu_G = 4/3$  agrees again reasonably well with the theoretical expectation for the  $1/3$  state. The perhaps most salient (and unexpected) feature of the transport measurement is the absence (or extreme weakness) of the  $\nu_G = \pm 5/3$  representative of the  $1/3$  family, which would correspond to the Laughlin state ( $\nu = 1/3 \leftrightarrow \nu_G = -5/3$  and the corresponding hole state) with a full SU(4) spin-valley ferromagnetic order, as argued in Sec. V.C.2.

Whereas the absence of this state remains to be understood, these findings corroborate the theoretical four-component picture of the graphene FQHE. Indeed, it clearly shows that the SU(4) symmetry of the  $n = 0$  LL is essential because the only correspondence between the FQHE states is particle-hole symmetry that maps  $\nu_G \leftrightarrow -\nu_G$ . If the SU(4) symmetry were broken, e.g. by a sufficiently strong Zeeman effect, the only symmetry would be the valley-SU(2) symmetry in each spin branch of the  $n = 0$  LL, in which case there exist the further mappings  $-2 + \nu \leftrightarrow -\nu$  in the spin- $\downarrow$  branch and  $\nu \leftrightarrow 2 - \nu$  in the spin- $\uparrow$  branch. However, the (observed)  $\pm 1/3$  state would then be mapped on the (unobserved or extremely weak)  $\pm 5/3$  state, and the strong difference in the visibility between these two states is therefore difficult to understand. This is also the case if the SU(4) symmetry is fully broken by strong external spin and valley Zeeman fields, such that all spin-valley sublevels are completely resolved, and  $\pm 5/3$  would be mapped on  $\pm 4/3$ , in the same manner as  $\pm 1/3$  on  $\pm 2/3$ .

## VI. CONCLUSIONS AND OUTLOOK

We have reviewed the quantum-mechanical properties of relativistic 2D electrons in monolayer graphene exposed to a strong magnetic field. The main parts of this review are concerned with the role of electronic interactions in graphene LLs. Whereas we have argued that these interactions may be treated perturbatively in the regime of the relativistic (integer) quantum Hall effect (RQHE), they constitute the relevant energy scale in partially filled graphene LLs due to the quenching of the kinetic energy. This is reminiscent of partially filled LLs in non-relativistic 2D electron systems, and the most prominent consequence of this quenched kinetic energy and the macroscopic LL degeneracy is certainly the FQHE. The graphene FQHE is expected to be reminiscent of that of non-relativistic 2D electrons but it is governed by a larger internal degeneracy described to great accuracy by the SU(4) group. The experimental study of the FQHE in graphene is still in its infancy, and novel surprises may be expected. Only recently have been reported measurements in the four-terminal geometry which allow for an analysis of prominent characteristics of FQHE states, such as the activation gaps. In view of the generally accepted universality of the quantum Hall effect, it will certainly be interesting to make a systematic comparison with the activation gaps of related FQHE states in

<sup>42</sup> Notice that the theoretical estimates have been obtained within a simplified two-component model, with a completely frozen spin degree of freedom. In spite of this simplification, the above-mentioned exact-diagonalization calculations with an implemented SU(4) symmetry have shown that the charge gap, which is responsible for the activated behavior, coincides indeed with that obtained in the two-component model (Papić *et al.*, 2010).

conventional 2D electron gases with a parabolic band.

In the perturbative regime of the RQHE, the theoretical study of electron-electron interactions indicates the presence of fascinating novel collective modes, such as linear magneto-plasmons, that are particular to graphene and do not have a counterpart in non-relativistic 2D electron systems in a perpendicular magnetic field. Also the upper-hybrid mode, which is the magnetic-field counterpart of the usual 2D plasmon, is expected to behave in a particular manner in graphene as a consequence of the linear dispersion relation and the vanishing band mass. Whereas these studies are at present only theoretical, these collective modes may find an experimental verification in inelastic light-scattering measurements.

Similarly to the role of electron-electron interactions in the RQHE regime, the electron-phonon coupling yields exciting resonance phenomena in graphene in a strong magnetic field. The electron-phonon interaction in graphene LLs has been discussed in the framework of a perturbative approach. Indications for the magneto-phonon resonance, e.g., have recently been found in Raman spectroscopy of epitaxial graphene.

The present review has been limited to monolayer graphene, and it is definitely a reasonable research program to ask how the effects described here manifest themselves in bilayer graphene. For example, the particular collective excitations described in Sec. III have been attributed to the lack of equidistant LL spacing and the presence of two bands. Whereas bilayer graphene also consists of two (particle-hole-symmetric) bands in the low-energy regime, the approximate parabolicity there yields almost equidistant LLs. The presence of additional high-energy bands (in the 300 meV range) certainly also affects the plasmonic modes.

## Acknowledgments

I would like to express my deep gratitude to numerous collaborators without whom the realisation of this review would not have been possible. Above all, I must acknowledge the very fruitful long-term collaborations with Jean-Noël Fuchs, on electron-electron interactions in the IQHE regime and electron-phonon coupling, and with Nicolas Regnault on the FQHE in graphene. I would furthermore thank my collaborators Claire Berger, Raphaël de Gail, Benoît Douçot, Volodya Fal'ko, Clément Faugeras, Kostya Kechedzhi, Pascal Lederer, Roderich Moessner, Gilles Montambaux, Cristiane Morais Smith, Zlatko Papić, Frédéric Piéchon, Paulina Plochocka, Marek Potemski, Rafael Roldán, and Guangquan Wang. Many thanks also to my colleagues Hélène Bouchiat, Antonio Castro Neto, Jean-Noël Fuchs, Christian Glattli, Paco Guinea, Anuradha Jagannathan, Philip Kim, and Bernhard Wunsch for fruitful discussions and a careful reading of this review.

## Appendix A: Matrix Elements of the Density Operators

The matrix elements that intervene in the expression for the density operators (139) are of the form  $\langle n, m | \exp(-i\mathbf{q} \cdot \mathbf{r}) | n', m' \rangle$  and may be calculated with the help of the decomposition of the cyclotron variable  $\boldsymbol{\eta}$  and the guiding centre  $\mathbf{R}$  into the ladder operators  $\hat{a}$  and  $\hat{b}$ , respectively [see Eqs. (78), (91) and (94)]. We furthermore define the complex wave vectors  $q \equiv (q_x + iq_y)l_B$  and  $\bar{q} = (q_x - iq_y)l_B$ .<sup>43</sup> One finds

$$\begin{aligned} \langle n, m | e^{-i\mathbf{q} \cdot \mathbf{r}} | n', m' \rangle &= \langle m | e^{-i\mathbf{q} \cdot \mathbf{R}} | m' \rangle \otimes \langle n | e^{-i\mathbf{q} \cdot \boldsymbol{\eta}} | n' \rangle \\ &= \langle m | e^{-\frac{i}{\sqrt{2}}(q\hat{b}^\dagger + \bar{q}\hat{b})} | m' \rangle \quad (\text{A1}) \\ &\quad \otimes \langle n | e^{-\frac{i}{\sqrt{2}}(\bar{q}\hat{a}^\dagger + q\hat{a})} | n' \rangle. \end{aligned}$$

The two matrix elements may be simplified with the help of the Baker-Hausdorff formula  $\exp(A)\exp(B) = \exp(A+B)\exp([A, B]/2)$ , for the case  $[A, [A, B]] = [B, [A, B]] = 0$  (Cohen-Tannoudji *et al.*, 1973). The second matrix element thus becomes, for  $n \geq n'$

$$\begin{aligned} \langle n | e^{-i\mathbf{q} \cdot \boldsymbol{\eta}} | n' \rangle &= \langle n | e^{-\frac{i}{\sqrt{2}}(\bar{q}\hat{a}^\dagger + q\hat{a})} | n' \rangle \quad (\text{A2}) \\ &= e^{-|q|^2/4} \langle n | e^{-\frac{i}{\sqrt{2}}\bar{q}\hat{a}^\dagger} e^{-\frac{i}{\sqrt{2}}q\hat{a}} | n' \rangle \\ &= e^{-|q|^2/4} \sum_j \langle n | e^{-\frac{i}{\sqrt{2}}\bar{q}\hat{a}^\dagger} | j \rangle \langle j | e^{-\frac{i}{\sqrt{2}}q\hat{a}} | n' \rangle \\ &= e^{-|q|^2/4} \sqrt{\frac{n!}{n'}} \left( \frac{-i\bar{q}}{\sqrt{2}} \right)^{n-n'} \\ &\quad \times \sum_{j=0}^{n'} \frac{n!}{(n-j)!(n'-j)!j!} \left( -\frac{|q|^2}{2} \right)^{n'-j} \\ &= e^{-|q|^2/4} \sqrt{\frac{n!}{n'}} \left( \frac{-i\bar{q}}{\sqrt{2}} \right)^{n-n'} L_{n'-n}^{n-n'} \left( \frac{|q|^2}{2} \right), \end{aligned}$$

where we have used

$$\langle n | e^{-\frac{i}{\sqrt{2}}\bar{q}\hat{a}^\dagger} | j \rangle = \begin{cases} 0 & \text{for } j > n \\ \sqrt{\frac{n!}{j!}} \frac{1}{(n-j)!} \left( -\frac{i}{\sqrt{2}}\bar{q} \right)^{n-j} & \text{for } j \leq n \end{cases}$$

in the third line and the definition of the associated Laguerre polynomials (Gradshteyn and Ryzhik, 2000),

$$L_{n'-n}^{n-n'}(x) = \sum_{m=0}^{n'} \frac{n!}{(n'-m)!(n-n'+m)!} \frac{(-x)^m}{m!}.$$

<sup>43</sup> We use this notation solely in the present appendix. Throughout the main text,  $q$  denotes the modulus of the wave vector  $\mathbf{q}$ ,  $q = |\mathbf{q}|$ .

In the same manner, one obtains for  $m \geq m'$

$$\begin{aligned} \langle m | e^{-i\mathbf{q}\cdot\mathbf{R}} | m' \rangle &= \langle m | e^{-\frac{i}{\sqrt{2}}(q\hat{b}^\dagger + \bar{q}\hat{b})} | m' \rangle \\ &= e^{-|q|^2/4} \sqrt{\frac{m!}{m'}} \left( \frac{-iq}{\sqrt{2}} \right)^{m-m'} \\ &\quad \times L_{m'}^{m-m'} \left( \frac{|q|^2}{2} \right). \end{aligned} \quad (\text{A3})$$

With the help of the definition

$$\mathcal{G}_{n,n'}(q) \equiv \sqrt{\frac{n!}{n'}} \left( \frac{-iq}{\sqrt{2}} \right)^{n-n'} L_{n'}^{n-n'} \left( \frac{|q|^2}{2} \right),$$

one may rewrite the expressions without the conditions  $n \geq n'$  and  $m \geq m'$ ,

$$\begin{aligned} \langle n | e^{-i\mathbf{q}\cdot\boldsymbol{\eta}} | n' \rangle &= [\Theta(n-n')\mathcal{G}_{n,n'}(\bar{q}) \\ &\quad + \Theta(n'-n-1)\mathcal{G}_{n',n}(-q)] e^{-|q|^2/4} \end{aligned} \quad (\text{A4})$$

and

$$\begin{aligned} \langle m | e^{-i\mathbf{q}\cdot\mathbf{R}} | m' \rangle &= [\Theta(m-m')\mathcal{G}_{m,m'}(q) \\ &\quad + \Theta(m'-m-1)\mathcal{G}_{m',m}(-\bar{q})] e^{-|q|^2/4}. \end{aligned} \quad (\text{A5})$$

## References

- Abanin, D. A., P. A. Lee, and L. S. Levitov, 2007a, Phys. Rev. Lett. **98**, 156801.
- Abanin, D. A., and L. S. Levitov, 2008, Phys. Rev. B **78**, 035416.
- Abanin, D. A., K. S. Novoselov, U. Zeitler, P. A. Lee, A. K. Geim, and L. S. Levitov, 2007b, Phys. Rev. Lett. **98**, 196806.
- Abanin, D. A., I. Skachko, X. Du, E. Y. Andrei, and L. S. Levitov, 2010, Phys. Rev. B **81**, 115410.
- Abergel, D. S. L., V. Apalkov, J. Berashevich, K. Ziegler, and T. Chakraborty, 2010, Advances in Physics **59**, 261.
- Abergel, D. S. L., and V. I. Fal'ko, 2007, Phys. Rev. B **75**, 155430.
- Abramowitz, M., and I. Stegun, 1970, *Handbook of Mathematical Functions (9th Ed.)* (Dover Publications, Dover).
- Ajiki, H., and T. Ando, 1995, J. Phys. Soc. Jpn. **64**, 260.
- Aleiner, I. L., and L. I. Glazman, 1995, Phys. Rev. B **52**, 11296.
- Alicea, J., and M. P. A. Fisher, 2006, Phys. Rev. B **74**, 075422.
- Ando, T., 2006a, J. Phys. Soc. Jpn. **75**, 074716.
- Ando, T., 2006b, J. Phys. Soc. Jpn. **75**, 124701.
- Ando, T., 2007a, J. Phys. Soc. Jpn. **76**, 024712.
- Ando, T., 2007b, J. Phys. Soc. Jpn. **76**, 024712.
- Andrei, E. Y., G. Deville, D. C. Glatli, F. I. B. Williams, E. Paris, and B. Etienne, 1988, Phys. Rev. Lett. **60**, 2765.
- Apalkov, V. M., and T. Chakraborty, 2006, Phys. Rev. Lett. **97**, 126801.
- Arikawa, M., Y. Hatsugai, and H. Aoki, 2008, Phys. Rev. B **78**, 205401.
- Arovas, D. P., A. Karlhede, and D. Lilliehöök, 1999, Phys. Rev. B **59**, 13147.
- Banerjee, S., R. R. P. Singh, V. Pardo, and W. E. Pickett, 2009, Phys. Rev. Lett. **103**, 016402.
- Bena, C., and G. Montambaux, 2009, New J. Phys. **11**, 095003.
- Berger, C., Z. Song, T. Li, A. Y. Ogbazghi, R. Feng, Z. Dai, A. N. Marchenkov, E. H. Conrad, P. N. First, and W. A. de Heer, 2004, J. Phys. Chem. **108**, 19912.
- Berman, O., G. Gumbs, and Y. E. Lezovik, 2008, Phys. Rev. B **78**, 085401.
- Bolotin, K. I., F. Ghahari, M. D. Shulman, H. L. Stormer, and P. Kim, 2009, Nature **462**, 196.
- Bolotin, K. I., K. J. Sikes, Z. Jiang, M. Klima, G. Fudenberg, J. Hone, P. Kim, and H. L. Stormer, 2008, Solid State Commun. **146**, 351.
- Bostwick, A., T. Ohta, T. Seyller, K. Horn, and E. Rotenberg, 2007, Nat. Phys. **3**, 36.
- Brey, L., and H. Fertig, 2006, Phys. Rev. B **73**, 195408.
- Brey, L., H. A. Fertig, R. Côté, and A. H. MacDonald, 1995, Phys. Rev. Lett. **75**, 2562.
- Büttiker, M., 1992, *The Quantum Hall Effect in Open Conductors*, in M. Reed (Ed.) *Nanostructured Systems (Semiconductors and Semimetals)*, **35**, 191 (Academic Press, Boston).
- Bychkov, Y. A., and G. Martinez, 2008, Phys. Rev. B **77**, 125417.
- Castro Neto, A. H., and F. Guinea, 2007, Phys. Rev. B **75**, 045404.
- Castro Neto, A. H., F. Guinea, N. M. R. Peres, K. S. Novoselov, and A. K. Geim, 2009, Rev. Mod. Phys. **81**, 109.
- Checkelsky, J. G., L. Li, and N. P. Ong, 2008, Phys. Rev. Lett. **100**, 206801.
- Checkelsky, J. G., L. Li, and N. P. Ong, 2009, Phys. Rev. B **79**, 115434.
- Chiu, K. W., and J. J. Quinn, 1974, Phys. Rev. B **9**, 4724.
- Cohen-Tannoudji, C., B. Diu, and F. Lalöë, 1973, *Quantum Mechanics* (Hermann, Paris).
- Coleman, P., 2003, An.. Henri Poincaré **4**, S559.
- Cooper, K. B., M. P. Lilly, J. P. Eisenstein, L. N. Pfeiffer, and K. W. West, 1999, Phys. Rev. B **60**, R11285.
- Côté, R., D. B. Boisvert, J. Bourassa, M. Boissonneault, and H. A. Fertig, 2007, Phys. Rev. B **76**, 125320.
- Côté, R., J.-F. Jobidon, and H. A. Fertig, 2008, Phys. Rev. B **78**, 085309.
- Damascelli, A., 2004, Phys. Scripta **T109**, 61.
- de Gail, R., N. Regnault, and M. O. Goerbig, 2008, Phys. Rev. B **77**, 165310.
- Dean, C., A. Young, P. Cadden-Zimansky, L. Wang, H. Ren, K. Watanabe, T. Taniguchi, P. Kim, J. Hone, and K. Shepard, 2011, Nature Phys. **7**, 693.
- Dietl, P., F. Piéchon, and G. Montambaux, 2008, Phys. Rev. Lett. **98**, 236405.
- Dillon, R. O., I. L. Spain, and J. W. McClure, 1977, J. Phys. Chem. Solids **38**, 635.
- Doretto, R. L., and C. Morais Smith, 2007, Phys. Rev. B **76**, 195431.
- Douçot, B., M. O. Goerbig, P. Lederer, and R. Moessner, 2008, Phys. Rev. B **78**, 195327.
- Drut, J. E., and T. A. Lähde, 2009a, Phys. Rev. Lett. **102**, 026802.
- Drut, J. E., and T. A. Lähde, 2009b, Phys. Rev. B **79**, 165425.
- Du, R. R., D. C. Tsui, H. L. Stormer, L. N. Pfeiffer, K. W. Baldwin, and K. W. West, 1999, Solid State Comm. **109**, 389.
- Du, X., I. Skachko, A. Barker, and E. Y. Andrei, 2008, Nat. Nanotech. **3**, 491.

- Du, X., I. Skachko, F. Duerr, A. Luican, and E. Y. Andrei, 2009, *Nature* **462**, 192.
- Eisenstein, J. P., K. B. Cooper, L. N. Pfeiffer, and K. W. West, 2002, *Phys. Rev. Lett.* **88**, 076801.
- Esaki, K., M. Sato, M. Kohmoto, and B. I. Halperin, 2009, *Phys. Rev. B* **80**, 125405.
- Ezawa, M., 2007, *J. Phys. Soc. Jpn.* **76**, 094701.
- Ezawa, Z. F., 2000, *Quantum Hall Effects – Field Theoretical Approach and Related Topics* (World Scientific, Singapore).
- Ezawa, Z. F., and K. Hasebe, 2002, *Phys. Rev. B* **65**, 075311.
- Ezawa, Z. F., and A. Iwazaki, 1993, *Phys. Rev. B* **47**, 7295.
- Ezawa, Z. F., G. Tsitsishvili, and K. Hasebe, 2003, *Phys. Rev. B* **67**, 125314.
- Fano, G., F. Ortolani, and E. Colombo, 1986, *Phys. Rev. B* **34**, 2670.
- Farjam, M., and H. Rafii-Tabar, 2009, *Phys. Rev. B* **80**, 167401.
- Faugeras, C., M. Amado, P. Kossacki, M. Orlita, M. Sprinkle, C. Berger, W. A. de Heer, and M. Potemski, 2009, *Phys. Rev. Lett.* **103**, 186803.
- Ferrari, A. C., J. C. Meyer, V. Scardaci, C. Casiraghi, M. Lazzeri, F. Mauri, S. Piscanec, D. Jiang, K. S. Novoselov, S. Roth, and A. K. Geim, 2006, *Phys. Rev. Lett.* **97**, 187401.
- Fertig, H. A., 1989, *Phys. Rev. B* **40**, 1087.
- Fogler, M. M., A. A. Koulakov, and B. I. Shklovskii, 1996, *Phys. Rev. B* **54**, 1853.
- Fuchs, J.-N., and P. Lederer, 2007, *Phys. Rev. Lett.* **98**, 016803.
- Fukuda, Y. *et al.* (Super-Kamiokande Collaboration), 1998, *Phys. Rev. Lett.* **81**, 1562.
- Fukuyama, H., 1975, *Solid State Commun.* **17**, 1323.
- Gangadharaiyah, S., A. M. Farid, and E. G. Mishchenko, 2008, *Phys. Rev. Lett.* **100**, 166802.
- Geim, A. K., and K. S. Novoselov, 2007, *Nat. Materials* **6**, 183.
- Ghahari, F., Y. Zhao, P. Cadden-Zimansky, K. Bolotin, and P. Kim, 2011, *Phys. Rev. Lett.* **106**, 046801.
- Girvin, S. M., 1999, *The Quantum Hall Effect: Novel Excitations and Broken Symmetries*, in A. Comtet, T. Jolicœur, S. Ouvry and F. David (Eds.) *Topological Aspects of Low-Dimensional Systems – École d'Été de Physique Théorique LXIX* (Springer, Berlin).
- Girvin, S. M., A. H. MacDonald, and P. M. Platzman, 1986, *Phys. Rev. B* **33**, 2481.
- Giuliani, G. F., and G. Vignale, 2005, *Quantum Theory of Electron Liquids* (Cambridge UP, Cambridge).
- Goerbig, M. O., 2009, *Quantum Hall Effects* (Lecture notes of the Les Houches Summer School 2009 (Singapore Session), arXiv:0909.1998).
- Goerbig, M. O., B. Douçot, and R. Moessner, 2006, *Phys. Rev. B* **74**, 161407.
- Goerbig, M. O., J.-N. Fuchs, K. Kechedzhi, and V. I. Fal'ko, 2007, *Phys. Rev. Lett.* **99**, 087402.
- Goerbig, M. O., J.-N. Fuchs, G. Montambaux, and F. Piéchon, 2008, *Phys. Rev. B* **78**, 045415.
- Goerbig, M. O., J.-N. Fuchs, G. Montambaux, and F. Piéchon, 2009, *EPL* **85**, 57005.
- Goerbig, M. O., P. Lederer, and C. Morais Smith, 2003, *Phys. Rev. B* **68**, 241302.
- Goerbig, M. O., P. Lederer, and C. Morais Smith, 2004, *Phys. Rev. B* **69**, 115327.
- Goerbig, M. O., and N. Regnault, 2007, *Phys. Rev. B* **75**, 241405.
- González, J., F. Guinea, and M. A. H. Vozmediano, 1994, *Nucl. Phys. B* **424**, 595.
- González, J., F. Guinea, and M. A. H. Vozmediano, 1999, *Phys. Rev. B* **59**, R2474.
- Gorbar, E. V., V. P. Gusynin, V. A. Miransky, and I. A. Shovkovy, 2002, *Phys. Rev. B* **66**, 045108.
- Gorbar, E. V., V. P. Gusynin, V. A. Miransky, and I. A. Shovkovy, 2008, *Phys. Rev. B* **78**, 085437.
- Gradshteyn, I. S., and I. M. Ryzhik, 2000, *Table of Integrals, Series and Products (6th Ed.)* (Academic Press, San Diego).
- Graf, D., F. Molitor, K. Ensslin, C. Stampfer, A. Jungen, C. Hierold, and L. Wirtz, 2007, *Nano Lett.* **7**, 238.
- Greiter, M., X.-G. Wen, and F. Wilczek, 1991, *Phys. Rev. Lett.* **66**, 3205.
- Gupta, A., G. Chen, P. Joshi, S. Tadigadapa, and P. Eklund, 2006, *Nano Lett.* **6**, 2667.
- Gusynin, V. P., V. A. Miransky, S. G. Sharapov, and I. A. Shovkovy, 2006, *Phys. Rev. B* **74**, 195429.
- Gusynin, V. P., and S. G. Sharapov, 2005, *Phys. Rev. Lett.* **95**, 146801.
- Gusynin, V. P., and S. G. Sharapov, 2006, *Phys. Rev. B* **73**, 245411.
- Haldane, F. D. M., 1983, *Phys. Rev. Lett.* **51**, 605.
- Haldane, F. D. M., 1988, *Phys. Rev. Lett.* **61**, 2015.
- Haldane, F. D. M., and E. H. Rezayi, 1985, *Phys. Rev. Lett.* **54**, 237.
- Halperin, B. I., 1983, *Helv. Phys. Acta* **56**, 75.
- Harrison, W. A., 1981, *Phys. Rev. B* **24**, 5835.
- Hasan, M. Z., and C. L. Kane, 2010, *Rev. Mod. Phys.* **82**, 3045.
- Hasegawa, Y., R. Konno, H. Nakano, and M. Kohmoto, 2006, *Phys. Rev. B* **74**, 033413.
- de Heer, W. A., C. Berger, X. Wu, P. N. First, E. H. Conrad, X. B. Li, T. B. Li, M. Sprinkle, J. Hass, M. Sadowski, M. Potemski, and G. Martinez, 2007, *Solid State Comm.* **143**, 92.
- Herbut, I. F., 2006, *Phys. Rev. Lett.* **97**, 146401.
- Herbut, I. F., 2007a, *Phys. Rev. B* **76**, 085432.
- Herbut, I. F., 2007b, *Phys. Rev. B* **75**, 165411.
- Herbut, I. F., 2008, *Phys. Rev. B* **78**, 205433.
- Herbut, I. F., V. Juričić, and B. Roy, 2009a, *Phys. Rev. B* **79**, 085116.
- Herbut, I. F., V. Juričić, and O. Vafek, 2009b, *Phys. Rev. B* **80**, 075432.
- Hou, C.-Y., C. Chamon, and C. Mudry, 2010, *Phys. Rev. B* **81**, 075427.
- Hou, J.-M., W.-X. Yang, and X.-J. Liu, 2009, *Phys. Rev. A* **79**, 043621.
- Hwang, E. H., and S. Das Sarma, 2007, *Phys. Rev. B* **75**, 205418.
- Imry, Y., 1997, *Introduction to Mesoscopic Physics* (Oxford UP).
- Ishikawa, K., and T. Ando, 2006, *J. Phys. Soc. Jpn.* **75**, 084713.
- Iyengar, A., J. Wang, H. A. Fertig, and L. Brey, 2007, *Phys. Rev. B* **75**, 125430.
- Jackson, J. D., 1999, *Classical Electrodynamics* (Wiley, 3rd ed., New York).
- Jiang, Z., E. A. Henriksen, Y.-J. W. L. C. Tung, M. E. Schwartz, M. Y. Han, P. Kim, and H. L. Stormer, 2007a, *Phys. Rev. Lett.* **98**, 197403.
- Jiang, Z., Y. Zhang, H. L. Stormer, and P. Kim, 2007b, *Phys.*

- Rev. Lett. **99**, 106802.
- Jobst, J., D. Waldmann, F. Speck, R. Hirner, D. K. Maude, T. Seyller, and H. B. Weber, 2010, Phys. Rev. B **81**, 195434.
- Juričić, V., I. F. Herbut, and G. W. Semenoff, 2009, Phys. Rev. B **80**, 081405(R).
- Kallin, C., and B. I. Halperin, 1984, Phys. Rev. B **30**, 5655.
- Kane, C., and E. J. Mele, 2005, Phys. Rev. Lett. **95**, 226801.
- Katayama, S., A. Kobayashi, and Y. Suzumura, 2006, J. Phys. Soc. Jpn. **75**, 054705.
- Katsnelson, M., K. Novoselov, and A. Geim, 2006, Nat. Phys. **2**, 620.
- Katsnelson, M. I., 2006, Phys. Rev. B **74**, 201401.
- Kekulé, A., 1865, Bulletin de la Societe Chimique de Paris **3**, (2) 98.
- Kekulé, A., 1866, Annalen der Chemie und Pharmazie **137**, (2) 129.
- Kellogg, M., J. P. Eisenstein, and L. N. P. and K. W. West, 2004, Phys. Rev. Lett. **036801**.
- Khveshchenko, D. V., 2001, Phys. Rev. Lett. **87**, 206401.
- Khveshchenko, D. V., 2007, Phys. Rev. B **75**, 153405.
- Klein, O., 1929, Z. Phys. **53**, 157.
- v. Klitzing, K., G. Dorda, and M. Pepper, 1980, Phys. Rev. Lett. **45**, 494.
- Kobayashi, A., S. Katayama, Y. Suzumura, and H. Fukuyama, 2007, J. Phys. Soc. Jpn. **76**, 034711.
- Kohn, W., 1959, Phys. Rev. Lett. **2**, 393.
- Kohn, W., 1961, Phys. Rev. **123**, 1242.
- Kosterlitz, J. M., and D. J. Thouless, 1973, J. Phys. C **6**, 1181.
- Kotov, V. N., B. Uchoa, and A. H. Castro Neto, 2007, Phys. Rev. B **78**, 035119.
- Kotov, V. N., B. Uchoa, V. M. Peirera, A. H. Castro Neto, and F. Guinea, 2010, preprint, arXiv:1012.3484.
- Koulakov, A. A., M. M. Fogler, and B. I. Shklovskii, 1996, Phys. Rev. Lett. **76**, 499.
- Laughlin, R. B., 1983, Phys. Rev. Lett. **50**, 1395.
- Lazzeri, M., and F. Mauri, 2006, Phys. Rev. Lett. **97**, 266407.
- Lee, C., X. Wei, J. K. Kysar, and J. Hone, 2008, Science **321**, 385.
- Lee, K. L., B. Grémaud, R. Han, B.-G. Englert, and C. Miniatura, 2009, Phys. Rev. A **80**, 043411.
- Lewis, R. M., Y. Chen, L. W. Engel, D. C. Tsui, L. N. Pfeiffer, and K. W. West, 2005, Phys. Rev. B **71**, 081301(R).
- Lewis, R. M., Y. Chen, L. W. Engel, D. C. Tsui, P. D. Ye, L. N. Pfeiffer, and K. W. West, 2004, Phys. Rev. Lett. **93**, 176808.
- Lewis, R. M., P. D. Ye, L. W. Engel, D. C. Tsui, L. N. Pfeiffer, and K. W. West, 2002, Phys. Rev. Lett. **89**, 136804.
- Li, G., and E. Andrei, 2007, Nat. Phys. **3**, 623.
- Li, G., A. Luican, and E. Y. Andrei, 2009a, Phys. Rev. Lett. **102**, 176804.
- Li, G., A. Luican, and E. Y. Andrei, 2009b, Phys. Rev. Lett. **102**, 176804.
- Lifshitz, I. M., and A. M. Kosevich, 1956, Sov. Phys. JETP **2**, 636.
- Lilly, M. P., K. B. Cooper, J. P. Eisenstein, L. N. Pfeiffer, and K. W. West, 1999, Phys. Rev. Lett. **82**, 394.
- Lukose, V., R. Shankar, and G. Baskaran, 2007, Phys. Rev. Lett. **98**, 116802.
- Mahan, G. D., 1993, *Many-Particle Physics* (Plenum Press, 2nd Ed., New York).
- Mallet, P., F. Varchon, C. Naud, L. Magaud, C. Berger, and J.-Y. Veuille, 2007, Phys. Rev. B **76**, 041403(R).
- Martin, J., N. Akerman, G. Ulbricht, T. Lohmann, J. H. Smet, K. von Klitzing, and A. Yacobi, 2008, Nat. Phys. **4**, 144.
- McClure, J. W., 1956, Phys. Rev. **104**, 666.
- Meyer, J. C., A. K. Geim, M. I. Katsnelson, K. S. Novoselov, T. J. Booth, and S. Roth, 2007, Nature **446**, 60.
- Mikitik, G. P., and Y. V. Sharlai, 1999, Phys. Rev. Lett. **82**, 2147.
- Min, H., J. E. Hill, N. A. Sinitsyn, B. R. Sahu, L. Kleinman, and A. H. MacDonald, 2006, Phys. Rev. B **74**, 165310.
- Moessner, R., and J. T. Chalker, 1996, Phys. Rev. B **54**, 5006.
- Montambaux, G., F. Piéchon, J.-N. Fuchs, and M. O. Goerbig, 2009a, Phys. Rev. B **80**, 153412.
- Montambaux, G., F. Piéchon, J.-N. Fuchs, and M. O. Goerbig, 2009b, Europhys. J. B **72**, 509.
- Moon, K., H. Mori, K. Yang, S. M. Girvin, A. H. MacDonald, I. Zheng, D. Yoshioka, and S.-C. Zhang, 1995, Phys. Rev. B **51**, 5143.
- Moore, G., and N. Read, 1991, Nucl. Phys. B **360**, 362.
- Morinari, T., T. Himura, and T. Tohyama, 2009, J. Phys. Soc. Jpn. **78**, 023704.
- Mucha-Kruczyński, M., O. Tsyplatyev, A. Grishin, E. McCann, V. I. Fal'ko, A. Bostwick, and E. Rotenberg, 2008, Phys. Rev. B **77**, 195403.
- Nomura, K., and A. H. MacDonald, 2006, Phys. Rev. Lett. **96**, 256602.
- Nomura, K., S. Ryu, and D.-H. Lee, 2009, Phys. Rev. Lett. **103**, 216801.
- Novoselov, K. S., A. K. Geim, S. V. Morosov, D. Jiang, M. I. Katsnelson, I. V. Grigorieva, S. V. Dubonos, and A. A. Firsov, 2005a, Nature **438**, 197.
- Novoselov, K. S., A. K. Geim, S. V. Morosov, D. Jiang, Y. Zhang, S. V. Dubonos, I. V. Grigorieva, and A. A. Firsov, 2004, Science **306**, 666.
- Novoselov, K. S., D. Jiang, T. Booth, V. V. Khotkevich, S. M. Morozov, and A. K. Geim, 2005b, PNAS **102**, 10451.
- Onsager, L., 1952, Philos. Mag. **43**, 1006.
- Papić, Z., M. O. Goerbig, and N. Regnault, 2009, Solid State Comm. **149**, 1056.
- Papić, Z., M. O. Goerbig, and N. Regnault, 2010, Phys. Rev. Lett. **105**, 176802.
- Partoens, B., and F. Peeters, 2006, Phys. Rev. B **74**, 075407.
- Pauling, L., 1960, *The Nature of Chemical Bonds* (Cornell UP).
- Pereira, V. M., A. H. Castro Neto, and N. M. R. Peres, 2009, Phys. Rev. B **80**, 045401.
- Peres, N. M., F. Guinea, and A. H. Castro Neto, 2006, Phys. Rev. B **73**, 125411.
- Peres, N. M. R., 2010, Rev. Mod. Phys. **82**, 2673.
- Peres, N. M. R., and E. V. Castro, 2007, J. Phys.:Condensed Matter **19**, 406231.
- Pisana, S., M. Lazzeri, C. Casiraghi, K. S. Novoselov, A. K. Geim, A. C. Ferrari, and F. Mauri, 2007, Nature Mat. **6**, 198.
- Piscanec, S., M. Lazzeri, F. Mauri, A. C. Ferrari, and J. Robertson, 2004, Phys. Rev. Lett. **93**, 185503.
- Plochocka, P., C. Faugeras, M. Orlita, M. L. Sadowski, G. Martinez, M. Potemski, M. O. Goerbig, J.-N. Fuchs, C. Berger, and W. A. de Heer, 2008, Phys. Rev. Lett. **100**, 087401.
- Polini, M., R. Asgari, G. Borghi, Y. Barlas, T. Pereg-Barnea, and A. H. MacDonald, 2008, Phys. Rev. B **77**, 081411.
- Ponomarenko, L. A., F. Schedin, M. I. Katsnelson, R. Yang, E. W. Hill, K. S. Novoselov, and A. K. Geim, 2008, Science

- 320**, 356.
- Poplavskyy, O., M. O. Goerbig, and C. Morais Smith, 2009, Phys. Rev. B **80**, 195414.
- Qi, X.-L., and S.-C. Zhang, 2011, Rev. Mod. Phys. **83**, 1057.
- Reina, A., X. Jia, J. Ho, D. Nezich, H. Son, V. Bulovic, M. S. Dresselhaus, and J. Kong, 2009, Nano Lett. **9**, 30.
- Roldán, R., J.-N. Fuchs, and M. O. Goerbig, 2009, Phys. Rev. B **80**, 085408.
- Roldán, R., M. O. Goerbig, and J.-N. Fuchs, 2010, Semicond. Sci. Technol. **25**, 034005.
- Sabio, J., J. Nilsson, and A. H. Castro Neto, 2008, Phys. Rev. B **78**, 075410.
- Sadowski, M. L., G. Martinez, M. Potemski, C. Berger, and W. A. de Heer, 2006, Phys. Rev. Lett. **97**, 266405.
- Saito, R., G. Dresselhaus, and M. S. Dresselhaus, 1998, *Physical Properties of Carbon Nanotubes* (Imperial College Press, London).
- Salem, L., 1966, *Molecular Orbital Theory of Conjugated Systems* (Benjamin, New York).
- Shen, T., J. J. Gu, M. Xu, Y. Q. Wu, M. L. Bolen, M. A. Capano, L. W. Engel, and P. D. Ye, 2009, Appl. Phys. Lett. **95**, 172105.
- Shimshoni, E., H. A. Fertig, and G. Vanketeswara Pai, 2009, Phys. Rev. Lett. **102**, 206408.
- Shizuya, K., 2007, Phys. Rev. B **75**, 245417.
- Shon, N. H., and T. Ando, 1998, J. Phys. Soc. Jpn. **67**, 2421.
- Shung, K. W. K., 1986, Phys. Rev. B **34**, 979.
- Sondhi, S. L., A. Karlhede, S. A. Kivelson, and E. H. Rezayi, 1993, Phys. Rev. B **47**, 16419.
- Song, Y. J., A. F. Otte, Y. Kuk, Y. Hu, D. B. Torrance, P. N. First, W. A. de Heer, H. Min, S. Adam, M. D. Stiles, and A. H. MacDonald, 2010, Nature **467**, 185.
- Spielman, I. B., J. P. Eisenstein, L. N. Pfeiffer, and K. W. West, 2000, Phys. Rev. Lett. **84**, 5808.
- Stern, F., 1967, Phys. Rev. Lett. **18**, 546.
- Tahir, M., and K. Sabeeh, 2008, J. Phys.:Condens. Matter **20**, 425202.
- Töke, C., and J. K. Jain, 2007, Phys. Rev. B **75**, 245440.
- Töke, C., P. E. Lammert, V. H. Crespi, and J. K. Jain, 2006, Phys. Rev. B **74**, 235417.
- Tsui, D. C., H. Störmer, and A. C. Gossard, 1982, Phys. Rev. Lett. **48**, 1559.
- Tutuc, E., M. Shayegan, and D. A. Huse, 2004, Phys. Rev. Lett **93**, 036802.
- Wallace, P. R., 1947, Phys. Rev. **71**, 622.
- Weinberg, S., 1995, *The Quantum Theory of Fields* (Cambridge UP).
- Wen, X.-G., and A. Zee, 1992a, Phys. Rev. Lett **69**, 1811.
- Wen, X.-G., and A. Zee, 1992b, Phys. Rev. B **46**, 2290.
- Willett, R. L., J. P. Eisenstein, H. L. Stormer, D. C. Tsui, A. C. Gossard, and J. H. English, 1987, Phys. Rev. Lett. **59**, 1776.
- Williams, F. I. B., P. A. Wright, R. G. Clark, E. Y. Andrei, G. Deville, D. C. Glattli, O. Probst, B. Etienne, C. Dorin, C. T. Foxon, and J. J. Harris, 1991, Phys. Rev. Lett. **66**, 3285.
- Williams, J. R., D. A. Abanin, L. DiCarlo, L. S. Levitov, and C. M. Marcus, 2009, Phys. Rev. B **80**, 045408.
- Wirtz, L., and A. Rubio, 2004, Solid Stat. Comm. **131**, 141.
- Wojs, A., G. Moller, and N. R. Cooper, 2010, preprint , arXiv:1007.3006.
- Wu, X., Y. Hu, M. Ruan, N. K. Madiomanana, J. Hankinson, M. Sprinkle, C. Berger, and W. A. de Heer, 2009, Appl. Phys. Lett. **95**, 223108.
- Wunsch, B., F. Sols, and F. Guinea, 2008, New Journal of Physics **10**, 103027.
- Wunsch, B., T. Stauber, F. Sols, and F. Guinea, 2006, New Journal of Physics **8**, 318.
- Yan, J., Y. Zhang, P. Kim, and A. Pinczuk, 2007, Phys. Rev. Lett. **98**, 166802.
- Yang, K., S. Das Sarma, and A. H. MacDonald, 2006, Phys. Rev. B **74**, 075423.
- Zhang, C.-H., and Y. N. Joglekar, 2007, Phys. Rev. B **75**, 245414.
- Zhang, C.-H., and Y. N. Joglekar, 2008, Phys. Rev. B **77**, 205426.
- Zhang, Y., Z. Jiang, J. P. Small, M. S. Purewal, Y.-W. Tan, M. Fazlollahi, J. D. Chudow, J. A. Jaszczak, H. L. Stormer, and P. Kim, 2006, Phys. Rev. Lett. **96**, 136806.
- Zhang, Y., Y.-W. Tan, H. L. Stormer, and P. Kim, 2005, Nature **438**, 201.
- Zhao, E., and A. Paramekanti, 2006, Phys. Rev. Lett. **97**, 230404.
- Zhou, S. Y., G.-H. Gweon, J. Graf, A. V. Fedorov, C. D. Spataru, R. D. Diehl, K. Kopelevich, D.-H. Lee, S. G. Louie, and A. Lanzara, 2006, Nat. Phys. **2**, 595.
- Zhu, S.-L., B. Wang, and L.-M. Duan, 2007, Phys. Rev. Lett. **98**, 260402.